A Numerical Investigation into Transonic Flight on Mars Utilizing a 2-D URANS Approach

by

Michael Westheim

Student number: 4355636
Project duration: March 9, 2021 – March 18, 2022
Thesis committee: Dr. F. Avallone, TU Delft, supervisor
Dr. T. Michelis, TU Delft, supervisor
Dr. R. Schmehl, TU Delft, Chair
Dr. M. Kotsonis, TU Delft

TU Delft

Abstract

Interest in powered flight on Mars has been growing in recent years, and as such new developments are being made in determining the effects the Martian atmosphere has on the flow physics and performance, specifically with regards to similarity parameters: the Reynolds number and the Mach number. Studies have been conducted for low Reynolds numbers in the past, and have shown that conventional airfoils exhibit non-linearity in performance due to vortex development and the formation of a laminar separation bubble. Mach number effects have been seen to have a stabilizing effect on the separated shear-layer and have a detrimental impact on this behavior. This paper aimed to investigate whether transonic effects could increase attached flow while improving aerodynamic performance due to the presence of a smeared shock. 2-D URANS simulations of a NACA-0012-34 airfoil were conducted with a SST k-ω, γ-intermittency model. The results find that an expansion fan delays separation, while the smeared shock weakens the adverse pressure gradient; this reduces the impact of the shock on the drag-coefficient, similar to a shock control bump; the result is a minute increase in the lift-to-drag performance. The development of coherent structures within the separated shear-layer have also been seen to be impacted due to the stabilizing effect of compressibility on the Kelvin-Helmholtz instability.

Contents

List of Symbols

α Angle of Attack [deg]
a Speed of Sound [m/s]

C_D Drag Coefficient [-]
C_f Skin Friction Coefficient [-]
c Chord Length [m]
C_L Lift Coefficient [-]
$C_{P,min}$ Minimum Pressure Coefficient [-]

d Reference Length [m]
δ^* Displacement Thickness [m]
μ Dynamic Viscosity [Pa s]
μ_0 Reference Dynamic Viscosity [Pa s]

f_n Nyquist Frequency [Hz]
f Frequency [Hz]
f_s Sampling Frequency [Hz]
f_i Solutions from each Grid Refinement [-]
F_x X-component of Force [N]
F_y Y-component of Force [N]

γ Specific Heat Ratio [-]
h_i Grid Spacing [m]

I Turbulent Intensity [-]

k Turbulent Kinetic Energy [m^2/s^2]

M Mach Number [-]
M_{crit} Critical Mach Number [-]

θ Momentum Thickness [m]
$\frac{\mu_t}{\mu}$ Eddy Viscosity Ratio [-]

N Number of Time-Steps [-]

p Observed Order of Accuracy [-]
P Pressure [Pa]]

R Specific Gas Constant [J/kg K]
Re Reynolds Number [-]
r Refinement Factor [-]
ρ Density [kg/m^3]
ρ_∞ Freestream Density [kg/m^3]

S Surface Area [m^2]
H Shape Factor [-]
S_t Strouhal Number [-]

T_0 Reference Temperature [K]
τ_w Wall Shear Stress [Pa]
T Temperature [K]
t Time [s]
Δt Time-step [s]
t_c Non-dimensional time [-]

U Velocity [m/s]
U_e External Velocity for a boundary layer [m/s]
U_∞ Freestream Velocity [m/s]

x_s Distance to Ramp [m]

List of Figures

1 Introduction

The concept of powered flight on Mars has been a topic of research and inquiry for some time [10, 19, 40]. However, in recent years there has been an increased interest in the topic, mainly with regards to small, drone-like vehicles [2, 17, 51]. Flight on Mars offers a key benefit that the conventional Martian rover lacks, and that is the ability to quickly survey land [2]. The atmosphere of Mars is vastly different compared to that of Earth: the density is about 1.5% of the latter's; the atmosphere is composed primarily of carbon dioxide, and the average temperature is around $210\,\mathrm{K}$ [22, 55].

With these key differences, a few inferences can be made about the Reynolds and Mach numbers. A reduction in density already indicates that the Reynolds number will be lower than the value expected on Earth, assuming the rest of the flow conditions remain constant; this ignores the fact that the sea level dynamic viscosity of Mars' Carbon Dioxide based atmosphere will be noticeably lower than when compared to Earth's: from $1.789 \times 10^{-5}\,\mathrm{N\,s\,m^{-2}}$ to $1.289 \times 10^{-5}\,\mathrm{N\,s\,m^{-2}}$ [44, 55, 58]. In general, if a standard airfoil with a one-meter chord length traveling at 20 m/s were considered on both planets; the one on earth would have a Reynolds number of 1.37×10^{6} while the one on Mars would have a Reynolds number of 2.32×10^{4}.

Another key point of interest is that due to the lower density, the lift generated by an airfoil on Mars, assuming a constant velocity, is around 60 times lower than that generated on Earth; though this is in part counteracted by the lower gravity on Mars. The velocity will need to increase by 500% in order to maintain the same lift-to-weight ratio as on earth. The increase in velocity coincides directly with an increase in Mach number; this is compounded with the change in atmospheric composition: a lower gas constant; $189\,\mathrm{J\,kg^{-1}\,K^{-1}}$ on Mars compared to $287\,\mathrm{J\,kg^{-1}\,K^{-1}}$ on Earth; a lower heat capacity ratio; γ = 1.289 compared to γ = 1.4; and a lower temperature; T = $214\,\mathrm{K}$ compared to $288\,\mathrm{K}$. This results in an overall decrease in the speed of sound, $a \approx 220\,\mathrm{m\,s^{-1}}$ at sea level on Mars, to $a \approx 340\,\mathrm{m\,s^{-1}}$ at sea level on Earth.

As a result of these effects, fixed-wing and rotor aircraft on Mars are designed with Mach numbers anywhere from M = 0.45 to 0.7 for Reynolds numbers ranging from Re = 1×10^{3} to 1×10^{5} [2, 10, 17, 19, 40, 51]. A wind tunnel was built in order to model the atmosphere of Mars and determine the Reynolds and Mach number effects under those atmospheric conditions [5, 6]. The wind tunnel provides excellent insight into low Reynolds number, compressible flows, but is limited at a maximum Mach number ($M \approx 0.8$) with a subsequently narrow range of Reynolds numbers.

The limitations of the Mar Wind Tunnel bring us to the aim of this paper, which is to investigate transonic flight on Mars; specifically how shock wave boundary-interactions behave at the low Reynolds numbers typical for Mars. As such this paper delves into shock-wave boundary-layer interactions, and the impact of non-dimensional numbers: primarily the Mach and Reynolds number; as such, a review of boundary layer theory, specifically with regards to Reynolds and Mach effects will be briefly reviewed prior to discussing them specifically in the circumstances of the low Reynolds compressible flight regimes one would expect on Mars.

1.1. Research Questions & Outline

The following questions are posed as the aim and goals of this research; the background for how these questions were formulated will be presented after the literature portion of this paper.

1. **Given the atmosphere composition of Mars, can the introduction of a shock wave improve aerodynamic (L/D) performance by inducing a delay in separation and/or earlier transition of the laminar boundary layer?**

   (a) What are the relevant Reynolds & Mach number effects at the atmospheric conditions on Mars?

      i. How does a change in either the Reynolds or Mach number affect the interaction between the shock wave and the boundary-layer?

      ii. How does a change in either the Reynolds or Mach number impact boundary-layer separation?

      iii. How does a change in either the Reynolds or Mach number influence the stability of the boundary-layer?

The outline of this paper is as follows: An introduction to relevant non-dimensional effects on Earth as they are known conventionally, which will then proceed into a discussion on their behavior within the sea-level atmospheric conditions on Mars; a second chapter will discuss the formulation of the aforementioned research questions, and provide more context into how they were developed; the next chapters will discuss the specifics of the methodology, comprised of the defining the necessary parameters, the software and computation method, and the validation of the method; finally, the results will be presented, in a similar fashion to those of similar papers, with an emphasis on the relevant non-dimensional effects, and how they shape a general understanding of transonic flight on Mars.

2 Investigation into Martian Aerodynamics

Only recently has there been development into trying to realize the conditions of Mars through the means of experimental development; in 2010, Anyoji et al [5] published a paper detailing their development of a Mars wind tunnel (MWT). The paper detailed that the design criteria used for conventional aircraft are not applicable to Mars, due to the atmospheric conditions, and more importantly, due to the low Reynolds numbers and high Mach numbers necessary to generate enough lift. Despite the dearth of open literature on the topic of Martian flight, what is available describes an inherently strong interaction between viscous effects and compressibility effects [5, 39, 55, 56].

2.1. The Reynolds Number & Boundary Layer Parameters

The introduction presented the key differences between the atmospheres of Earth and Mars, primarily with regards to non-dimensional numbers. To be more specific, the Reynolds numbers on Mars are smaller by a factor of 60 compared to Reynolds numbers on Earth. This is significant because the vast majority of airfoils are intended for Reynolds numbers around $Re = 1 \times 10^6$ [15]. Consequentially. as Re decreases, performance drastically decreases as a result [15, 66]. The reasoning behind why is well understood: Re has an effect on boundary layer behavior, and in fact is dominant in how it affects transition [62].

$$Re = \frac{\rho U_\infty c}{\mu} \tag{2.1}$$

The Reynolds number effectively describes the ratio of inertial forces to the viscous forces in a given flow (Equation 2.1) [28] , and from this understanding, along with the relationship between the shear stress and the boundary layer velocity gradient. A decrease in Re results in a relative increase in viscous forces; the boundary-layer thickness is proportional to viscosity, and thus results in a shallower velocity gradient. A decrease in Re results in an increase in the skin friction coefficient, C_f [28].

$$\delta^* = \int_0^\infty \left(1 - \frac{\rho U}{\rho_\infty U_\infty}\right) dy \tag{2.2}$$

A decrease in Reynolds number results in an increase in the boundary layer thickness and the displacement thickness, δ^*; the displacement thickness describes the necessary increase in airfoil thickness to have an equivalent inviscid mass flow. Effectively, the displacement thickness describes the mass flow detriment due to viscosity [28], as described analytically in Equation 2.2.

$$\theta = \int_0^\infty \frac{\rho U}{\rho_\infty U_\infty}\left(1 - \frac{U}{U_\infty}\right) dy \tag{2.3}$$

Similarly enough, the momentum thickness, θ, describes the momentum detriment due to viscosity in the form of a thickness (Equation 2.3). The ratio between the displacement and momentum thickness defines the shape factor, H, which is a non-dimensional parameter that describes the shape of the velocity distribution within the boundary layer [28], as seen in Figure 2.1. The displacement thickness and momentum thickness, through the shape factor, along with the skin friction coefficient, contribute to the Von Kármán momentum integral relation (Equation 2.4) [62].

$$\frac{C_f}{2} = \frac{d\theta}{dx} + \theta\frac{(H+2)}{u_e}\frac{du_e}{dx} \tag{2.4}$$

An important part of the shape factor is how it eloquently and concisely conveys the behavior of the boundary-layer; one can quickly see where transition and separation of the shear-layer occurs [50]. The shape factor can indicate whether a boundary-layer is laminar (H = 2.7) or turbulent (H = 1.3). Additionally, one can relate the shape factor and Re in order to predict where transition occurs; a decrease in the shape factor is indicative of transition an attached boundary layer [21]. Flow transition is not predicted to occur when Re is below the critical Reynolds number, which in turn aids delaying transition and thus reattachment, if it occurs [28].

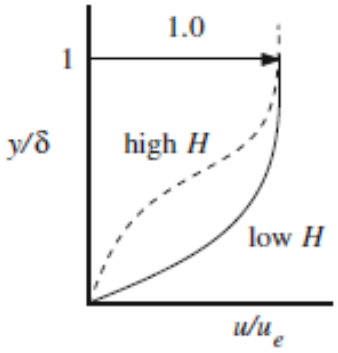

Figure 2.1: Shape Factor [62]

Flow separation is a boundary layer phenomenon that can occur due to excessive momentum loss near the wall in a boundary layer as the flow attempts to continue downstream against increasing pressure, often described as an adverse pressure gradient [62]; this is opposed to a decreasing pressure, which is referred to as a favorable pressure gradient [62]. The shape factor is important in helping understand when boundary layer separation occurs; a laminar boundary layer is predicted to separate around a shape factor of H = 4, while a turbulent boundary layer is expected to detach around a shape factor of H = 2.7 [47]. The pressure dis-

tribution over an airfoil is generally defined by the curvature of that airfoil, increasing curvature results in higher super-velocities and thus a favorable pressure gradient, while a divergent curvature results in an adverse pressure gradient for subsonic Mach numbers [62]. Laminar separation and turbulent separation can be predicted, both utilizing different formulations and estimations by Stratford [60]. The pressure distribution is also affected by a change in Re; a decrease in Re coincides with a decrease in the magnitude of the suction peak due to a change in effective curvature as a result of the increased displacement thickness [11].

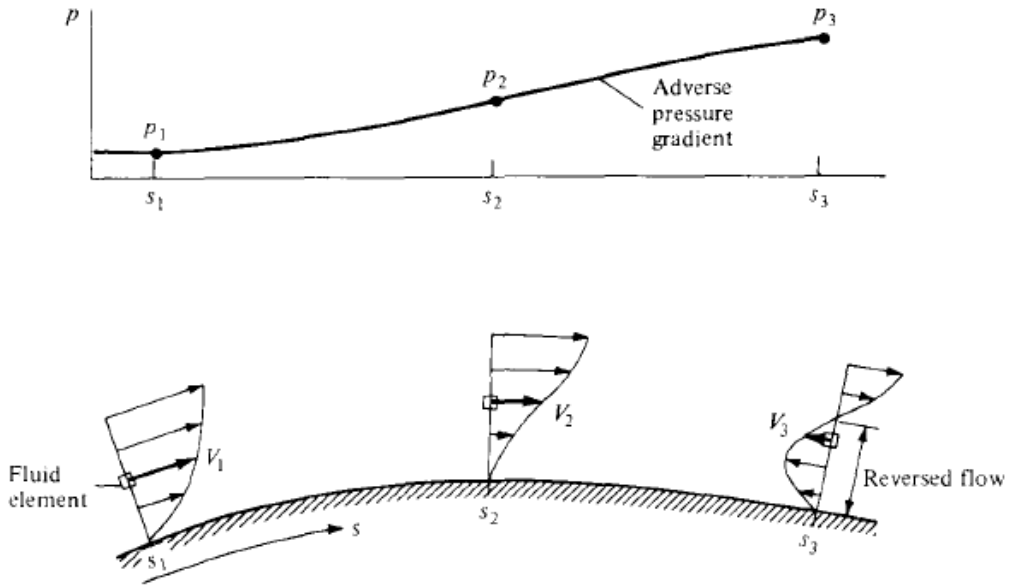

Figure 2.2: Separated flow induced by an adverse pressure gradient. [28]

The adverse pressure gradient can result in periodic instabilities, such as two-dimensional Tollmien-Schlichting (TS) waves, which are the first of the instabilities that appear in laminar flow [62]. The instabilities in a flow can be caused by numerous parameters: the surface roughness, the turbulence present in the free-stream, the onset of an adverse pressure gradient, and the heating of a fluid by the surface [28], vibration, sound, free-stream disturbances and more [57, 62]. These instabilities can result in the separated laminar shear-layer to undergo transition. Transition can be described as the point where instabilities in the flow rapidly grow; the steps in transition are complicated and have overlapping dependencies; though in general there is some initial growth of nearly two-dimensional Tollmien-Schlichting waves, which are the first of the instabilities that appear in laminar flow [62]. The Tollmien-Schlichting waves grow, and eventually become three-dimensional. As a result, several forms of unstable vortices occur within regions of high localized shear stress; they are longitudinally stretched, and start to break down into smaller units, at which intense local changes occur randomly. Eventually, this results in a fully turbulent flow [62]. The entire process is artistically visualized in Figure 2.3.

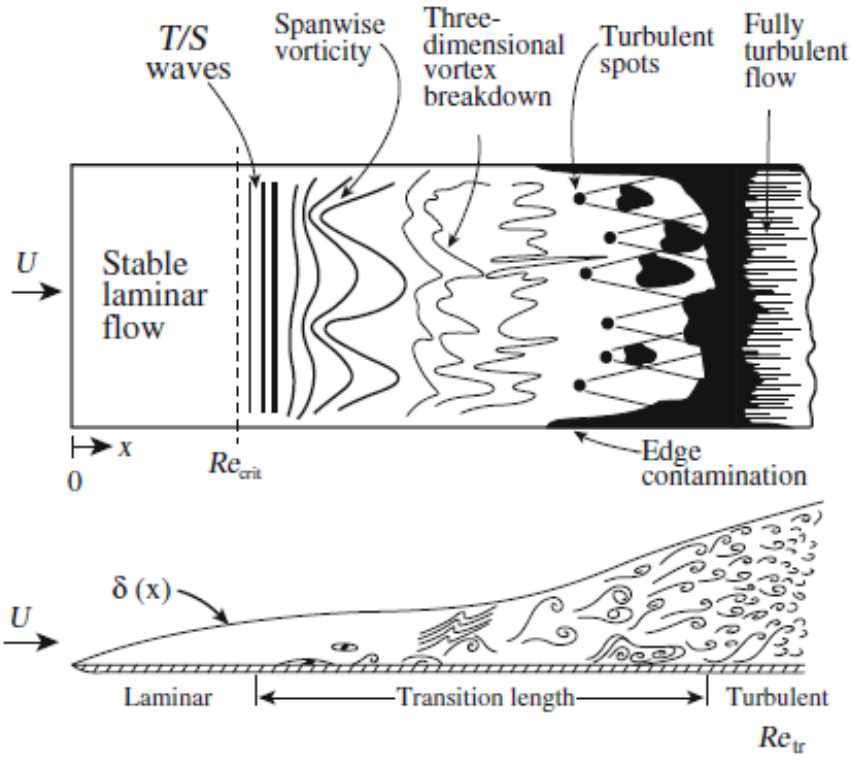

Figure 2.3: Idealized boundary layer transition over a flat plate [30, 62]

There is a critical Reynolds number, Re_{cr}, at which the reference length, x_{cr} is the point in which natural transition occurs. The value of Re_{cr} is difficult to predict, as such, a general rule of thumb is that the value is around 5×10^5; any boundary-layer with a Reynolds number considerably lower than this value will likely remain laminar [28]. Transition can still occur at low Reynolds numbers, as other causes of instabilities can still have a substantial impact; as Re decreases, however, the critical Reynolds number demands a larger shape factor before instabilities occur in a significant enough manner [62] (Figure 2.4).

A decrease in the shape factor is indicative of transition for an attached boundary-layer, the transition point of a separated shear layer remains hard to find [21], though a decrease in shape factor still illustrates (Figure 2.5) that transition of the separated shear layer does still occur [31]. The transition process can lead to vortex shedding [69]; vortex shedding is an unsteady periodic pattern of vortex development where the upper and lower surface of a body develops a vortex in an alternating fashion, an example of this is called a Kármán vortex street and is typically observed for flow over a cylinder [28]. This flow phenomenon occurs due to coherent structures developing in the wake of the airfoil. The development of these structures is suggested to be due to the Kelvin-Helmholtz instability in the separated shear layer, while other studies suggest it is due to the transition process [69]. The frequency at which the vortex sheds is dependent on Re, and at the conditions considered in this paper (Re = 1×10^4 to 1×10^5), would result in Strouhal numbers of around S_t = 0.21 S_t = 0.14 [43, 69].

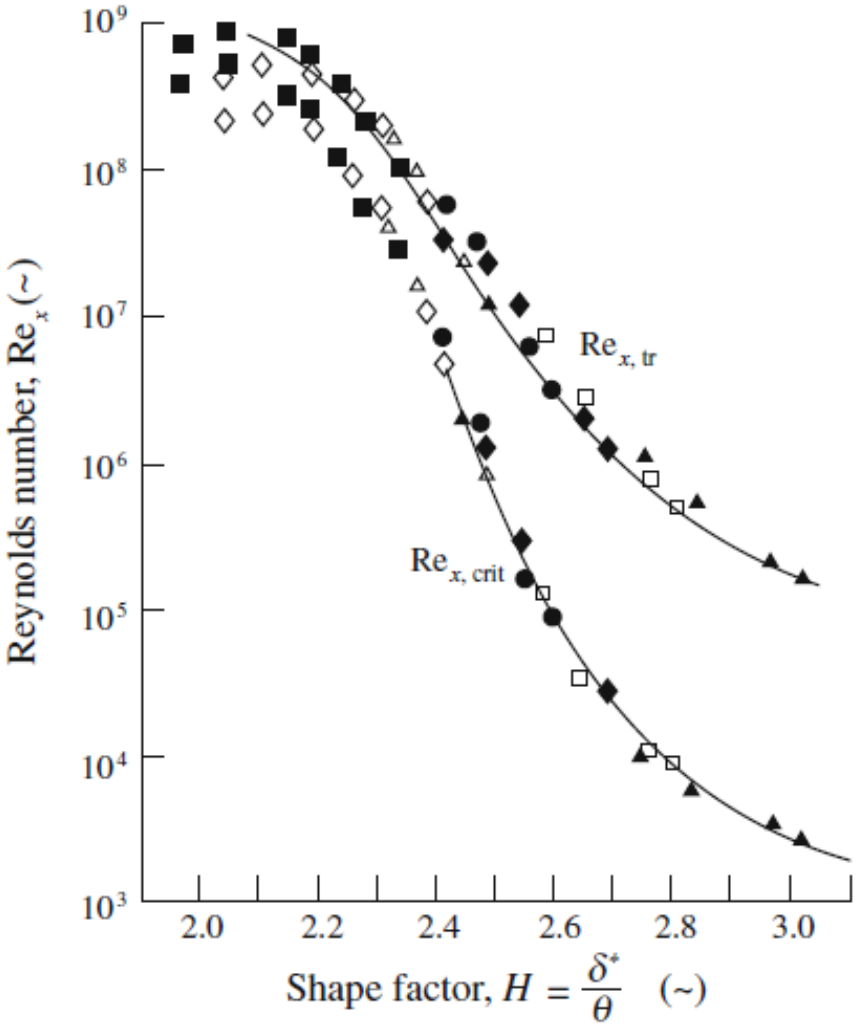

Figure 2.4: Correlation between shape factor and transition Reynolds number [62]

Given a Reynolds number where at which the laminar boundary-layer separates prior to transition, the instability of the separated shear layer can result in the transition and subsequent reattachment of the separated laminar shear layer; this can result in the formation of a laminar separation bubble (Figure 2.6). First observed by Jones [27] in 1934, A laminar separation bubble is a temporary region of reversed flow, that is formed when the laminar boundary layer separates prior to transition, and then reattaches [62]. Reattachment occurs when the turbulent boundary layer has enough momentum to resist the adverse pressure gradient. A flow separates due to an adverse pressure gradient, in which the flow momentum can no longer overcome the pressure differential, and thus a region of reverse flow occurs. Reattachment occurs when the flow either regains enough momentum, or the pressure gradient becomes more favorable, to the point where the flow can reattach again. Typically this is a result of transition [28], but can be induced by a strong shock interaction as well [62]. The formation of a laminar separation bubble is ideal when compared to the alternative of a separated shear

layer that fails to reattach, as the increased attached flow is positive for both lift and drag performance [50, 60].

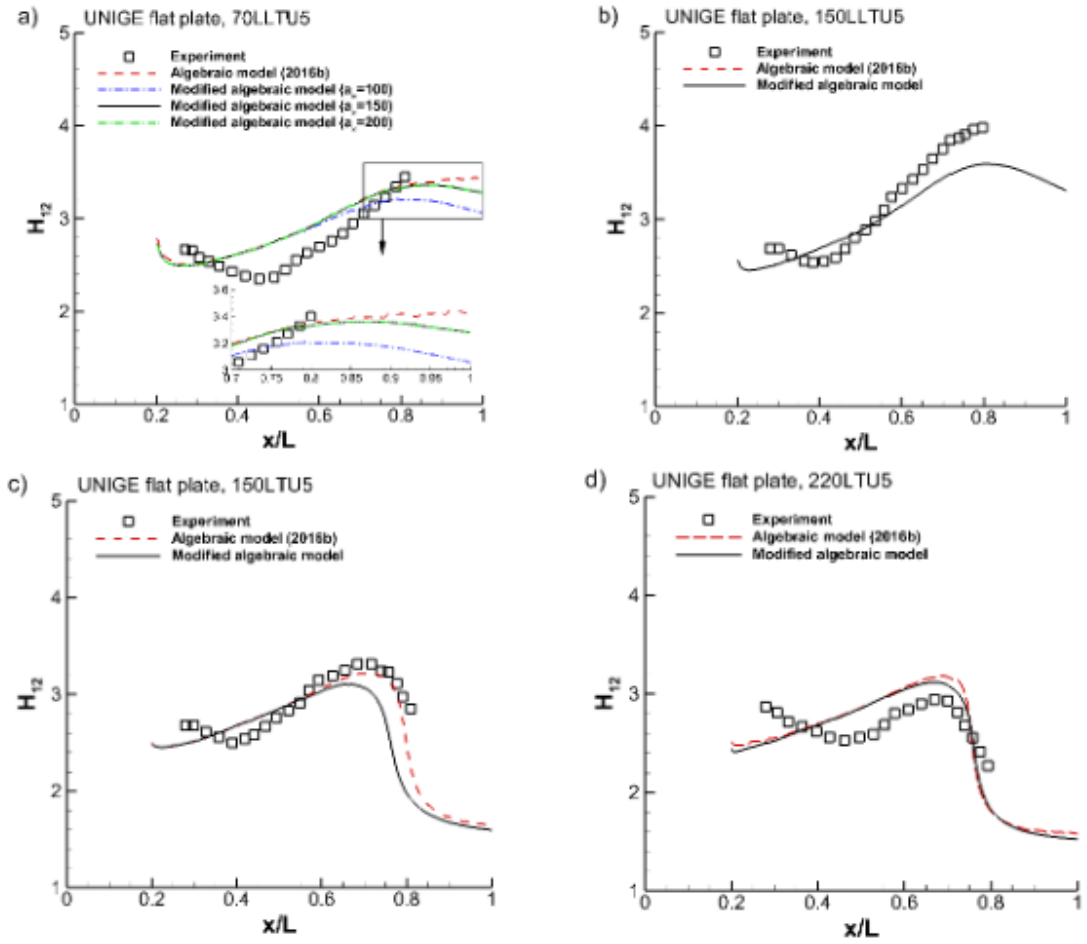

Figure 2.5: UNIGE flat plate. Measured and predicted shape factor evolutions for cases without transition before the end of the plate (a,b) and with bypass transition (c,d). [31]

The shape and thickness of an airfoil have a substantial relationship with Re: for conventional Reynolds numbers, a lower thickness would produce greater suction peaks at higher angles of attack due to the increase in curvature at the leading edge; this would thus result in earlier separation compared to a thicker airfoil at high angles of attack. At lower angles of attack, the opposite is true; as the curvature of thicker airfoils produces a larger suction peak. This behavior is amplified for lower Reynolds numbers, where the boundary-layer is more prone to separation given an adverse pressure gradient. Due to this, in some cases, a flat plate can perform better than a conventional airfoil, such as a NACA 0012 [66] (Figure 2.7).

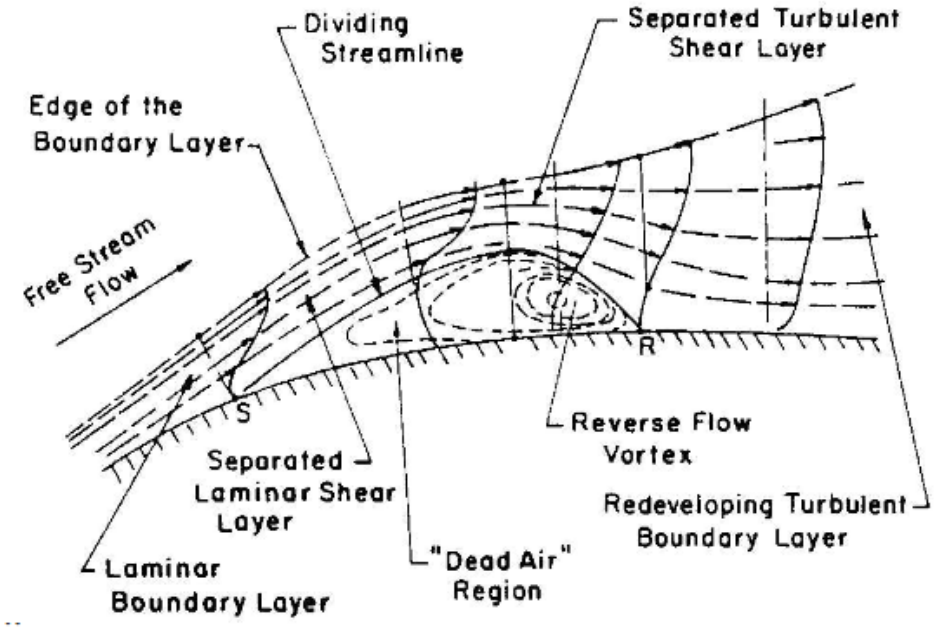

Figure 2.6: The classical structure of a short laminar bubble [8, 26]

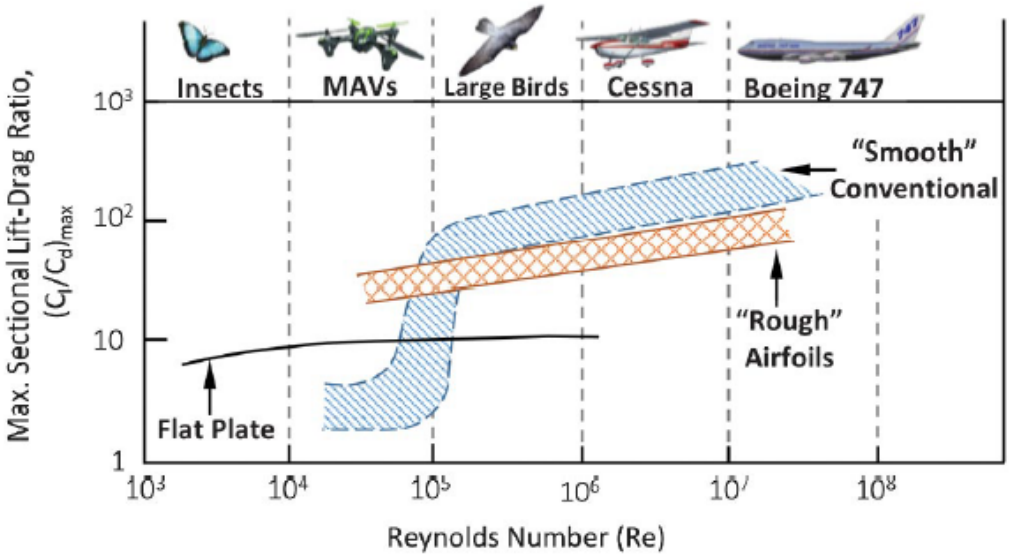

Figure 2.7: Effect of Reynolds number on airfoil maximum sectional lift-to-drag ratio. (Adapted from McMasters and Henderson [34] and Mueller [38]) [66]

2.1.1. Effect of Low Reynolds Numbers

Winslow et al. [66] have compiled low Reynolds number experimental results for a NACA 0012 airfoil, such as those by Ohtake et al. [42], and have shown that the aerodynamic performance at low Reynolds numbers exhibits unique non-linear behavior. At conventional Reynolds numbers, the lift curve slope would remain linear, up until high angles of attack where it will round-off due to stall; however, the lift polars at low Reynolds numbers illustrate a different scenario (Figure 2.8). As can be seen, there is a substantial change in the shape of the lift curve, especially as Re decreases further.

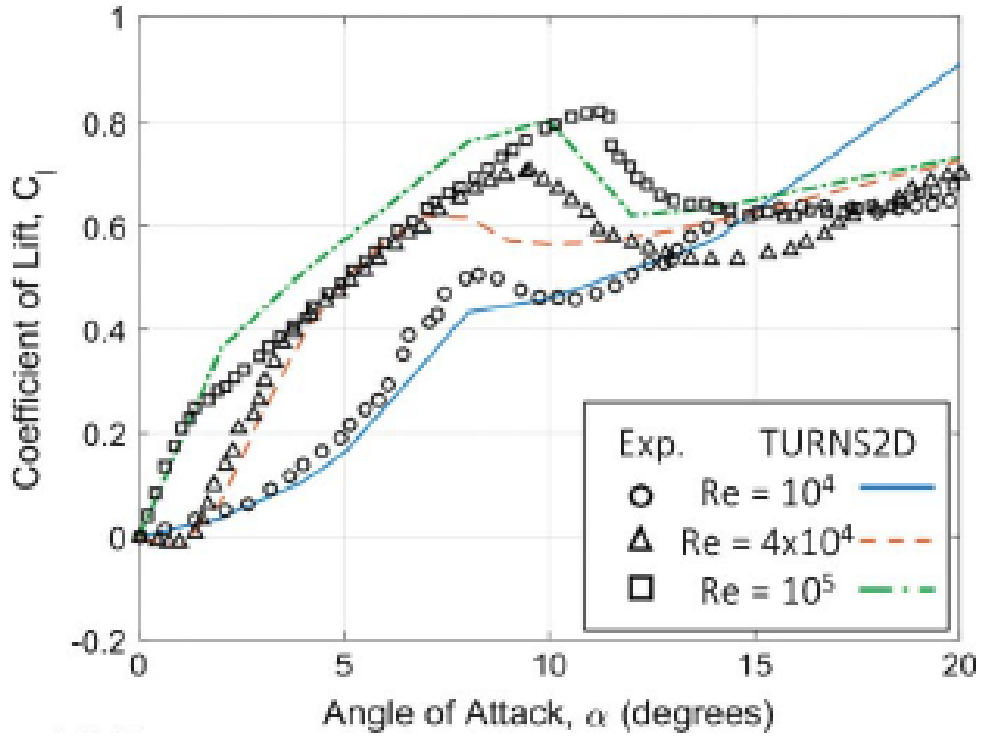

Figure 2.8: Lift coefficient comparison of CFD predictions for NACA 0012 between Reynolds numbers of 104 and 105. (Experimental data from Ohtake et al. [42].)[66]

The lift curve of the NACA 0012 airfoil exhibits a noticeable non-linearity, or shift in the slope of the lift curve; the cause of this non-linearity in the lift curve is due to how the separation and laminar-to-turbulent transition behave at lower Reynolds numbers. When Re decreases, transition is delayed further and further downstream, this can be explained by Figure 2.4. As mentioned before, laminar separation typically occurs around H = 4 [47]. As Re decreases, the critical and transition Reynolds numbers occur at higher shape factors, thus indicating that separation is increasingly more likely to occur prior to transition; this results in laminar separation, with transition occurring downstream. The transition point occurs further and further aft as Re decreases. The separation and transition points begin to move upstream as the angle of attack increases, resulting in a substantial separation.

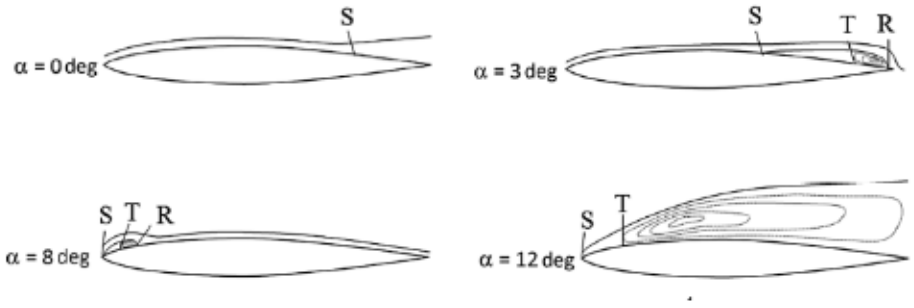

Figure 2.9: Four main stages of the flow behavior due to an increasing angle of attack at low Reynolds numbers (Adapted from [5])

Transition in the separated shear layer plays part in vortex development at lower Reynolds numbers [69]. The final stages of transition, described by a rapid flow breakdown to turbulence (illustrated in Figure 2.3) are associated with non-linear interactions [69]; at this stage of transition, coherent structures begin to form [69], whereas Watmuff [64] suggests these are associated with the Kelvin-Helmholtz instability [69]. There is still debate whether these structures persist into the attached turbulent boundary layer, or break down in the reattachment region [69]. Villegas & Diez [61] aimed to expand upon the relationship between wake vortex shedding and aerodynamic force fluctuations for a low Reynolds number wing; an illustration of this can be seen in Figure 2.11. Yarusevych et al. [69] suggest that the development of coherent structures in the wake of some airfoil at lower Reynolds numbers is of interest, as it affects the airfoil performance, along with governing flow around downstream objects, which could produce undesirable structural vibrations and noise generation. The coherence and the length scale of the wake vortices are diminished significantly due to the formation of the separation bubble [69].

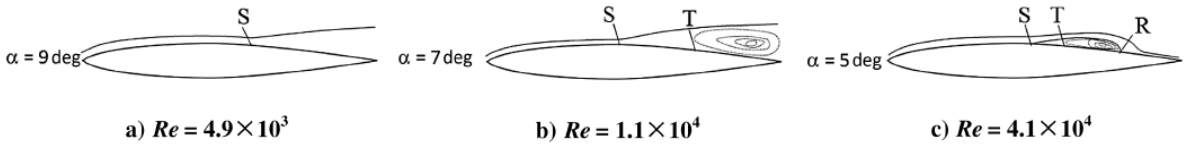

Figure 2.10: Reynolds number effect on flow behavior at low Reynolds numbers (Adapted from [5])

The formation of a laminar separation bubble is delayed until higher angles of attack as Re decreases due to the increased stability of the boundary- and shear-layers. This results in elongated bubbles due to the increased or 'excessive' amount of laminar flow. In this case, excessive laminar flow is used to describe the subsequent aft movement of the transition point, resulting in a delayed formation of a laminar separation bubble to higher angles of attack; this reduces the amount of attached flow due to the increased amount of trailing edge separation, which progresses further as the angle of attack continues to increase prior to the formation of the separation bubble. Therefore, any further reduction in Re would see the transition point move further downstream, and inhibit reattachment. These elongated bubbles have

their reattachment point further downstream and are delayed until higher angles of attack as Re decreases, and provide less of a lift enhancement compared to a smaller bubble, or, ideally, a fully attached boundary-layer. As the angle of attack increases, the laminar separation bubble begins to move upstream and contract in size, this is due to the increasingly adverse pressure gradient expediting separation and transition. Figure 2.10 illustrates the effect of the Reynolds numbers on the transition point, and the formation of the laminar separation bubble.

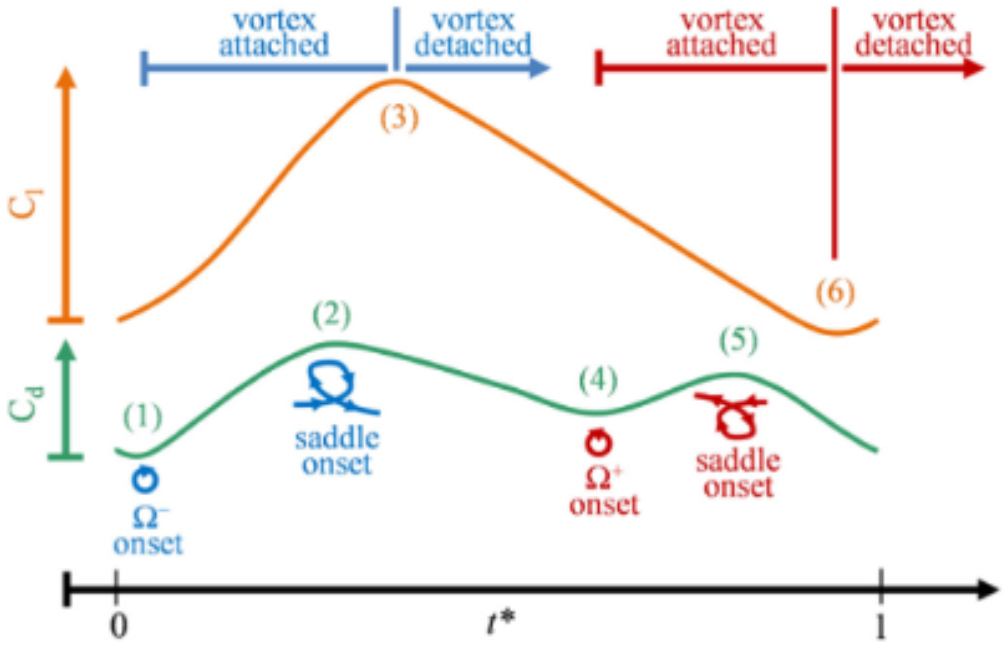

Figure 2.11: Sketch showing the force-vortex relationship for one shedding cycle. [61]

2.1.2. Effect of Differing Atmospheric Compositions

The discussion on low Reynolds numbers up until now has been primarily discussing what is seen at low Reynolds numbers on Earth. This means that the Mach numbers are substantially smaller than for an equivalent Reynolds number on Mars, and that the atmospheric composition is Air instead of CO_2. The effect of this atmospheric change was investigated by Anyoji et al. [5]. The Reynolds numbers discussed considered ranged from $Re = 1 \times 10^3$ to 1×10^5, with Mach numbers considered ranging from M = 0.2 to 0.61 [6]. Anyoji et al. [5] developed a Mars wind tunnel in order to investigate Reynolds and Mach number effects for various airfoils; they considered two geometries for their investigation into Martian flight, both with a 50 mm chord length: a flat plate, and a NACA 0012-34 airfoil. The NACA 0012-34 airfoil is a modified NACA 0012 airfoil with a smaller radius at the leading edge. The purpose of the reduction in leading-edge radius was to lessen the leading edge separation at low angles of attack due to the effects of bluntness.

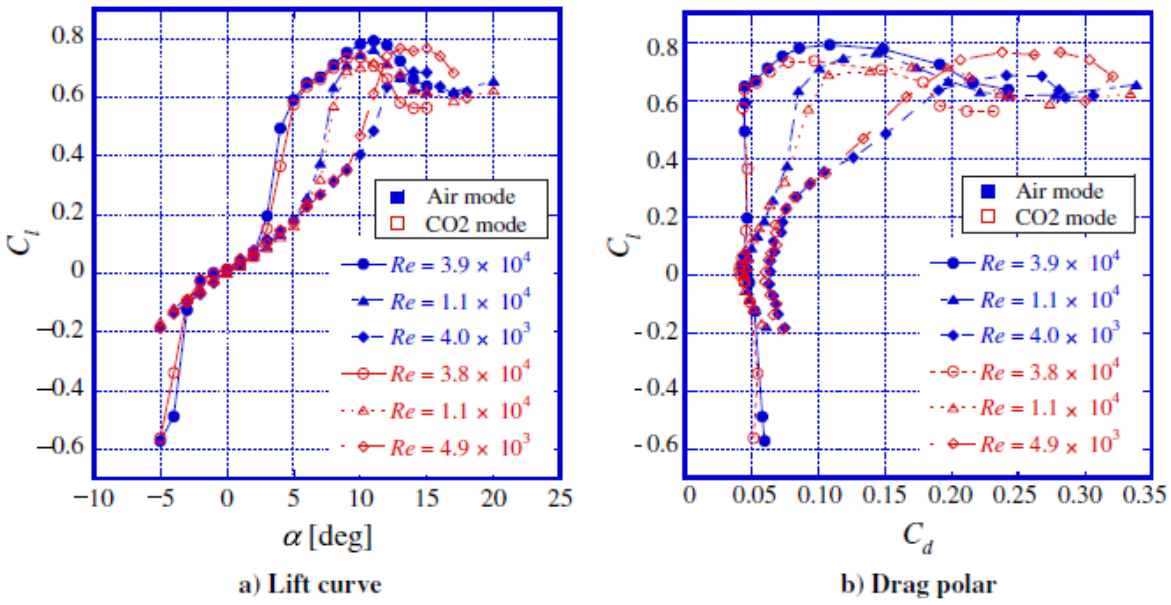

Figure 2.12: Effects of specific heat ratio on aerodynamic characteristics of the NACA 0012-34 for a constant Mach number (M = 0.20). [5]

The effect of the two different atmospheric modes, Air and CO_2, on aerodynamic performance is shown in Figure 2.12. The behavior of the Reynolds number in a Martian atmosphere appears to be consistent with what is known for Earth; this brings to the topic of atmospheric composition to the forefront, more specifically in how the predominantly Carbon Dioxide based atmosphere on Mars affects the behavior of the airfoil within the same Mach and Reynolds number conditions of that on Earth. The specific heat ratio, γ of CO_2 and air were considered to determine the effect of the atmospheric composition on aerodynamic performance. Only a slight difference was found, specifically in the post-stall angle of attacks, and a shift from an atmosphere composed of air to CO_2 had little effect on the force measurements [5, 39]. With this, it is clear that the Reynolds number effects experienced on Earth also apply to Mars in a non-dimensional sense. This is not to say that the gaseous composition of the atmosphere does not matter; the specific heat ratio and specific gas constant of Mars are lower than Earth's, which results in a lower speed of sound, and thus increased Mach numbers.

2.2. Mach Number Effect on Boundary- & Shear-Layer Behavior

The Mach number is where the differences between Earth and Mars begins to diverge substantially when considering a similar range of Reynolds numbers at a constant chord length on either of the two planets, with up until the high subsonic to low transonic Mach numbers being feasible for the discussed Reynolds numbers of $Re = 1 \times 10^3$ to 1×10^5. The Mach number is also affected by the atmospheric composition of Mars, as the speed of sound is reduced due to a decrease in temperature, specific heat ratio, and the specific gas constant (Equation 2.5).

$$a = \sqrt{\gamma R T} \tag{2.5}$$

The Mach number has a substantial impact on the behavior of the boundary-layer. when considering compressibility, the assumptions of a constant viscosity, density, and heat transfer coefficient within the boundary layer no longer remain valid [62]. The skin friction coefficient changes due to a now present temperature distribution in the boundary layer, which in turn has an effect on the velocity gradient; additionally, the temperature distribution impacts the viscosity through Sutherland's law [62]. The effects of compressibility can also be seen through the isentropic flow relations, and their effect on pressure, density, and temperature. The varying density would in turn impact the displacement and momentum thickness', which would impact the development of the external flow velocity. For a compressible laminar boundary-layer on an adiabatic wall, The momentum integral equation takes the form seen in Equation 2.6 [50].

$$\frac{d\theta}{dx} + \frac{\theta}{u_e}\frac{du_e}{dx}\left(2 + H - M^2\right) = \frac{C_f}{2} \tag{2.6}$$

Transition is a primary point of interest for low Reynolds numbers, as discussed previously in Section 2.1.1. The specifics of the Mach numbers effect on stability theory is complicated; in simple terms, compressibility impacts the stability of the boundary-layer by removing heat from the boundary layer; which results in increased stability [50]. A study conducted on two-dimensional low Reynolds compressible flows around a cylinder has seen that an increase in Mach number results in lower shedding amplitudes and Strouhal numbers, though the Reynolds numbers studied lay between Re = 20 & Re = 100 [14]. The Mach number, or to be more precise, compressibility, has been seen to have a noticeable impact on the Kelvin-Helmholtz instability; it has been shown that the introduction of compressibility results in a suppression of the Kelvin-Helmholtz instability due to the dynamics of the pressure-vorticity interaction [29]. For incompressible Mach numbers, the Kelvin-Helmholtz instability is dominated by the dissipation of clockwise vortices, and the enhancement and merging of two counter-clockwise vortices, which begin to roll-up rapidly around the pivot point [29]; for compressible Mach numbers, vortex reversal occurs instead, with no roll-up, and thus prevent the positive feedback essential for mixing [29].

$$C_p = \frac{C_{p,0}}{\sqrt{1 - M_\infty^2}} \tag{2.7}$$

There is an additional impact on the pressure distribution; the methods to account for this impact are known as compressibility corrections [28]. The Prandtl-Glauert correction (Equation 2.7) states that if the incompressible pressure distribution is known, then the compressible pressure distribution for the same airfoil can be determined [28]. The same correction applies to the lift and moment coefficients. This correction under-predicts the experimental data, and there are other compressibility corrections as well [28]. The benefits of an increase in Mach number due to compressibility effects are limited to low to high subsonic Mach numbers [3, 12, 52]. The predicted increase in C_L begins to reverse once M approached M_{crit}; an example is shown in Figure 2.13; this is due to the formation of a shock-wave, and the subsequent separation of the boundary layer due to the strong adverse pressure gradient [62].

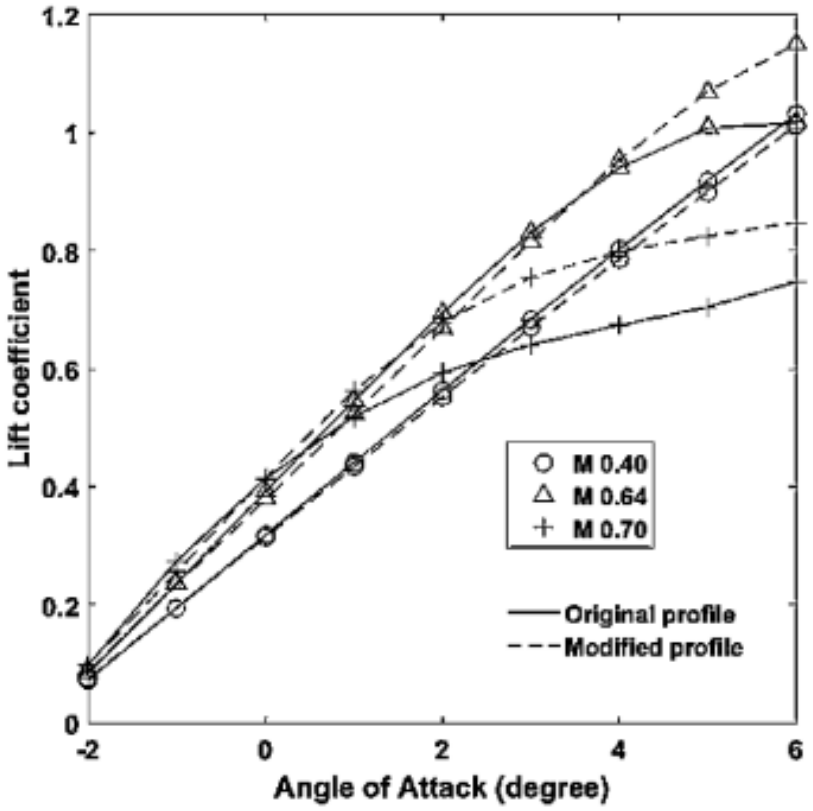

Figure 2.13: Lift coefficient at each angle of attack at various Mach numbers at $Re = 6 \times 10^6$ for a NASA LS-0013 Airfoil at an angle of attack of $\alpha = 4\,\mathrm{deg}$ [52]

2.2.1. Mach Number Effects on Martian Aerodynamics

As the Reynolds number effects are consistent on Earth and Mars, the only key similarity parameter remaining is the Mach number, as most low Reynolds numbers are considered for flight on Earth, only Mach numbers below M = 0.3 are considered [5, 15, 55]. There is a general trend that is seen in other analyzes of low Reynolds number effects: an initial trailing edge separation, vortex development, the formation of a separation bubble, and then eventual leading-edge stall; these are predominately impacted by the delay in transition. The Mach number's effect on boundary-layer stability was discussed in Section 2.2, and is seen to have a stabilizing effect on the boundary-layer.

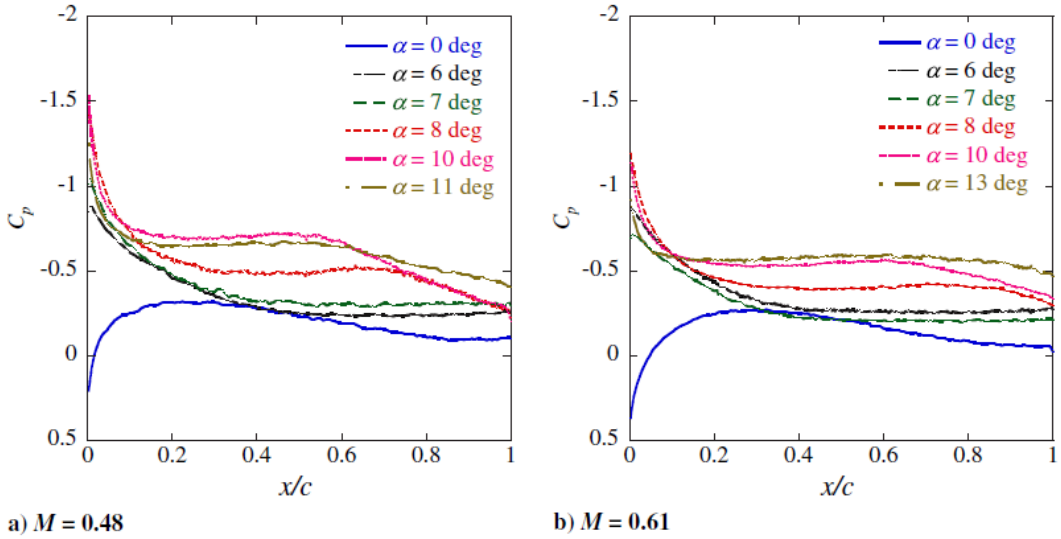

Figure 2.14: (Upper) Pressure distribution of the NACA 0012-34 at a) M = 0.48, and b) M = 0.61. [5]

This is corroborated by Anyoji et al. [5], who tested three Mach numbers at a constant Reynolds number (Re = 1.1×10^4): M = 0.2, 0.48 and 0.61 (Figure 2.15). The initial lift curve slope of each condition does not have any significant deviation from one another, however at higher angles of attack, around α = 7 deg, a noticeable difference occurs: the lower Mach numbers result in a higher maximum lift coefficient, and as a result, a better lift-to-drag performance. This is quite different from the typical results predicted by the Prandtl-Glauert rule, which expects lift coefficients to increase due to compressibility [62]. These results indicate that the Prandtl-Glauert rule does not remain valid for low Reynolds numbers; this is said to be due to the interaction between compressibility and viscosity, which becomes more pronounced at lower Reynolds numbers. This can be seen by comparing the upper surface pressure distributions at M = 0.48 and M = 0.61 (Figure 2.14). The magnitude of the suction peak is depressed due to an increase in M; this is only true for the NACA 0012-34 airfoil, as the flat plate does not elicit the same trend.

Prior to α = 7 deg, the variation in C_L is insignificant for all the considered Mach numbers, and it follows the same non-linear lift curve. This occurs until C_L suddenly increases around an 7 deg angle of attack for M = 0.20; this is similar to the Re effect on the transition process, and can be

attributed to the delayed and aft formation of the laminar separation bubble due to increased boundary-layer stability delaying transition as a result of the increase in Mach number [5, 6]. The increase in boundary-layer stability is noticeable, albeit small, as the decrease in the magnitude of the suction peak impacts the severity of the adverse pressure gradient. This remains the case until the formation of the laminar separation bubble at a higher angle of attack. The Mach number effects on separation, transition, and reattachment locations at various angles of attack for a NACA 0012-34 airfoil can be seen in Figure 2.16. An increase in M is seen to delay transition and reattachment of the shear-layer; which subsequently results in further elongation of the laminar separation bubble (M = 0.48), or prevents any formation at all (M = 0.61). An illustration of this is shown in Figure 2.17. The reasoning for why the maximum lift coefficient decreases as M increases is then due to the delay in transition and its subsequent effect on the separation bubble forming resulting in a reduction of attached flow.

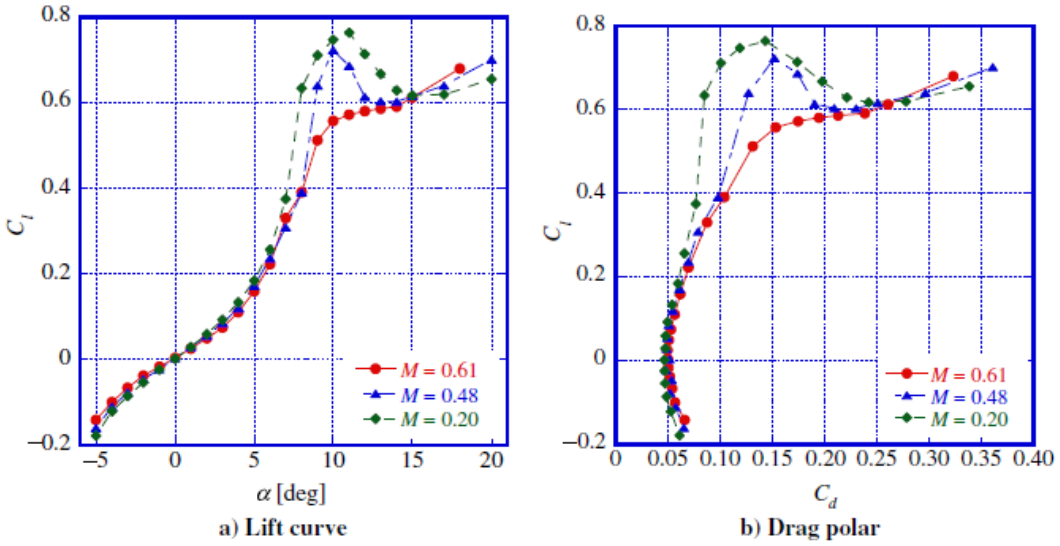

Figure 2.15: Effects of the Mach number on aerodynamic characteristics of the NACA 0012-34 for a constant Reynolds number ($Re = 1.1 \times 10^4$). [6]

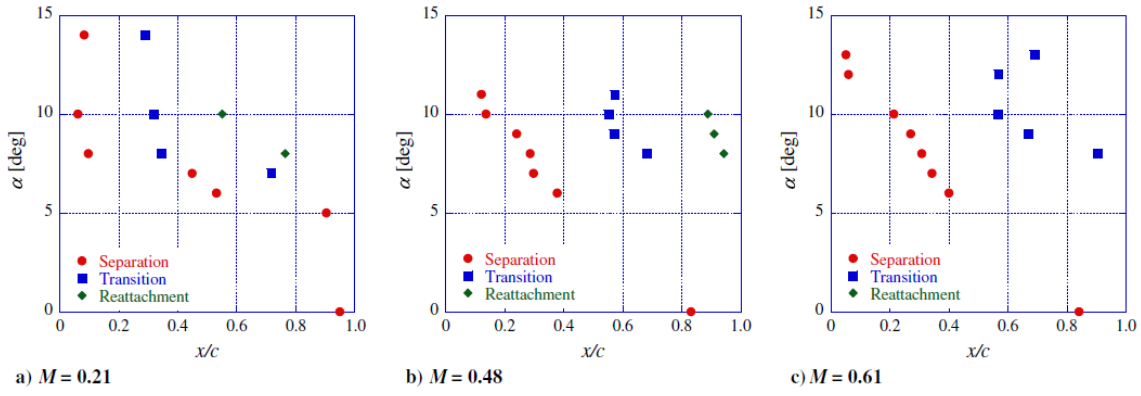

Figure 2.16: Variation of separation, transition, and reattachment locations with the angle of attack for different Mach numbers. [5]

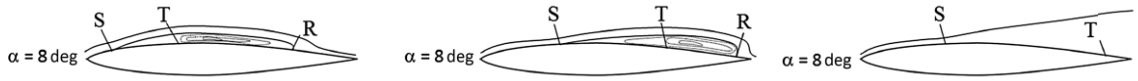

Figure 2.17: Mach effect on the formation of a separation bubble at low Reynolds numbers (M = 0.21, 0.48, 0.61) (Adapted from [5])

The conclusions presented by Anyoji et al. [5] were then corroborated by Suwa et al. [56], who utilized the Mars wind tunnel to conduct experiments on a flat plate and a triangular airfoil in order to ascertain the effects of compressibility at low Reynolds numbers (Figure 2.18). Prior to this study, there was little analysis into how compressibility effects compare at different Reynolds numbers considered representative of Mars (Re = 1×10^3 to 1×10^5). They determined the Mach number effects do not vary greatly across the two Reynolds numbers considered: Re = 3×10^3 and Re = 1×10^4. Figure 2.18shows that the Re and its effects on C_L: the aforementioned kink-point in the lift curve moves to a greater angle of attack as Re decreases. In contrast, the Mach effects do not vary substantially between the two Reynolds numbers: the lower Mach number maintains a lower maximum lift coefficient due to the delay in transition being detrimental to bubble formation.

The experiments conducted by Suwa et al. [56] on the triangular airfoil and their results were then utilized by Munday et al. [39] in direct comparison to their direct numerical simulations (DNS) on the triangular airfoil. Their results are presented in Figure 2.19; as can be seen, a large deviation in the lift and drag polars occurs after the kink point in the lift curve, with some deviation beforehand as well; this is noted to be a result of the flow in the wind tunnel being under the influence of the test-section walls, while the flow described by DNS is span-wise periodic. The aim of their paper was not to match those results, but to be able to correlate the onset of non-linear lift with the flow physics that occurs for compressible flows at low-Reynolds numbers [39].

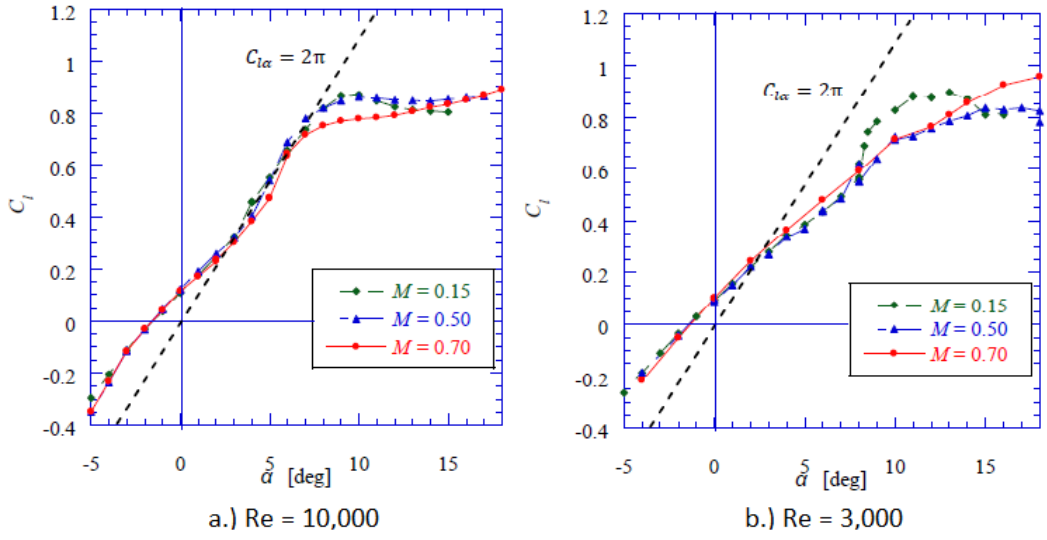

Figure 2.18: Lift coefficient results of force measurements of a triangular airfoil for Re = 10,000 & Re = 3,000 [56]

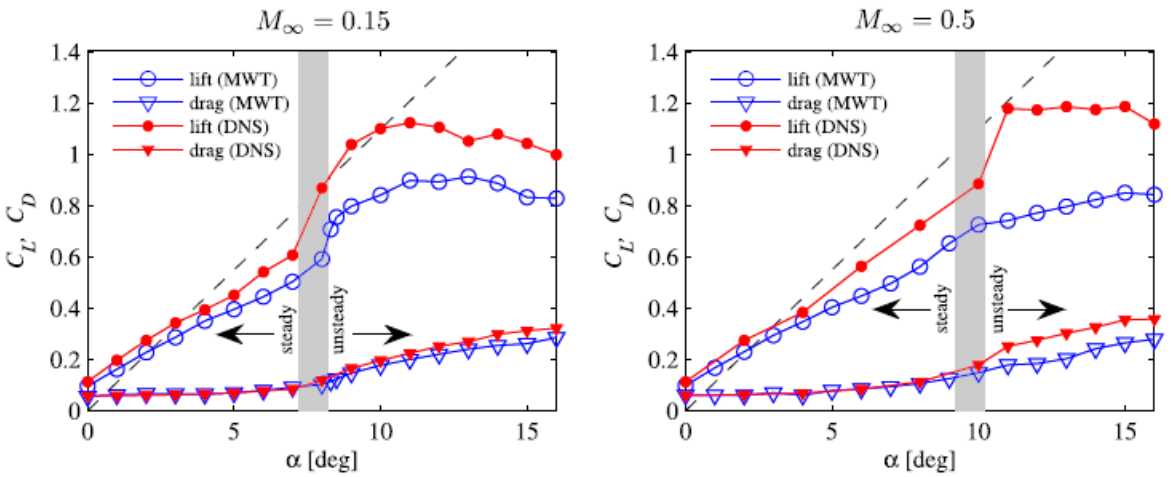

Figure 2.19: Lift and drag coefficients from simulations and experiments. The idealized lift slope CL = $2\pi\alpha$ is also shown (dashed line). [39]

The results obtained from DNS at the low Mach condition (M_∞ = 0.15) compare fairly well with the MWT results; there is the discussed deviation in magnitude, but the shape of the lift and drag polar match. The kink point, denoted as the angle in which the lift curve slope suddenly changes [39], is consistent for both data-sets at $\alpha = 8\,\mathrm{deg}$. Munday et al. [39] describe that the kink point coincides with the movement of the separation point moving from the airfoils apex to the leading edge. The nonlinear lift increase is said to be caused by additional vortical lift due to a roll-up of the leading edge vortex sheet.

While the low-Mach number (M_∞ = 0.15) data-sets appear to compare well with regards to the general shape of the curve, the higher-Mach number condition (M_∞ = 0.5) seems to be less agreeable, albeit still somewhat comparable (Figure 2.19). The DNS results present a clear kink point at 11 degrees, while the time-averaged results obtained from the MWT show a slight nonlinear change at 10 degrees. This difference for both the low and high Mach conditions at angles above the kink point, is explained by the wake behavior, such as reattachment; it is said to be a result of the difference in the span-wise flow conditions between the two data sets. The time-averaged pressure profiles are obtained at the mid-span for the MWT, and span-wise averaged for the DNS, additionally, the thick boundary layer formed on the sidewall forces the flow to be pushed inwards towards the mid-span, altering the behavior of the separated flow in that region [39].

Munday et al. [39] indicate that a large discrepancy exists in the results between their results, and those found experimentally through the MWT [56], along with those that utilize two-dimensional unsteady Reynolds averaged Navier-Stokes simulations (URANS) [68]. Various numerical studies have been conducted on a NACA 0012 airfoil, utilizing URANS models, and have found that the models can capture the characteristics of dynamic stall quite well, such as leading-edge vortices, hysteresis, and secondary vortices in the down-stroke [63]. The issue remains in that dynamic stall is inherently a 3-D phenomenon [54, 63], that requires experimental measurements to be taken to ensure a 2-D flow at the mid-span of the airfoil [63].

Spentzos et al. [54] have conducted a CFD analysis of 2-D and 3-D dynamic stall, and have found a noticeable increase in aerodynamic performance for the 3-D case (Figure 2.20).

The potential impact of this discrepancy is minuscule when considering the aim of this paper: for one, the experimental and numerical references both agree, though Munday et al. [39] argue that the Mars Wind Tunnel is narrow, and thus acts as a pseudo-2-D setup. One of the numerical studies, conducted by Yang & Agarwal [68], state their surprise when discussing the DNS results, though do not go into further detail about their thoughts and opinions. More importantly, however, the purpose of this paper is to ascertain whether there is a relative change or shift in performance due to transonic effects, compared to the high subsonic cases. In this case, as long as the impact of 3-D compared to 2-D results is a simple scaling increase, then one could argue that the relative shift will remain present. In either case, this is something that should be researched further.

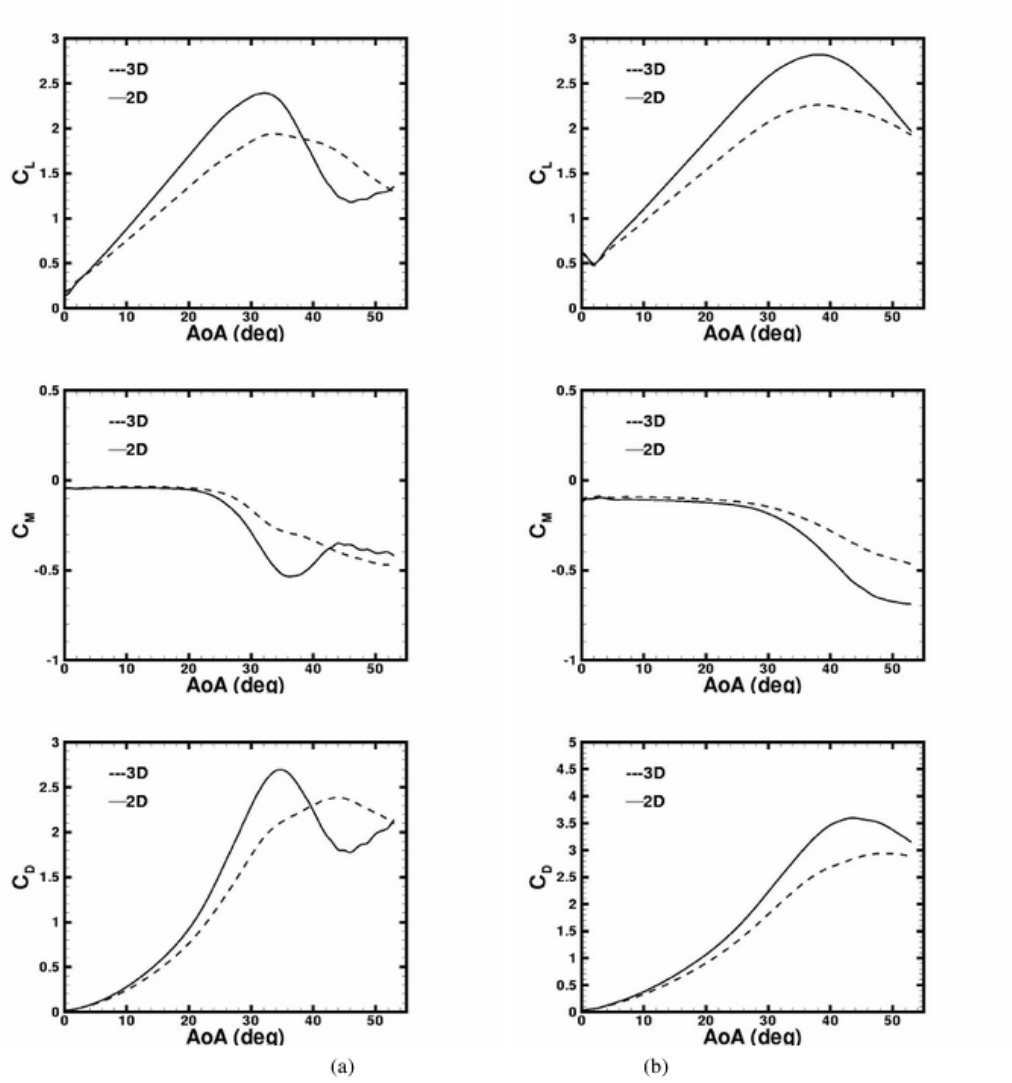

Figure 2.20: Comparison between 2-D and 3-D simulation results for the lift, drag, and quarter-chord moment coefficient of two cases. [54]

2.3. Current Limitations & Knowledge Gap

The wind tunnel construction began in 2007, and is quite small, with a cross-section of 100 mm by 150 mm; additionally, they worked under the assumption that Carbon Dioxide can be solely utilized to model Mars' atmosphere. The wind tunnel allows for a Reynolds range of 2.6×10^3 to 1.3×10^5, with a maximum allowable Mach number of 0.84. The Mars Wind Tunnel has two operational modes: Air and CO_2. For each of these two Modes, there exists an operational envelope; shown in Figure 2.21for Air, and Figure 2.22 for CO_2.

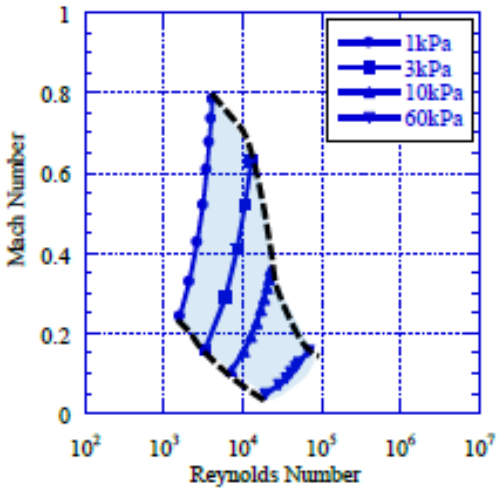

Figure 2.21: Operation Range of the MWT (Air) [56]

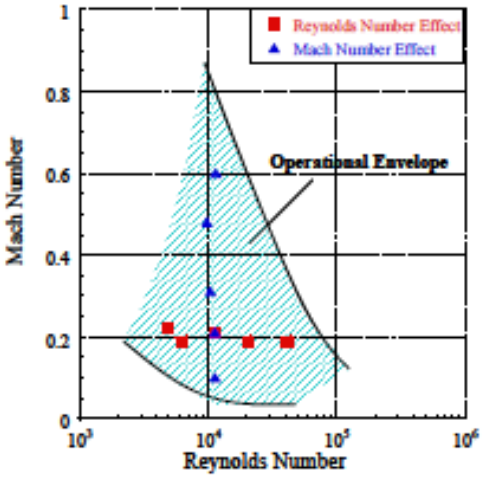

Figure 2.22: Experimental flow condition and operational envelope of the MWT [6]

The wind tunnel has a distinct limitation: the operational range of Reynolds numbers decreases as M decreases, until M = 0.84; this does not allow for any substantial experimental analysis of transonic flight on Mars. Whether this necessitates, or encourages, the development of another Mars wind tunnel is another question. In any case, the lack of experimental studies on transonic flight on Mars is accompanied by a lack of numerical studies as well; despite this, there is some literature discussing transonic flight at low Reynolds numbers; primarily focusing on the shock-wave boundary-layer interactions at these conditions; this literature is presented in Section 2.4.1. Before we look into the effects of transonic flight and shock-wave boundary-layer interactions; the two key non-dimensional numbers and their subsequent effects will be discussed: one in a conventional sense, and then further into the specifics with regards to Martian flight.

Transonic flight on Mars may immediately seem out of the range of feasibility, but numerous examples show that there may be a need for it in the future. Ares [10] was a fixed-wing design for Mars with a design operational range of M = 0.62 to 0.71 at a Reynolds number of about 1×10^5. The AME (Airplane for Mars Exploration) [19] utilized a non-air breathing propulsion system, and was designed to reach high subsonic Mach numbers. The aircraft was tested on Earth at 29 km at Mach 0.8 before disintegrating. There is also the consideration of helicopters on Mars[51] that currently have tip Mach numbers of around M = 0.45, along with Ingenuity

[2], which is designed with tip speeds just below Mach 0.7. There is a strong likelihood that helicopters on Mars could scale up further, and thus experience higher tip speeds as well.

2.4. Transonic Aerodynamics & Shock-Waves

Transonic flow is defined as a domain in which there are three subdomains: subsonic, sonic, and super-sonic; these are illustrated in Figure 2.23. Transonic flow introduces shock waves, which result in the termination of supersonic flow; this sudden change in flow velocity results in a sudden adverse pressure gradient which can affect flow separation and transition, which can result in increased drag (i.e wave drag), shock stall and unsteady effects such as shock oscillations i.e buffeting [62].

Primarily, when defining the lower bound of where transonic flight occurs, the critical Mach number, M_{crit}, is used; it is defined as the Mach number where at the highest local Mach number on the airfoil is at or above the sonic condition (M = 1). This point is important as there is a dramatic increase in drag beyond this point [28, 62]; the drag divergence Mach number is defined as a Mach number beyond M_{crit}, in which there is an exponential increase in drag [28]. Defining the drag divergence Mach number is arbitrary, and multiple definitions have been used; one method it to determine the point at which dC_d/dM = 0.10 [62]. An example of this is shown in Figure 2.24, where an increase in the zero-lift drag coefficient for a NACA 0012 airfoil can be seen. The increase in C_D as a result of wave drag and the subsequent decrease in lift-coefficient past M_{crit} results in a decrease in lift-to-drag performance [12, 52].

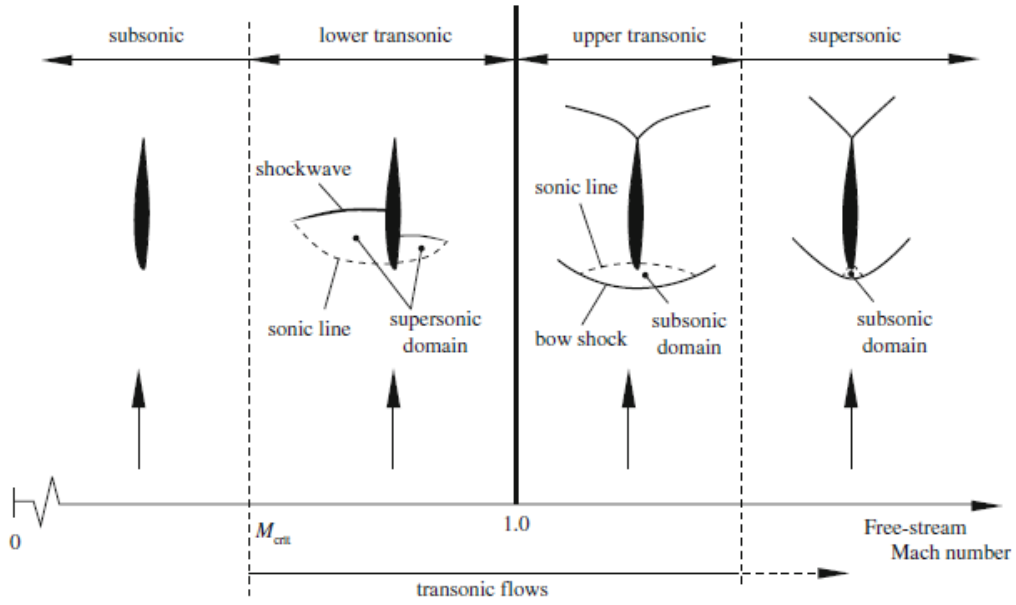

Figure 2.23: Three main stages in the boundary layer physics due to an increasing angle of attack at low Reynolds numbers [5]

The pressure distribution over the airfoil will also be impacted due to the presence of local supersonic Mach numbers. For a subsonic regime, an adverse pressure gradient forms at divergent geometry relative to the angle of attack at which the airfoil is angled; this does not occur for regions where M is locally supersonic. In these conditions, a divergent geometry will result in expansion fans (Figure 2.25), and thus will increase the super-velocities over the wing, and result in a decrease in the pressure coefficient, or in other terms, this expansion fan will delay the suction peak aft until just before the shock-wave occurs [7].

The presence of a weak normal shock, or re-compression shock, is in the design condition of many high-subsonic aircraft [62]. Shock waves on non-lifting bodies are avoided in order to produce wave drag, and separation of the boundary layer on the foot of a shock wave. For a lifting body, (i.e an airfoil) this is not generally the case. A flow crossing a shock wave can cause the following effects: a sudden drop inflow velocity, a sudden increase in pressure, an increase in the flow temperature, and a rise in entropy [18]. An example of the resulting adverse pressure gradient as a result of a shock-wave can be seen in Figure 2.26, which presents the pressure distribution of a NACA 0012 airfoil at M = 0.80.

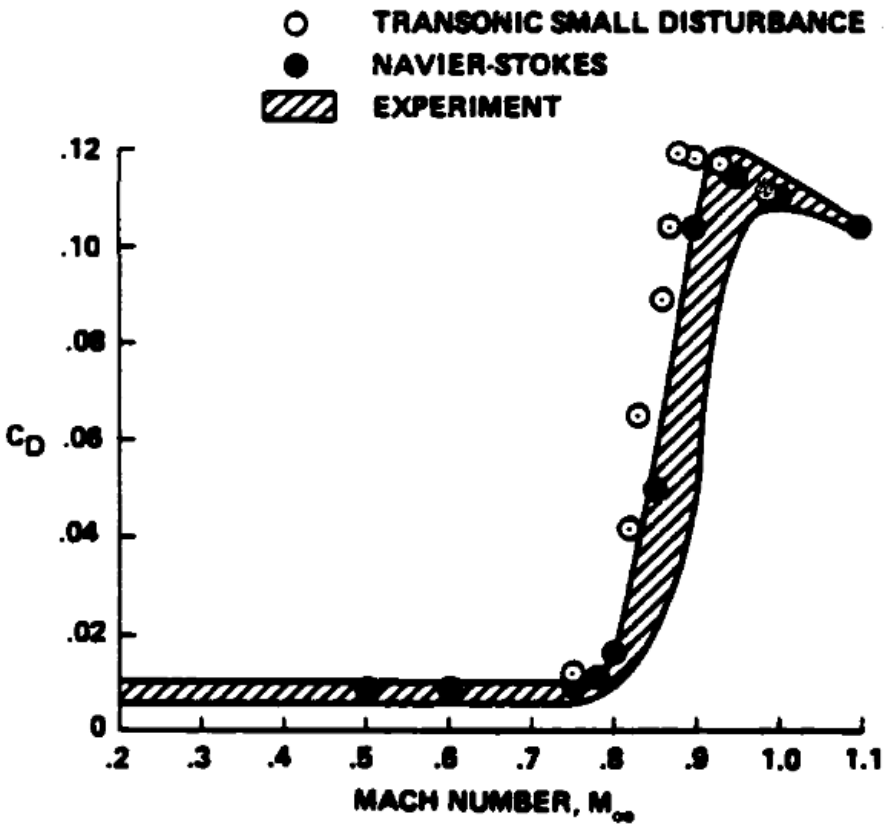

Figure 2.24: Comparison of drag at zero lift for the NACA 0012 airfoil. [33]

The characteristics that describe the boundary-layer, such as the velocity profile and the overall boundary-layer thickness, have a substantial impact on the shock-wave boundary-layer interaction; given that both determine the location of the sonic line within the boundary-layer. The sonic line is the wall distance at which the velocity within the boundary-layer is greater than the speed of sound, or M = 1. Within the subsonic region, information can travel upstream, and thus impact the flow there as well; a larger subsonic region will result in an increased upstream influence length [7]. Additionally, the strength of the shock can result in different interactions; in general, there are two interactions a shock wave can have on a flow: a weak interaction, and a strong interaction [62].

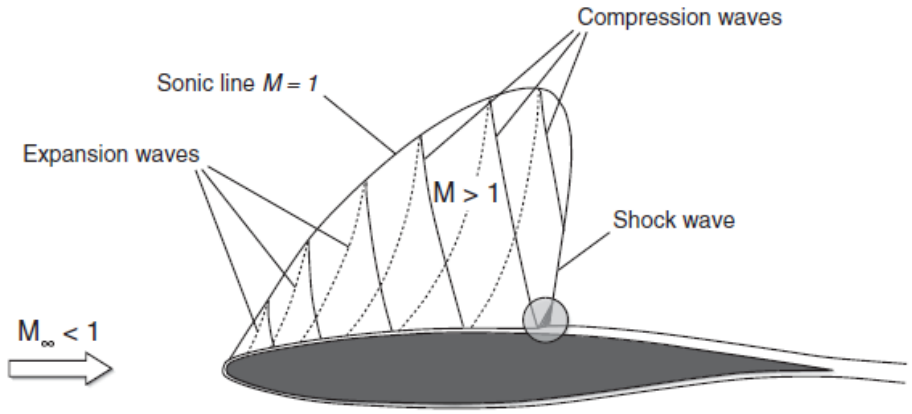

Figure 2.25: SBLI on transonic wing. [7]

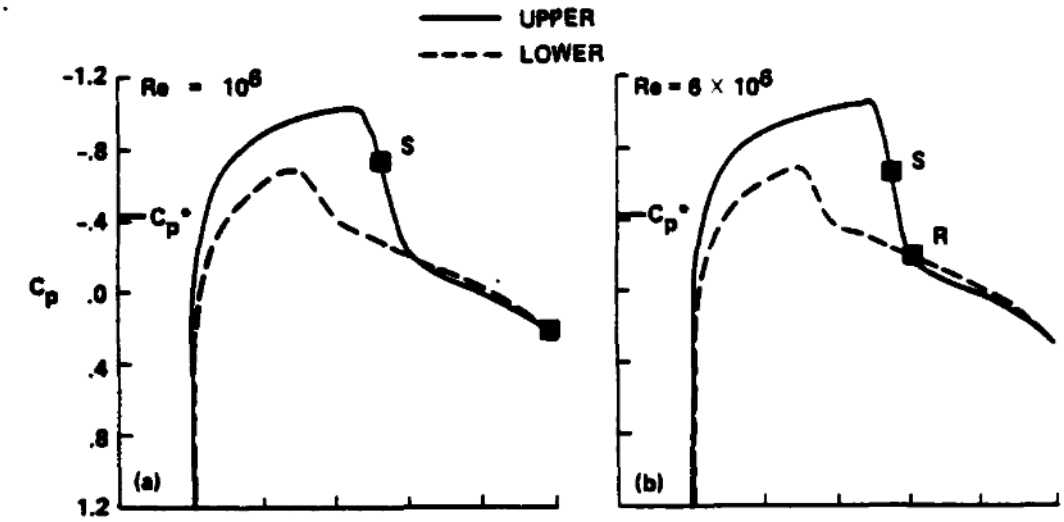

Figure 2.26: Pressure distributions on the NACA 0012 airfoil at M = 0.80 and α = 1 deg. [33]

2.4.1. Transonic Aerodynamics on Mars

Analyzes of transonic flow at low Reynolds numbers have been conducted, but for comparatively high Reynolds numbers: $Re > 2.5 \times 10^5$ [20]; for the conditions expected on Mars, there appears to be a noticeable lack of experimental or numerical studies. There, however, exists some literature from which some information can be derived. Direct numerical simulations were also conducted at Reynolds numbers between 50 and 300 to analyze the effects of subsonic to supersonic flow over a sphere [41]. Another recent study considered Reynolds number as low as 4.4×10^5, though this is based on the boundary layer growth length, and not a full chord length. A recent study considered high-subsonic Mach numbers up to $M = 0.8$, at single Reynolds number of Re $\approx 2 \times 10^5$ [67]. They used a RANS solver to simulate flow around an E387 airfoil and determined the appearance of shocks at Mach 0.7. The separation point due to the shock-wave boundary layer interaction is observed to cause a forward movement of laminar separation and transition.

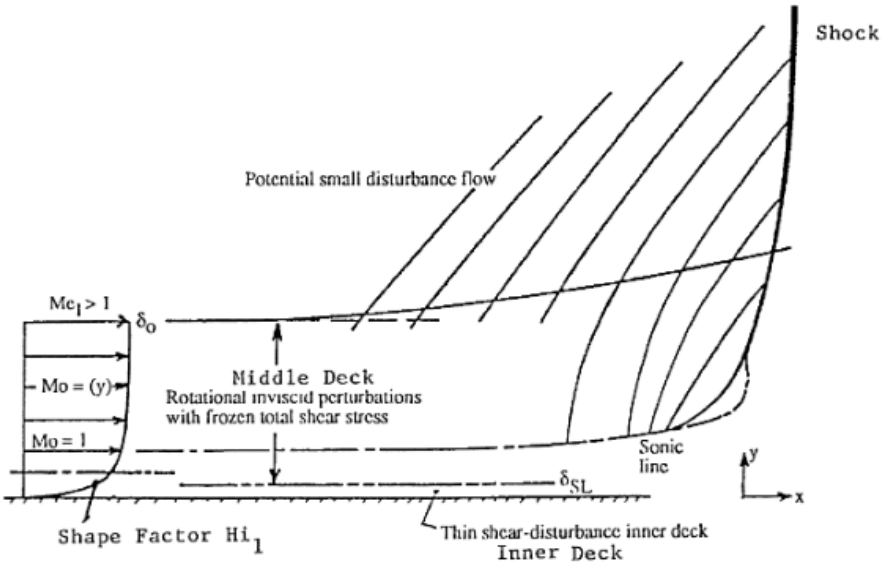

Figure 2.27: Triple-deck structure of interaction zone. [59]

Aside from these and other similar studies, there has been limited experimental or numerical analysis in transonic Mach numbers at the low Reynolds numbers typical for Mars. Theoretical research into transonic Mach numbers at low Reynolds numbers has been done [59], with Reynolds numbers ranging from 1×10^3 to 1×10^6. Additionally, the boundary-layer is heavily dependent on Re, and in turn, a lot of information can be derived through how the boundary-layer interacts with a shock-wave [7]. The effect of small disturbances due to a weak external shock on some incoming turbulent boundary layer were considered [59]. They utilized triple-deck theory, which describes the interaction zone of a shock and a turbulent boundary layer. The theoretical model indicates that as Re decreases, there is an increasing influence on the change in wall pressure, displacement thickness growth, and local skin friction, C_f, (Figure 2.28). The pressure change across the shock-wave at low Reynolds numbers is reduced in magnitude; the displacement thickness, while larger due to a lower Reynolds number, also

exhibits the same behavior due to the shock-wave.

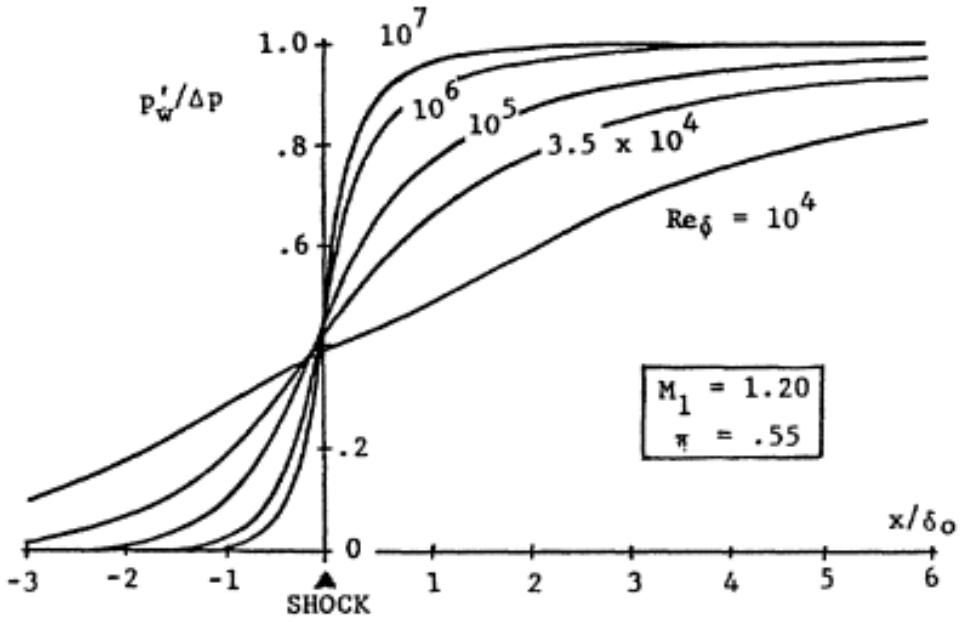

Figure 2.28: Change in pressure across a shock wave at various Reynolds numbers. [59]

Why this occurs is related to how a change in curvature impacts compressibility. A ramp with a concave curvature will induce compression waves, that coalesce into a shock, but the point at which they coalesce away from the ramp depends on the length of the ramp, or in other terms, the curvature. A gradual change curvature spreads out compression waves more than an abrupt change in curvature, thus the waves coalesce further away, and in turn, the shock occurs further away [7]. The sonic line within the boundary-layer acts as the boundary, and such defines the curvature for which the compression waves develop. An illustration of this is illustrated in Figure 2.30. Additionally, The lower Reynolds number flow alters the boundary layer in a few ways, which in turn influences the interaction of the shock-wave with the boundary-layer. For one, a reduction in Reynolds number results in a thicker boundary layer, and thus the sonic line occurs further from the surface resulting in a larger subsonic region.

The thickness and velocity profile of the boundary-layer can impact the location of the sonic line within the locally supersonic bulk flow. As Re decreases, the boundary-layer thickness increases, and the laminar boundary-layer becomes increasingly stable. The increase in the former would result in the sonic line moving further away from the wall, and the latter would see an increase in the amount of laminar flow. A laminar boundary layer has a different velocity profile compared to a turbulent boundary layer, which would result in the sonic line moving away from the wall than when compared to the turbulent boundary-layer [7].

The low Reynolds shock-wave boundary-layer interactions result in something similar to shock control, where the overall impact of the shock on the pressure change is reduced. This is due to, again, a gradual curvature smearing the shock, but instead of the boundary layer, the actual curvature of the wall acts as the shock control (Figure 2.29). The sonic lines location is seen to impact the upstream influence length, or as in, how far upstream does the downstream information travel upstream of the shock. A decrease in Reynolds number seems to result in a larger upstream influence, which in effect results in the shock interaction to progressively spread out the effects of key flow parameters [59]. Other studies have looked into the effects of laminar boundary-layer shock-wave interactions, and have determined an increase in flow instabilities, which would result in the transition of the boundary-layer [9, 24].

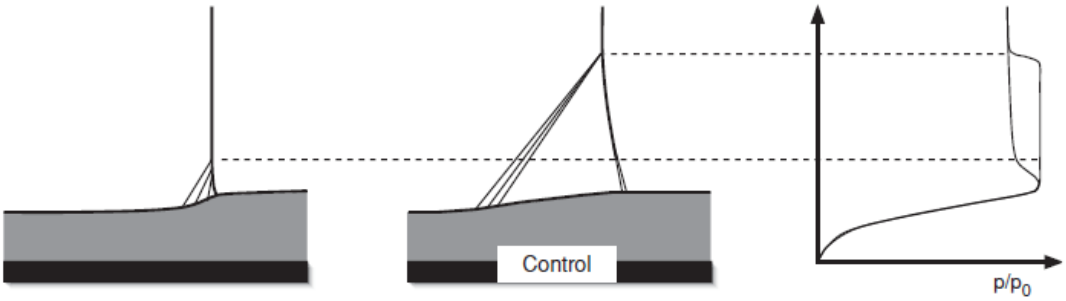

Figure 2.29: Basic mechanism of shock control and illustration of its impact on pressure [7]

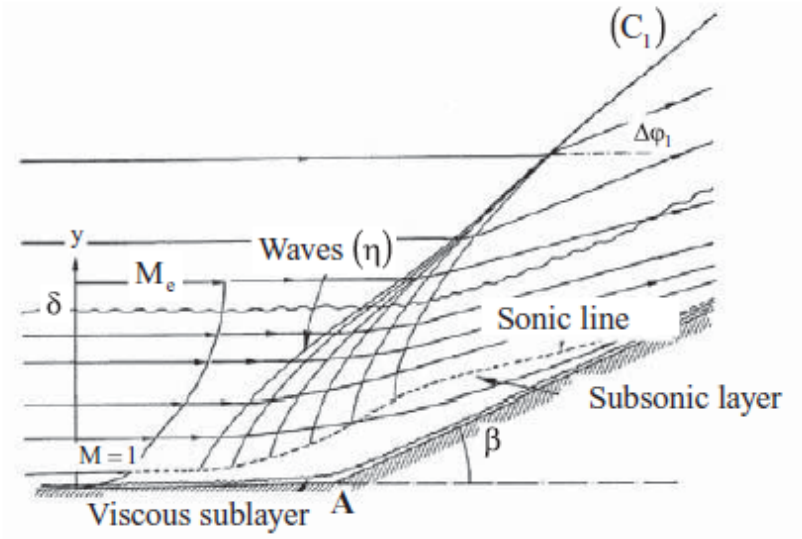

Figure 2.30: Ramp-induced shock without boundary-layer separation. [7] The sonic line and its impact on the formation of compression waves is illustrated here.

3 Formulation of Research & Methodology

The effect of low Reynolds numbers on the flow physics appears to be consistent between Earth and Mars, as the atmospheric composition, through the specific heat ratio, has been seen to not impact the performance or flow physics in any noticeable way. Thus low Reynolds number incompressible flows are seen to be consistent. The effect of compressibility at low Reynolds numbers appears to be a point of interest, as it does not follow the expected Prandtl-Glauert scaling. The effects of compressibility at low Reynolds numbers are also shown to not vary due as a result of the Reynolds number; for the considered conditions at the very least.

The key flow phenomenon of interest for subsonic flight on Mars is the stability of the boundary-layer, or rather where transition of the boundary-layer occurs. This defines whether the formation of a laminar separation bubble occurs, and in turn, defines the amount of attached flow over the airfoil. Other secondary factors to consider are the changes in skin friction coefficient, the separation point, and the pressure distribution due to changes in the Mach and Reynolds number; this is especially in regards to the decrease in the magnitude of the suction peak due to Reynolds and Mach number effects. As the increase in boundary-layer stability is so substantial in determining the aerodynamic performance of a given airfoil in subsonic flight; for transonic flight, a few differences occur, primarily with regards to the shock-wave, but also with regards to the existence of a potential expansion fan in regions of locally supersonic flow.

Questions form on whether transonic flight, and the subsequent shock-wave boundary-layer interaction that occurs, has a substantial consequence on the aerodynamic performance of a wing in the atmospheric conditions of Mars, and what effects on various flow phenomena result in these effects. A hypothesis is that a shock-wave is a clear destabilizing feature when it comes to boundary-layer stability, primarily due to the sudden adverse pressure gradient; however, this adverse pressure gradient is mitigated due to what we know happens at lower Reynolds numbers: a smoothing out and diminishing of the shock-wave boundary-layer interaction. This can be juxtaposed to the delay in the adverse pressure gradient due to the presence of the expansion fan as well, which would delay separation to after the foot of the shock, and thus likely transition would be delayed until after as well.

Ideally, we can separate the hypothesis into two components; the impact of the expansion fan, and the impact of the shock-wave. The expansion fan should push the adverse pressure gradient aft at increasing Mach numbers, and thus reduce the amount of trailing edge separation at low angles of attack. The shock-wave, while diminished in its interaction with the boundary layer due to a potential lambda structure, still would provide an adverse pressure gradient, which could introduce instabilities in the boundary-layer and result in earlier transition when compared to a hypothetical high-subsonic counterpart. From these two possible directions

could follow, we see an overall forward movement of the transition point, and thus the reintroduction of a laminar separation bubble for high Mach numbers, or we could see an increase in overall boundary-layer stability. With regards to separation, we would expect it to move aft due to the expansion fan, which would increase the amount of attached flow; however whether this would be a positive consequence in and of itself would be directly tied to the overall impact of the shock-wave boundary-layer interaction, and in how detrimental it is to aerodynamic performance due to wave drag as a result of momentum loss in the boundary-layer.

3.1. Research Questions

1. **Given the atmosphere composition of Mars, can the introduction of a shock wave improve aerodynamic (L/D) performance by inducing a delay in separation and/or earlier transition of the laminar boundary layer?**

   (a) What are the relevant Reynolds & Mach number effects at the atmospheric conditions on Mars?

      i. How does a change in either the Reynolds or Mach number affect the interaction between the shock wave and the boundary-layer?

      ii. How does a change in either the Reynolds or Mach number impact boundary-layer separation?

      iii. How does a change in either the Reynolds or Mach number influence the stability of the boundary-layer?

3.1.1. Quantification of Research Objectives

The research questions set out by the hypothesis need to be quantified in a manner that can answer them objectively. Determining whether the aerodynamic performance improves is straightforward; typically this is described as an increase in lift-to-drag performance. Whether or not the performance improves or not is not useful in and of itself; determining and understanding why is just as imperative. The conditions on Mars illustrate that the Reynolds and Mach numbers are by far the most influential parameters on the performance through their impact on boundary-layer behavior. As the Mach number is inherently connected to the development of a shock-wave, the effects of an increasing Mach number are necessary to ascertain. The Reynolds number is connected heavily to the behavior, shape, and overall profile of the boundary-layer; in turn, the Reynolds number affects the interaction between the shock-wave and the boundary-layer.

How either similarity parameter influences the interaction between the shock-wave and the boundary-layer is important to understand; this can be quantified through many methods: the location of the shock wave, the impact of the shock wave on the pressure distribution, and the

impact of the shock wave on momentum loss in the boundary-layer. The separation point is dependent on the shock-wave due to the subsequent adverse pressure gradient; the separation point can be illustrated through the skin friction coefficient; a negative skin friction coefficient indicates flow reversal. The stability of the boundary layer is a complex problem that cannot be analyzed in detail due to the methodological limitations discussed in Chapter 4.6. Certain conclusions can be made through an analysis of the shape factor and the behavior of the vortex shedding. A decrease in shape factor is indicative of boundary-layer transition. The later stages of transition play a significant role in the vortex development in a separated shear-layer at low Reynolds numbers; How the Strouhal number changes, or not, is indicative of the behavior, and chord-wise position of boundary-layer transition.

3.2. Airfoil Selection

Selecting an airfoil is a trade-off between multiple criteria: experimental data, depth of literature, ease of simulation, applicability, and viability are all examples of what influences the choice of which airfoil to select. Only three options have data applicable to the topic at hand: a flat plate, a triangular airfoil, and a NACA 0012-34 airfoil.

Figure 3.1: Illustration of the NACA 0012-34 Airfoil

The only viable option is the NACA 0012-34 airfoil (Figure 3.1), as neither the flat plate nor the triangular airfoil will provide insight into the movement of the shock-wave, or separation location.

$$\begin{aligned} \pm y_t &= a_0\sqrt{x} + a_1 x + a_2 x^2 + a_3 x^3 && \text{ahead of } t_{\max} \\ \pm y_t &= d_0 + d_1(1-x) + d_2(1-x)^2 + d_3(1-x)^3 && \text{aft of } t_{\max} \end{aligned} \tag{3.1}$$

The NACA 0012-34 airfoil is defined by two analytical equations given below in Equation 3.1. The a and d coefficients are presented in Table 3.1 [13, 49].

a_0	a_1	a_2	a_3	d_0	d_1	d_2	d_3
0.14845	0.193233	-0.55817	0.283208	0.002	0.315	-0.23333	-0.03241

Table 3.1: Coefficients defining the NACA 0012-34 airfoil

3.3. Parameter Definition

Determining the displacement and momentum thickness' are important parameters in helping understand the boundary-layer profile, and overall development of the boundary layer. Both parameters were presented in Section 2.1 alongside their respective equations, The key point of interest is determining the velocity tangential to the airfoil wall, as this is the value utilized for velocity in each equation; this is done by translating the curvature of the airfoil at any specified location to that of a flat plate equivalent. In order to do this, the analytical equations defining the NACA 0012-34 airfoil are utilized in order to find the slope, and in turn the angle at any discrete point along the surface of the airfoil (Equation 3.2).

$$\begin{aligned} \frac{dy_t}{dx} &= 0.5a_0x^{-0.5} + a_1 + 2a_2x + 3a_3x^2 && \text{ahead of } t_{\max} \\ \frac{dy_t}{dx} &= -d_1 + -2d_2(1-x) + -3d_3(1-x)^2 && \text{aft of } t_{\max} \end{aligned} \tag{3.2}$$

The angle is then determined (Equation 3.3); the angle can then be considered with the angle of attack to determine the slope, and as such can be utilized to define a line of points tangentially from the surface; the lines are then generated for a discrete number of points evenly along the chord (Figure 3.2).

$$\phi = \arctan \frac{dy_t}{dx} \tag{3.3}$$

The x- and y-components of velocity are then transformed into the normal and tangential components. From here the computation of the displacement and momentum thickness', and in turn, the shape factor can be done. This angle can then be used to determine the skin friction coefficient from both x- and y-components of the wall shear stress.

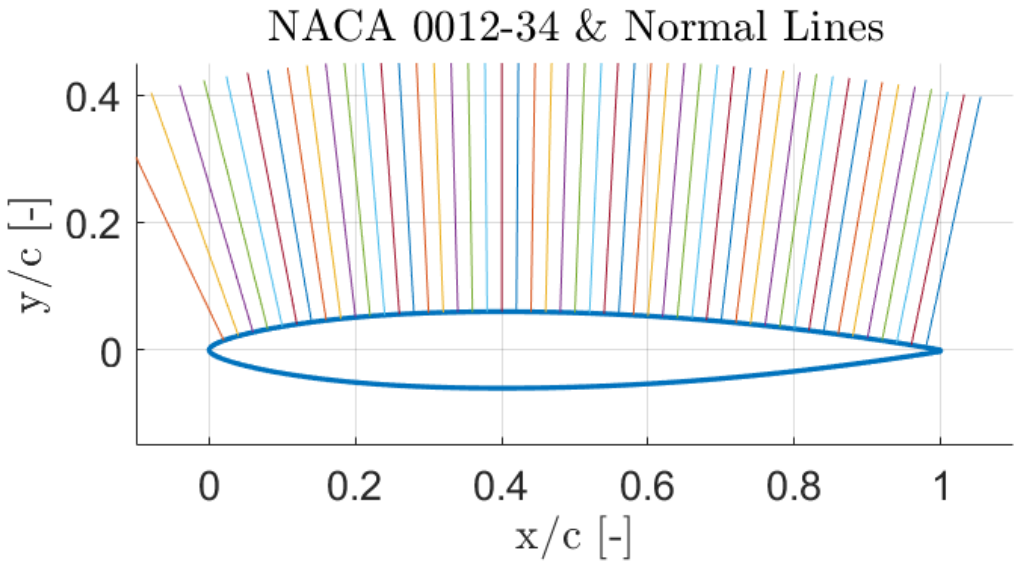

Figure 3.2: Example of 50 lines normal to the local curvature of the airfoil; these lines are utilized to determine the normal and tangential velocities at the wall.

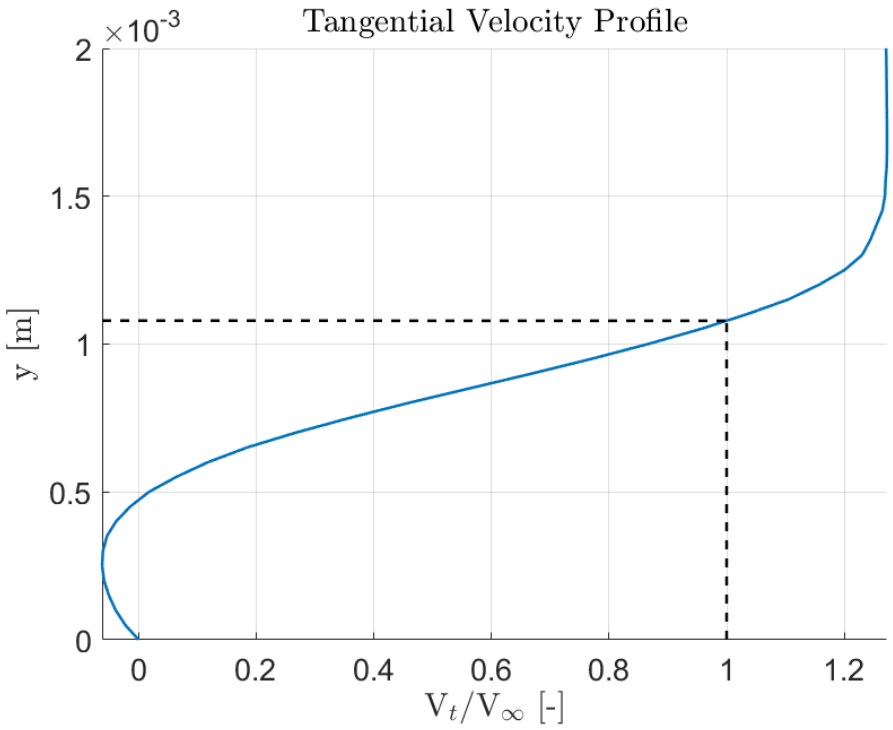

Figure 3.3: Example of a tangential velocity profile non-dimensionalized to the free-stream velocity

3.3.1. Displacement & Momentum Thickness

Defining the displacement and momentum thickness relies on defining which velocity is used to determine the upper bound of the integration, U_e [65]. This velocity can be defined as the free-stream velocity U_∞, and thus the wall distance at which the velocity in the boundary layer reaches said value defines the upper bound (Figure 3.3. Another method is to consider the maximum tangential velocity within the velocity profile [65], but this can be impacted by the angle of the shock.

3.3.2. Force Coefficients

The lift and drag coefficients are defined by the x- and y- directions of the force on the airfoil, transformed to the inflow angle of attack. Where S is the surface area, defined by the chord length, c, multiplied by the span-wise width of the computational domain (Chapter 4.2).

$$C_L = \frac{F_y \cos\alpha - F_x \sin\alpha}{\frac{1}{2}\rho_\infty U_\infty S} \tag{3.4}$$

$$C_D = \frac{F_x \cos\alpha + F_y \sin\alpha}{\frac{1}{2}\rho_\infty U_\infty S} \tag{3.5}$$

3.3.3. Skin Friction Coefficient

The skin friction coefficient is defined by non-dimensionalizing the shear stress at the wall, τ_w with the dynamic pressure. the wall shear stress is given in x- and x- components, and thus the same change in the reference frame is done for every discrete position along the airfoil surface. At this point, the tangential value is used for τ_w.

$$C_f = \frac{\tau_w}{\frac{1}{2}\rho_\infty V_\infty^2} \tag{3.6}$$

3.3.4. Shock-Wave Location

As mentioned in the Chapter 2.4.1, the shock location is different to ascertain based on what occurs at the wall; this is due to the smearing effect of the shock-wave boundary-layer interaction. In either case, the development of the shock can still be seen by considering the adverse pressure gradient, and the suction peak, $C_{P,min}$. The shock occurs after the suction peak due to the preceding expansion fan; thus, $C_{P,min}$ is the location that will be used as the beginning of this interaction. Further discussion at the shock-wave boundary-layer interaction at low Reynolds numbers can be seen in Appendix A.

3.3.5. Strouhal Number & Frequency Analysis

Another parameter considered is the Strouhal number. The Strouhal number is a non-dimensional number describing oscillating flow problems (Equation 3.7) [23]; it is especially useful for analyzing the vortex shedding, and can be utilized as a method to validating the solution.

$$St = \frac{fd}{U_\infty} \tag{3.7}$$

The frequency, f, is typically found by means of a frequency analysis, where the sampling frequency is determined by the time-step of the problem. In this case, the frequency is that of the vortex shedding. The reference length, d, is determined by the cross-section of the airfoil chord, c, projected onto the cross-stream plane.

$$d = c \sin \alpha \tag{3.8}$$

The frequency was extracted using the time history of the lift coefficient The time-step is also used to determine the sampling frequency, f_s, and in turn the Nyquist frequency, f_n (Equation 3.9) [4].

$$f_s = \frac{1}{\Delta t} \text{ and } f_n = \frac{f_s}{2} \tag{3.9}$$

The number of frequency points is determined by half the number of time-steps, N; the value at each frequency point is a uniform range from 0 Hz to the Nyquist frequency. After this, the mean value of the lift coefficient was subtracted, and then a fast Fourier transform was used to convert it into spectral components. The spectral lift coefficients are then divided by the number of time-steps, N, and then plotted against the frequency points. A sufficient number of periods is used in order to extract a clear value; an example is shown in Figure 3.4. Time is non-dimensionalized by the time it takes a particle of air in the free-stream to travel one chord length (Equation 3.10).

$$t_c = t\frac{U_\infty}{c} \tag{3.10}$$

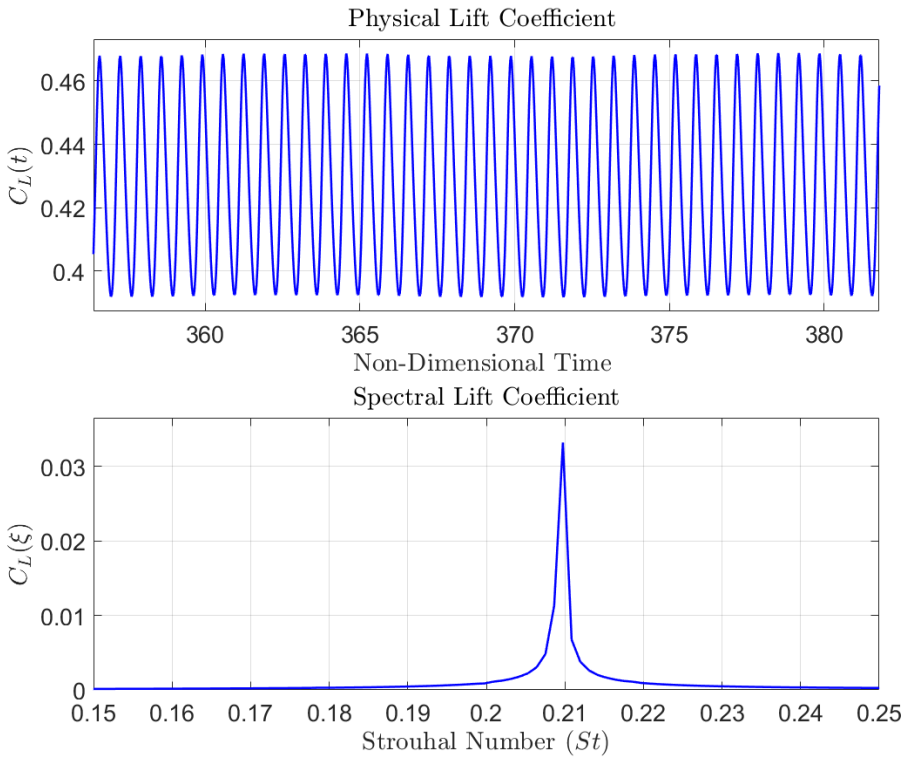

Figure 3.4: Frequency analysis of the lift coefficient illustrating the vortex shedding frequency and Strouhal number for the validation case: M = 0.61 & Re = 1.1×10^4

3.4. Selection of Test Conditions

In order to determine the effect of transonic Mach numbers at low Reynolds numbers, a test matrix has to be set up in a way that can compare Mach number effects, and Reynolds number effects. Determining which Mach numbers are ideal for determining the effects of transonic flow at low Reynolds numbers. The largest Mach number considered for the NACA 0012-34 airfoil was M = 0.61 [5]; for the triangular airfoil, this value was M = 0.70. Determining the value of the critical Mach number is typically estimated through the use of Prandtl-Glauert scaling

[62]. The results so far indicate that the Prandtl-Glauert correction in fact over predicts the compressibility effects at low Reynolds numbers. This implies a decrease in the suction peak as the Mach number increase; this suggests that the critical Mach number should be higher at low Reynolds numbers. To be sure, a full range of the low transonic flight will be considered, with Mach numbers ranging from M = 0.70 until M = 0.95, with ΔM = 0.05 as the resolution.

The Reynolds number range on Mars is shown to be between Re = 1×10^3 to 1×10^5, depending on the vehicle. The NACA 0012-34 airfoil has experimental and numerical results at Reynolds numbers 1.1×10^4; selecting these two Reynolds ranges would be ideal; additionally, the blade tips of rotor-craft would be in the range of Re $\approx 1\times10^4$ The higher velocities associated with the increased Mach number could push the Reynolds number further towards an order of Re = 2×10^5, which would make this an interesting case as well for larger fixed-wing Martian aircraft. For standard Martian conditions at a Mach number of 0.85, these Reynolds numbers would result in chord lengths ranging from $1.5\,\mathrm{cm}$ to $100\,\mathrm{cm}$. The Reynolds numbers selected did not have a large variation between them, as resolution would be lost; as such the Reynolds numbers selected will focus on the lower end of the realistic range.

Anyoji et al. [5] illustrate that the angle where the Mach number effects are most noticeable is at $10\,\mathrm{deg}$, while for Reynolds effects, this angle is at $6\,\mathrm{deg}$. Studying all possible angles in order to gauge the Reynolds and Mach number's general impact on performance is inefficient and beyond what is necessary to understand the topic at hand. At $8\,\mathrm{deg}$ both a change in Reynolds and Mach numbers present clear changes in the lift coefficient, and lift-to-drag ratio; as such, an angle of $8\,\mathrm{deg}$ was selected, as it offers a good midpoint for analyzing Mach and Reynolds effects. The test conditions are presented in Table 3.2. Further data points may be considered if necessary. The equivalent chord length is the chord length required to satisfy the Mach and Reynolds numbers at sea-level conditions on Mars; in the simulations, the density is varied in place of the chord length.

Mach Number, M [-]	Reynolds Number, Re [-]	Equivalent Chord Length, c [mm]
0.70	1.1×10^4	44.4
0.75	1.1×10^4	41.4
0.80	1.1×10^4	38.8
0.85	1.1×10^4	36.5
0.85	2×10^4	66.4
0.85	3×10^4	99.6
0.85	4×10^4	132.8
0.90	2×10^4	62.7
0.90	1.1×10^4	34.5
0.95	1.1×10^4	32.7

Table 3.2: The considered test conditions: at α = $8\,\mathrm{deg}$. The equivalent chord length is the length required to maintain the same Reynolds and Mach number at a constant sea-level density on Mars

4 Computational Methodology

Any experimental analysis is unfeasible due to the limitations of the current facilities in their ability to realize the effects of transonic flight on Mars; additionally, the time and resource constraints do not allow for any substantial experimental development. With these considerations in mind, the only option remaining is to conduct a numerical study.

Most of the studies considering flight on Mars utilize two-dimensional unsteady Reynolds averaged Navier-Stokes (2-D URANS) simulations ; to be more precise, they consider the condition unsteady only above an angle of attack of around, α = $5\,\mathrm{deg}$ [55, 68]. One study, as previously mentioned in Section 2.1.2, utilized direct numerical simulations (DNS) [39], though their results are inconsistent for angles of attack above α = $5\,\mathrm{deg}$ due to what they state to be due to three-dimensional unsteady phenomena [39].

Sugar-Gabor & Koreanschi [55] considered a NACA 0012-34 airfoil for their simulations; they utilized 2-D URANS for the purposes of optimizing an airfoil for subsonic flight on Mars, and validated their model against the experimental results of the Mars wind tunnel. In any case, all the 2-D URANS setups appear to be accurate in comparison to their experimental counterparts. A two-dimensional unsteady Reynolds-averaged Navier-Stokes approach would be ideal; the limitations of 2-D URANS are apparent and must not be understated; The accuracy of the problem is sacrificed for computational efficiency, and as such all results should be viewed relative to one another.

4.1. Numerical Solver Selection

As the problem definition is fairly straightforward, commercially available numerical solvers can be used. The commercial software available for use are Fluent 19.1 and CFX 19.1, with the TU Delft having licenses for both. SU2 and OpenFoam are additional options as well, though due to the lack of familiarity with the SU2 and OpenFoam, they were not considered. Either option is sufficient, as neither seems to be substantially different in terms of their use cases or results [1]; One thing to note is CFX 19.1 is incapable of 2-D simulations in an absolute sense, and require one cell width in the span-wise direction; this is sometimes colloquially referred to as ”2.5”-D; but it is effectively 2-dimensional. CFX 19.1 was selected as the solver for use, alongside ICEM CFD 19.1 for mesh development.

4.1.1. Discretization Method

ANYSYS CFX 19.1 offers three schemes for advection and turbulence: A first-order scheme, high-resolution scheme, and a scheme with a specified blend factor. The high-resolution scheme utilizes a variable blend factor,?? , in order to balance between the first and second-order schemes, while the specified blend factor specifies a constant value of β between 0 and 1. ANSYS recommends the high-resolution scheme when possible. The scheme implemented in ANSYS CFX is shown in Equation 4.1.

$$\varphi_{ip} = \varphi_{up} + \beta \nabla \varphi \cdot \Delta \vec{r} \tag{4.1}$$

The transient schemes available are first-order backward Euler and second-order backward Euler. As the studied conditions exhibit strong unsteady behavior, the second-order scheme is utilized.

4.2. Domain Sizing

Yang & Agarwal [68] performed two-dimensional numerical simulations utilizing a rectangular grid, in the same fashion as Munday et al. [39], who utilized a domain size of (x; y; z) ∈ [−10c; 20c] × [−10c; 10c] × [−0.15c; 0.15c]. They considered that the past research concluded that the M_∞ = 0.15 had a free-stream that was nearly incompressible, and thus velocity inlet and pressure outlet boundary conditions were prescribed; for the top and bottom boundaries, a free stream boundary condition was applied. The M_∞ = 0.5 case employed the use of a pressure far-field boundary condition for the inlet, outlet, top, and bottom boundaries, with a no-slip wall boundary condition used for both Mach numbers. A domain size of (x; y; z) ∈ [−10c; 20c] × [−10c; 10c] × [-0.025c; 0.025c] was generated, with one cell width in the span-wise (z) direction in order to utilize a 2-Dimensional approach in Ansys CFX 19.1. The chord length was selected to be 0.05 meters, matching that of the Mars Wind Tunnel [5]. The boundary conditions were selected to match those of the compressible case used by Yang & Agarwal: a total pressure inlet with a specified flow direction, a static pressure outlet, a static pressure opening for the far-field, an adiabatic wall for the airfoil, and a symmetry condition in the span-wise direction.

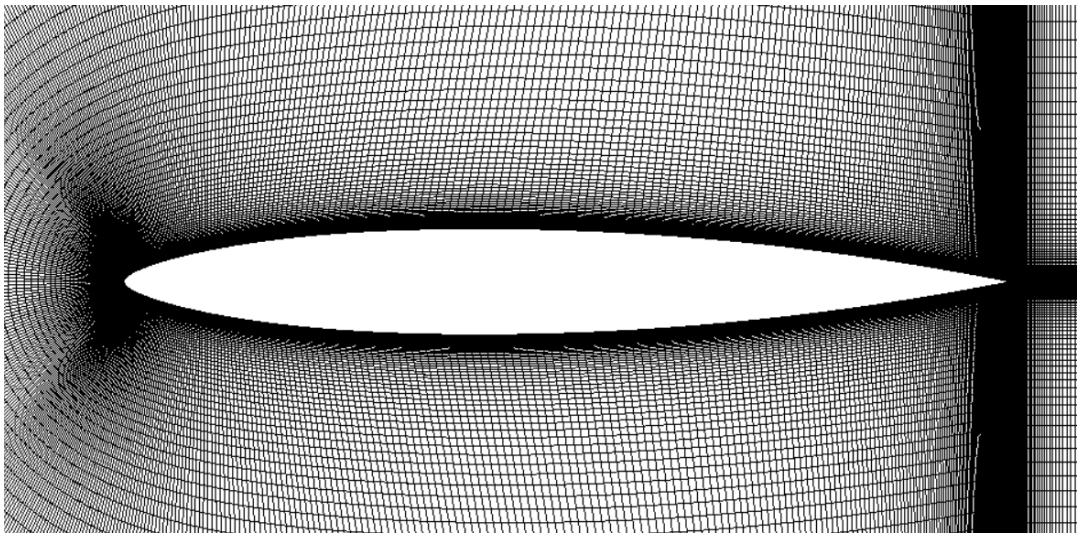

Figure 4.1: Close up of airfoil: Medium mesh refinement [149,592 cells]

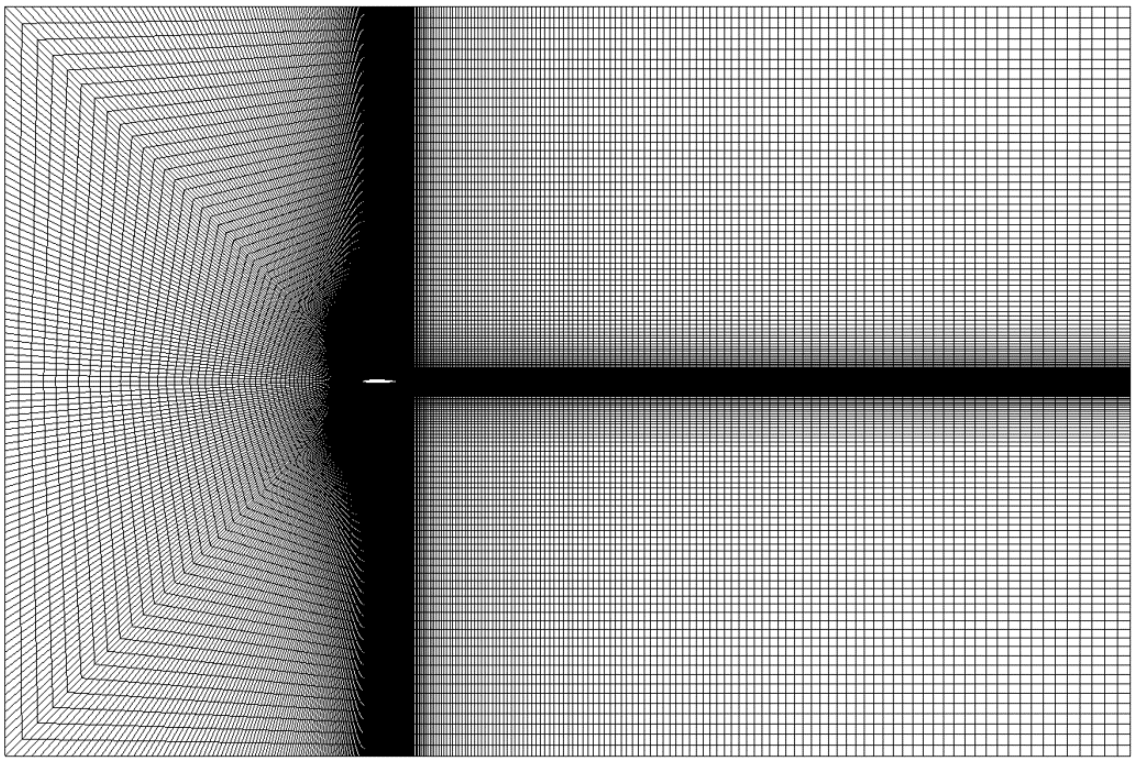

Figure 4.2: Full domain: Medium mesh refinement [149,592 cells]

4.2.1. Mesh Quality

A reasonable level of mesh quality is important to ensure that the simulation is both accurate and resource-efficient. There are certain parameters that can help determine the quality, primarily: Smoothness, orthogonality, and the aspect ratio [32]. The mesh expansion factor measures the maximum volume change between each neighboring cell. It is effectively a parameter that determines the smoothness of the grid. A mesh expansion factor of 1.2 is usually indicative of a smooth transition between elements. An example of the volume change at the leading edge is shown in Figure 4.3.

Orthogonality is a measure of the angle difference between the vector that joins to two mesh elements centers, and the connecting surface. An ideal orthogonality angle is $90\,\mathrm{deg}$, though sometimes this is written instead as $0\,\mathrm{deg}$ with an increasing angle as detrimental, utilizing the face normal vector as the reference instead of the face itself. The ANSYS CFX solver is capable of handling high aspect ratios, up to 10,000 with the double-precision solver; in any case, the largest aspect ratios should be located where the flow is simple; i.e near the far-field in order to help with convergence.. The determinant is used to check for cells with non-real geometry, such as negative volume.

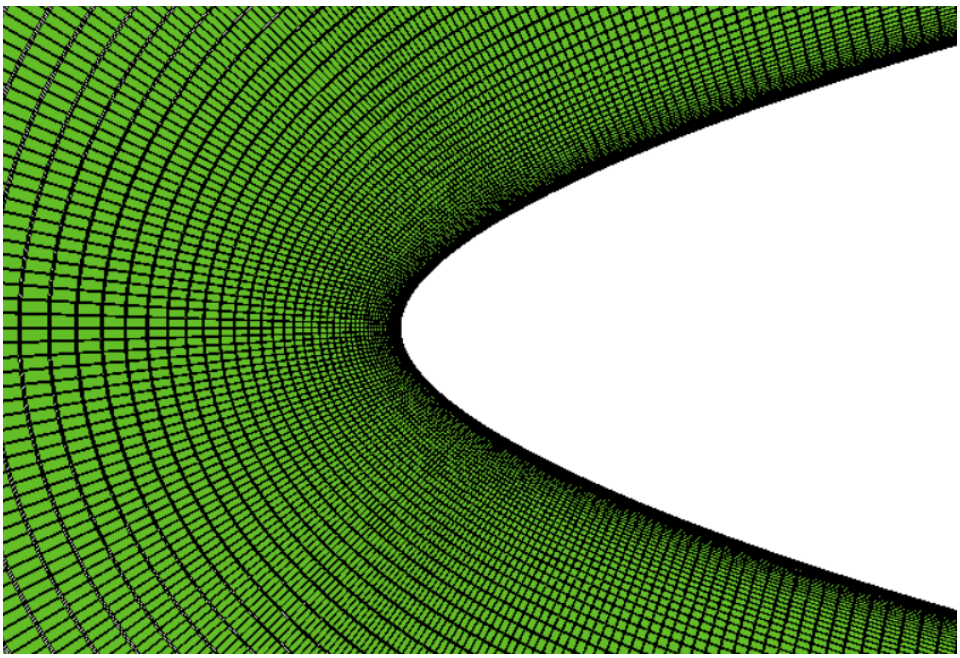

Figure 4.3: Volume change at leading-edge: Cells in green illustrate a mesh expansion factor ≤ 1.2

4.2.2. Element Sizing

The most important criteria for determining the smallest element size is the non-dimensional wall distance, y^+. Typically a y^+ of less than one would be sufficient, however both references utilized lower values, below 1, around y^+ = 0.1 [55, 68]; the y^+ was selected to be as such. The smallest element would, as a result, have a length between 5×10^{-6} & 1×10^{-5} meters.

4.3. Physics Modeling

All the studies that have considered CO_2 and air have indicated that they make no significant difference in the flow behavior or force measurements [5, 56]; this indicates that any simulations can be considered using air, which many studies have done. Though there is the consideration that the atmospheric composition impacts the specific gas constant & the specific heat ratio, which subsequently affects the speed of sound. CO_2 has lower values for both parameters, which would make designing high Mach, low Reynolds number wind tunnels easier, as there would be a lower necessary temperature reduction.

The composition of the Martian atmosphere has been seen to have a limited, and insignificant impact on performance; the difference between the atmospheres is only useful for determining realistic flight conditions on Mars. In order to remove any ambiguity, an ideal gas was assumed with Carbon Dioxide (CO_2) selected as the working gas in order to best match both the numerical results, the experimental results, and more importantly, the Martian environment. Total energy heat transfer and high-speed wall models were activated in order to capture the effects of compressibility.

4.3.1. Boundary & Initial Conditions

The model was set up with pressure boundary conditions at the Inlet, Outlet, and Far-field, as those are ideal for considering compressible flow [68]. The Mach number and Reynolds number were selected for each case, and then every other necessary boundary & initial condition were derived through them, with certain values such as temperature (T), chord length (c), and gas constants (i.e the specific heat ratio, γ) were kept constant; keeping these parameters constant allowed for the Mach number to only be dependent on the velocity, and allowed for a constant dynamic viscosity, μ. The free-stream velocity, U_∞, is then found using just the Mach number (Equation 4.2).

$$U_\infty = M\sqrt{\gamma R_{CO_2} T} \tag{4.2}$$

The standard sea-level temperature for Mars is set as the reference temperature, $T_0 = 214\,\mathrm{K}$, with a reference dynamic viscosity, $\mu_0 = 1.289 \times 10^{-5}\,\mathrm{Pa\,s}$ [55]. With these, Sutherland's law can be used to determine the dynamic viscosity, μ, on Mars at a constant temperature (Equation 4.3) [55]; in this case, the temperature remains $214\,\mathrm{K}$, but the method is also used to determine the dynamic viscosity locally as the temperature varies within the vicinity of the airfoil.

$$\mu = \mu_0 \left(\frac{T}{T_0}\right)^{1.5} \left(\frac{S + T_0}{S + T}\right) \tag{4.3}$$

A constant chord length of c = $0.05\,\mathrm{m}$ was selected, as it was utilized as the chord length by Anyoji et al. [5] and is within a realistic order of magnitude. The boundary-condition for density, ρ, can be found using the Reynolds number (Equation 4.4). The static pressure at the boundaries can then be found using Equation 4.5.

$$\rho = \frac{Re}{cU_\infty{}^2\mu} \tag{4.4}$$

$$P = \rho R_{CO_2} T \tag{4.5}$$

The total temperature and total pressure at the Inlet can be found using Equations 4.6 and 4.7.

$$T_{total} = T\left(1 + \frac{\gamma - 1}{2}M^2\right) \tag{4.6}$$

$$P_{total} = P\left(1 + \frac{\gamma - 1}{2}M^2\right)^{\left(\frac{\gamma}{\gamma-1}\right)} \tag{4.7}$$

Every boundary condition could be applied aside from those related to turbulence; The angle of attack can be utilized in order to receive the necessary directional components of velocity. The static pressure, P, was also subtracted to all pressure values prior to input, and instead specified as the reference pressure. The only remaining boundary & initial conditions to discuss are those related to turbulence.

4.4. Turbulence Model Selection

Yang & Agarwal [68] compared their results to the experimental (MWT) and DNS results found by Munday et al. [39] for both the M_∞ = 0.15 and M_∞ = 0.50 cases, at a Reynolds number of 3×10^3. First, they considered the lift coefficient (Figure 4.4). The results indicate that, when compared to the experimental results, the Spalart-Allmaras turbulence model performed the worst, as it tended to over predict the pre-transition angle lift curve, the SST k-ω model appeared to be fairly good, with a slight deviation, and finally the Wray-Agarwal model, which performed the best when compared to the experimental data.

This is juxtaposed to the work done by Sugar-Gabor & Koreanschi [55], who considered the NACA 0012-34 airfoil instead of the triangular airfoil; Similar to Yang & Agarwal, they consider a Spalart-Allmaras turbulence model, but with one key difference: they utilized a transition model as well, in this case, the one-equation indeterminacy model [55]. The use of a transition model is understandable when comparing the triangular airfoil and the NACA 0012-34 airfoil. The triangular airfoil has a distinct, sharp change in curvature, which essentially makes

predicting transition to turbulence easier due to the predictability of the adverse pressure gradient no matter the Reynolds number. The NACA 0012-34 airfoil has a gradual curvature, and the conditions are at low Reynolds numbers, where modeling transition is essential; thus a transition model to predict when transition occurs is utilized.

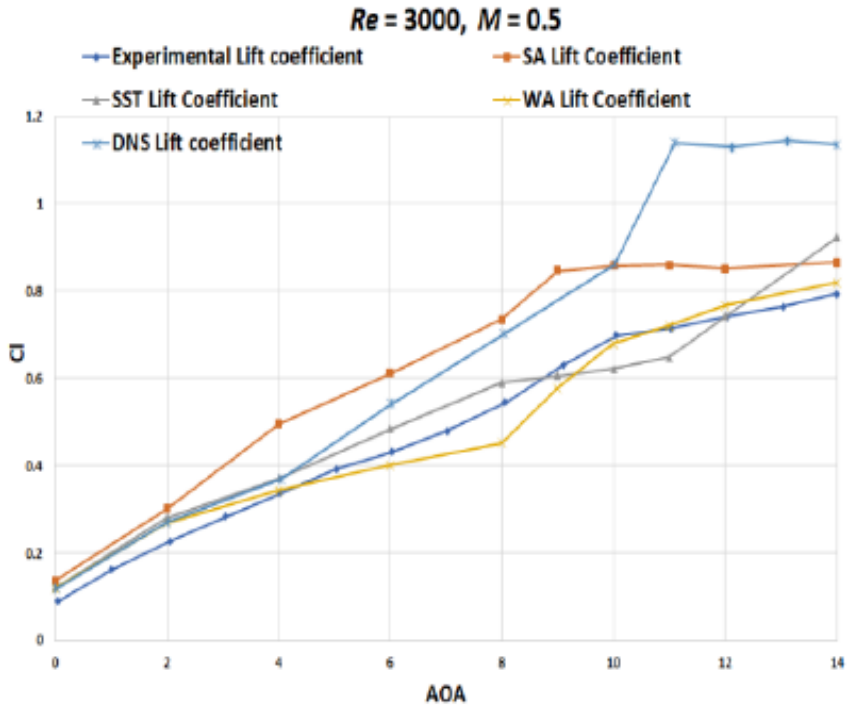

Figure 4.4: Lift coefficient vs. AOA for triangular airfoil using the SA model, Re = 3,000, M_∞ = 0.5 [68]

Numerous turbulence models are of interest when it comes to CFX 19.1 has the Spalart-Allmaras turbulence model as a beta feature, and does not have a transition model implemented; additionally, the Wray-Agarwal turbulence model is unavailable. The k-ω Shear Stress Transport (k-ω SST) turbulence model was seen to perform well and was selected alongside a one equation transition (Intermittency - γ) model. This does increase the number of equations from two to three; though with some gain in accuracy as well.

A certain problem persists with regards to the k-ω Shear Stress Transport turbulence model; the model has an issue with an overproduction of turbulent kinetic energy in regions with an adverse pressure gradient or high curvature [36], which in turn impacts separation prediction greatly. In order to solve this problem, a production limiter was introduced. The original formulation by Menter [35] is presented as a Clip Factor in ANSYS CFX. Kato & Launder [37] presented another production limiter, in order to combat a similar problem; their model is specified as the Kato-Launder production limiter. These two models are both present in ANSYS CFX, and ANSYS recommends the Kato-Launder formulation. While validation will be discussed further in Section 4.7, the process led to a discovery that the Clip-Factor formulation performs significantly better at high angles of attack, as the Kato-Launder formulation still led to an overproduction of turbulent kinetic energy at the leading edge.

4.4.1. Turbulent Conditions

Menter [35] recommends the following boundary conditions for turbulence.

$$\frac{U_\infty}{L} < \omega_{\text{farfield}} < 10\frac{U_\infty}{L} \tag{4.8}$$

$$\frac{10^{-5}U_\infty^2}{Re_L} < k_{\text{farfield}} < \frac{0.1U_\infty^2}{Re_L} \tag{4.9}$$

Where L is suggested to be the approximate length of the computational domain, though this open to interpretation [46]; in general, this should lead to far-field eddy viscosity ratios of $\frac{\mu_t}{\mu}$ = 10^{-5} to 10^{-2}. A common selection for the eddy viscosity ratio is $\frac{\mu_t}{\mu}$ = 0.009 to 0.01 [53].

The conditions on Mars would result in low Reynolds numbers; As previously discussed in this paper, low Reynolds numbers, and high Mach numbers have a stabilizing effect on the boundary layer. The conditions would thus be almost entirely laminar. Sugar-Gabor & Koreanschi [55] corroborate this by utilizing a turbulence intensity of, I = 0.05% for their simulations; assuming the standard validation case (discussed in Section 4.7), then this would fall within the range for turbulent kinetic energy, k, based on Equation 4.10.

$$k = \frac{3}{2}(UI)^2 \tag{4.10}$$

The turbulence conditions were thus taken as a constant turbulent intensity of 0.05% [55], and an eddy viscosity ratio of 0.009 [53]. The initial conditions were set up with each case's test condition, and then a steady-state simulation was run, which in turn would be used as the initial condition for the transient simulation.

4.5. Convergence Criteria

There are two definitions of convergence when it comes to a transient numerical solver, as CFX 19.2 utilizes a number of inner-loop steps to determine the solution for each time-step; usually, this is defined by the residual, where the root mean square (RMS) of each of Navier-Stokes and model equations are run through some number of steps before they reach a residual of 1×10^{-4} to 1×10^{-6}; the lower the residual the more numerically accurate the solution. The maximum value of each residual in the entire domain can also be used as a criterion instead for certain problems. In general, it is a compromise between time (number of inner-loop steps) and numerical accuracy. The second definition is determined when the entire transient solution across some number of time-steps is considered converged; usually by selecting some parameter of interest, and running the simulation until the value hits some asymptotic value. In the case of low Reynolds numbers, this is instead when the mean value of the shed vortex is constant across a certain number of periods: in this case around 100 cycles. An example of asymptotic convergence is shown in Figure 4.5.

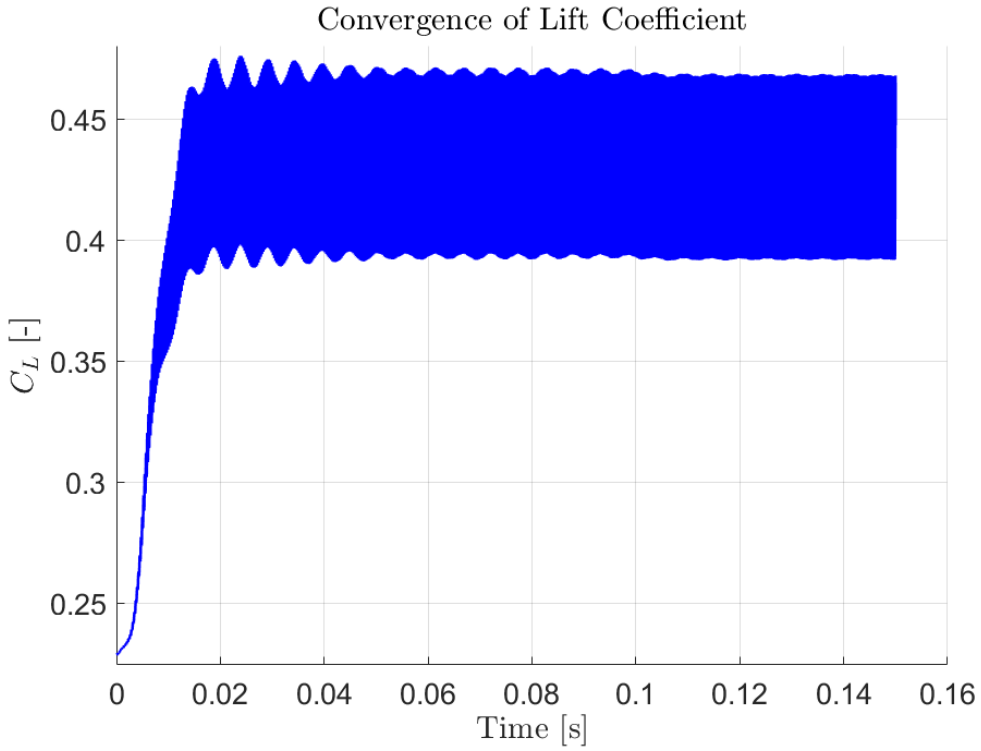

Figure 4.5: Example: convergence of the lift coefficient for the validation case M = 0.61 & Re = 1.1×10^4 at α = 8 deg

4.6. Methodological Limitations

The methodology developed here is pragmatic in its approach to be efficient with the resources available. Unsteady Reynolds-averaged Navier-Stokes models compute the mean flow and are incapable of resolving any turbulent scales; all turbulence is modeled. URANS models have trouble with the separation of buff bodies, and with turbulence within a separated laminar shear layer [25].

The complete modeling of turbulence and transition prevents a thorough stability analysis; a URANS approach is limited when it comes to weak instabilities [16]. URANS is additionally limited when it comes to tackling large-scale coherent structures, and in terms of predicting transition [16]; though the addition of transition models does help, these models are in part based on empirical relations. The two-dimensional approach utilized also introduced margin for potential deviations from reality, as discussed in Section 2.2.1 on the discrepancy between the DNS, URANS, and experimental results. Certain flow phenomena, such as dynamic stall are three-dimensional in nature, and thus a two-dimensional model can fail in capturing it accurately [54, 63]. The upside to a two-dimensional approach is the efficiency of the problem, as a three-dimensional approach would mandate an order of magnitude increase in the cell count.

Aside from the deficiencies of URANS; there are modeling limitations when it comes to specific turbulence models; the k-ω SST turbulence model has issues with predicting separation due

to an overproduction of turbulent kinetic energy at regions of high curvature [35]. These issues can and have been mitigated by the introduction of production limiters. Due to the mentioned examples and other sacrifices in accuracy, all information extracted from this methodology should be compared in relative terms, and not in terms of its exact value; an example would the location of separation, or the shock-wave.

4.7. Verification & Validation

This section will discuss the ability of the method to capture a reasonably accurate representation of what occurs in the researched flight conditions. The experimental and numerical results [5, 55] at M = 0.61, and Re = 1.1×10^4 will be utilized for validation.

4.7.1. Grid-Independence Study

A grid independence study was conducted using three levels of mesh refinement: [74,796; 149,592; 299,184]. The grid spacing, h_i, decreases by a factor of r = 2 for each refinement level. The study was conducted at an angle of attack, α = $8\,\mathrm{deg}$, a Mach number of M = 0.61, and a Reynolds number of Re = 1.1×10^4. As can be seen, the difference between the results of the medium grid and the fine grid are insignificant for the loss in computational efficiency, and as such, the medium grid is selected.

Grid Type	Lift Coefficient [-]	Drag Coefficient [-]
Coarse (74,796 cells)	0.3981	0.1006
Medium (149,592 cells)	0.4218	0.1052
Fine (299,184 cells)	0.4232	0.1054
Experimental Reference [5]	0.3938	0.1032
Numerical Reference [55]	0.4004	0.0956

4.7.2. Time-step Independence

Yang & Agarwal [68] utilized a 2-D URANS approach to analyze the accuracy of various turbulence models at low Reynolds subsonic conditions; a triangular airfoil was utilized with a chord length of 0.03 meters. They determined a time-step of Δt = $1 \times 10^{-5}\,\mathrm{s}$ was viable to capture the unsteady flow behavior within their problem. The dominant unsteady behavior for the flow regimes discussed in this paper is due to vortex shedding in the wake, where a Strouhal number of S_t = 0.21 is to be expected [23]. Using the validation case of M = 0.61, Re = 11,000, a free-stream velocity of U_∞ = $139.282\,\mathrm{m\,s^{-1}}$ is found. The chord length, c, is $0.05\,\mathrm{m}$, at an angle of attack of $8\,\mathrm{deg}$. The frequency of the vortex shedding is determined to be 4,203 Hz, equating to t = $2.4 \times 10^{-4}\,\mathrm{s}$. The selected time-step should be able to capture this frequency, thus should be at least one order of magnitude smaller, placing it around Δt = $1 \times 10^{-5}\,\mathrm{s}$. Lower time-steps ($\Delta t$ = $2.5 \times 10^{-6}\,\mathrm{s}$) do not present a significant increase in accuracy that would require increased computational time.

Time-Step	Lift Coefficient [-]	Drag Coefficient [-]
1×10^{-5} s	0.4218	0.1052
2.5×10^{-6} s	0.4384	0.1074

4.7.3. Solution Verification

A generalized Richardson extrapolation procedure was used to determine the accuracy of the solution: as the exact solution is unknown and unknowable with regards to verifying the numerical model, then three numerical solutions are necessary in order to calculate the observed order of accuracy [45]. The three grids were generated with a refinement factor of r = 2, where the spacing of the fine grid is half that of the medium grid, which is half that of the coarse grid.

$$r = \frac{h_2}{h_1} = \frac{h_3}{h_2} = 2 \tag{4.11}$$

The solutions, f_i, are found for each of the three grids, and are numbered based on their refinement: the solution of the fine grid, f_1, the medium grid, f_2, and the coarse grid, f_3. The solutions of the three grids are then used to calculate the observed order of accuracy, p, for that specific parameter (Equation 4.12).

$$p = \frac{\ln\left(\frac{f_3 - f_2}{f_2 - f_1}\right)}{\ln(r)} \tag{4.12}$$

The parameters in question are the velocity, temperature, and density, measured within the wake; this is done specifically for the validation case of M = 0.61, Re = 1.1×10^4. The observed order of accuracy is seen to be approximately $p \approx 2.3$ for the three parameters considered. The schemes used are either second-order, or the aforementioned high-resolution scheme; this indicates that the numerical method is reliable, as the observed order of accuracy is near the formal order of accuracy.

4.7.4. Validation Study

The experimental results provided by Anyoji et al. 2015 [5], and numerical results Sugar-Gabor & Koreanschi [55] were used in conjunction to help validate the model. Simulations were conducted at M = 0.61, and Re = 1.1×10^4 throughout a full angle of attack range. An unsteady simulation is only considered for angles of attack above $5\,\mathrm{deg}$, as the impact of unsteady behavior diminishes as the angle of attack drops [39, 55, 68]. As can be seen in Figures 4.6 and 4.7, the lift and lift-drag polars are consistent with the experimental and numerical data. Issues arose with stall angles of attack due to the over-production of turbulent kinetic energy at the leading edge; this was mitigated by selecting the clip-factor instead of the recommended Kato-Launder production limiter.

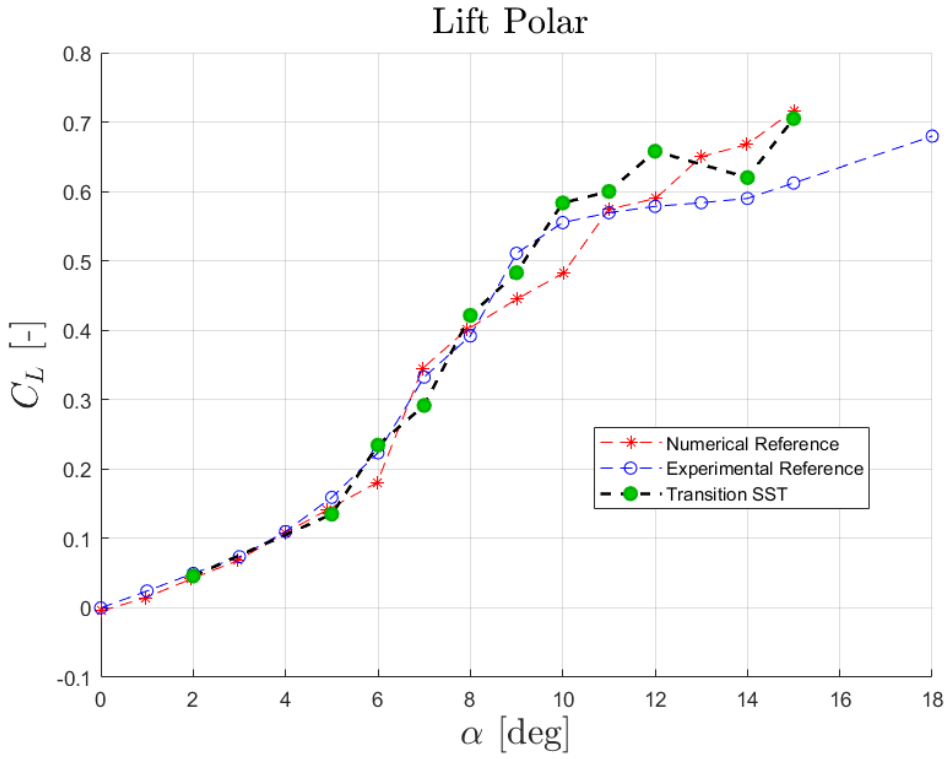

Figure 4.6: Lift Polar for the experimental reference [5], the numerical reference [55], and the model results (Transition SST)

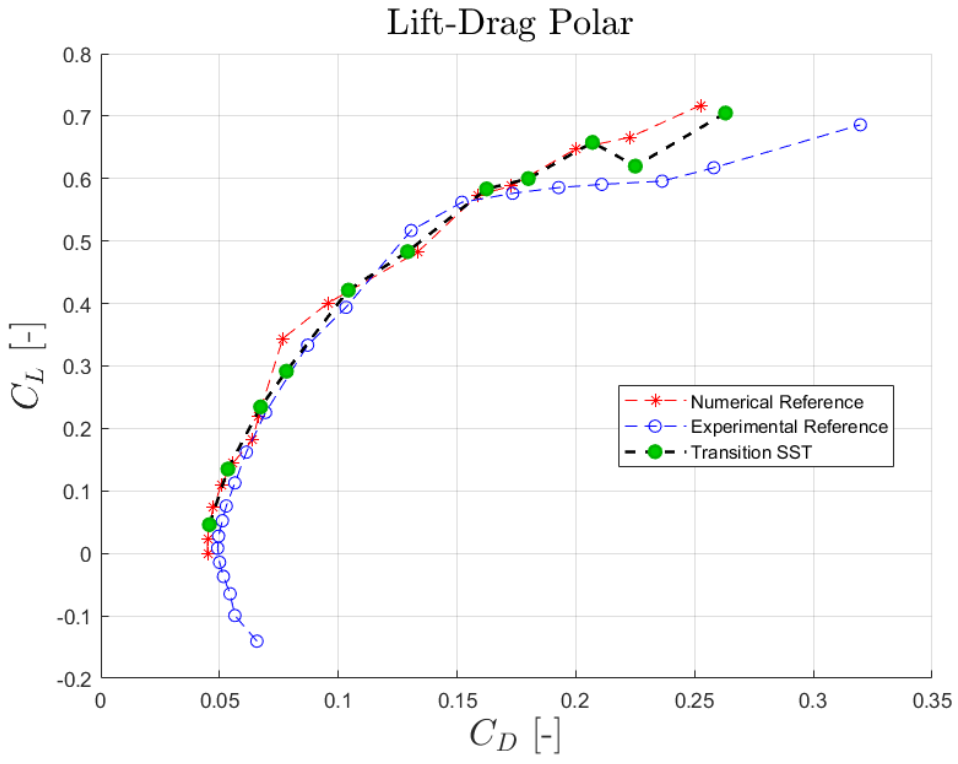

Figure 4.7: Lift-Drag Polar for the experimental reference [5], the numerical reference [55], and the model results (Transition SST)

„ 5 Results & Discussion

5.1. Mach Number Effects

Figure 5.1 presents the onset of drag divergence at a constant angle of attack, α = $8\,\mathrm{deg}$, and at a constant Reynolds number, Re = 1.1×10^4. Here it can be seen that the drag coefficient grows substantially after a certain Mach number is achieved (M = 0.75). At this Mach number, it can be seen that dC_d/dM = 0.10, and thus is the drag divergence Mach number for α = $8\,\mathrm{deg}$. The behavior is consistent with what is seen for higher Reynolds numbers, albeit with a substantially larger drag coefficient.

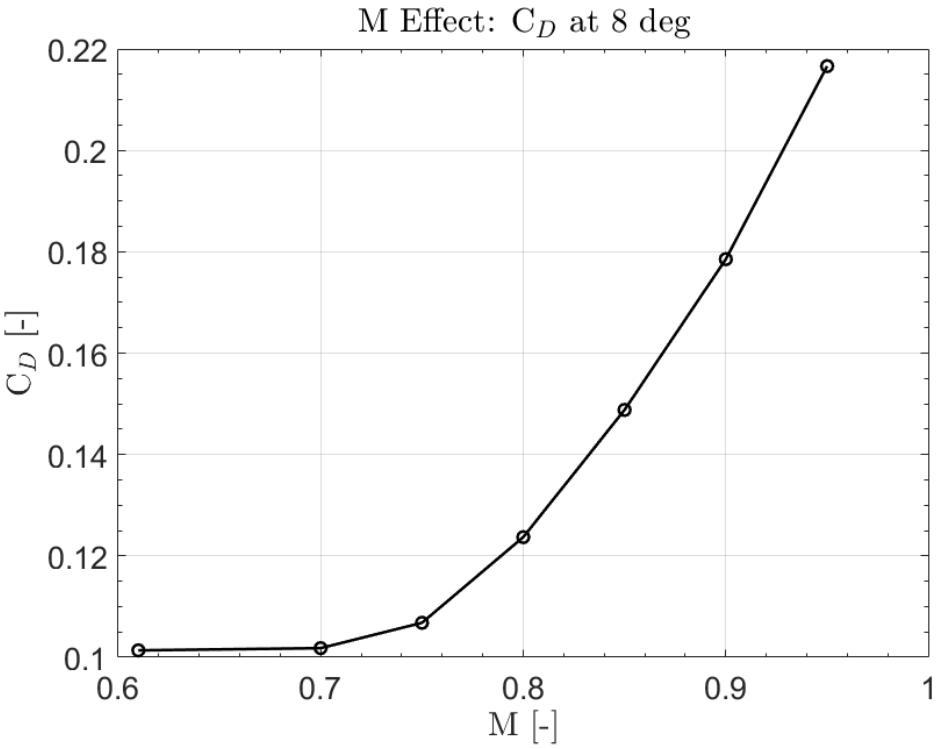

Figure 5.1: Mach number effect on the Drag Coefficient for a NACA 0012-34 Airfoil: Re = 11,000, α = $8\,\mathrm{deg}$

In contrast, the lift coefficient illustrates a different scenario from what is typically seen. For standard flight conditions on Earth, the lift coefficient grows with increasing Mach number due to compressibility effects, and then drops as shock-waves are introduced; this was illustrated in Figure 2.13 in Section 2.2. This is juxtaposed to what is seen in Figure 5.2; as predicted, the lift coefficient decreases as M increases to higher subsonic values. This trend appears to reverse as the drag divergence Mach number is surpassed, contrary to what is seen at conventional Reynolds numbers, where a shock-wave has a negative impact on the lift coefficient.

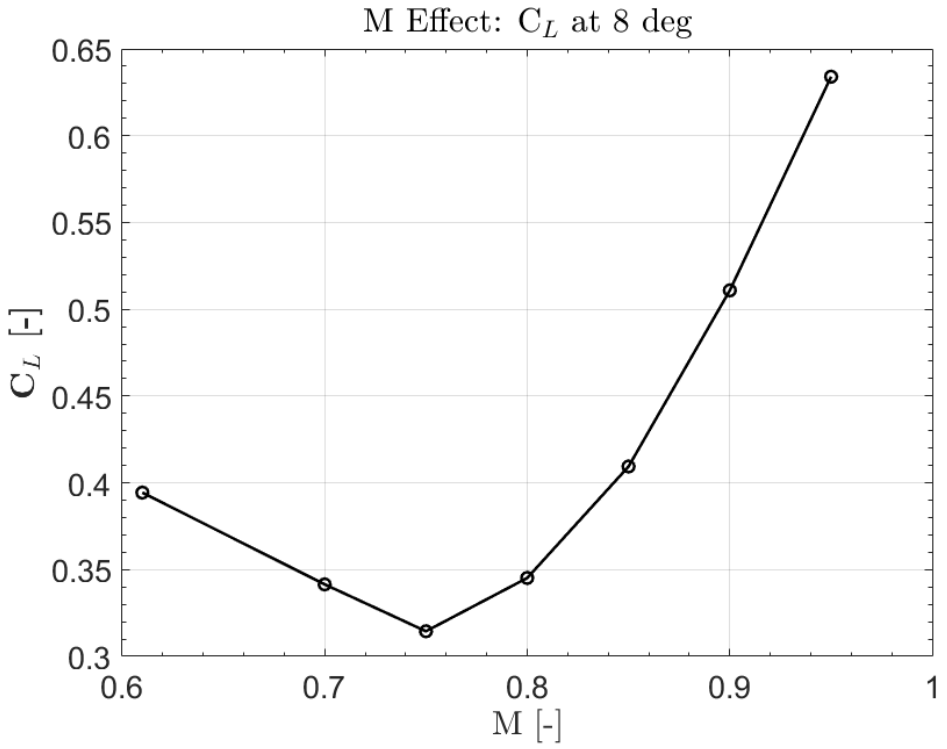

Figure 5.2: Mach number effect on the Lift Coefficient for a NACA 0012-34 Airfoil: Re = 11,000, α = 8 deg

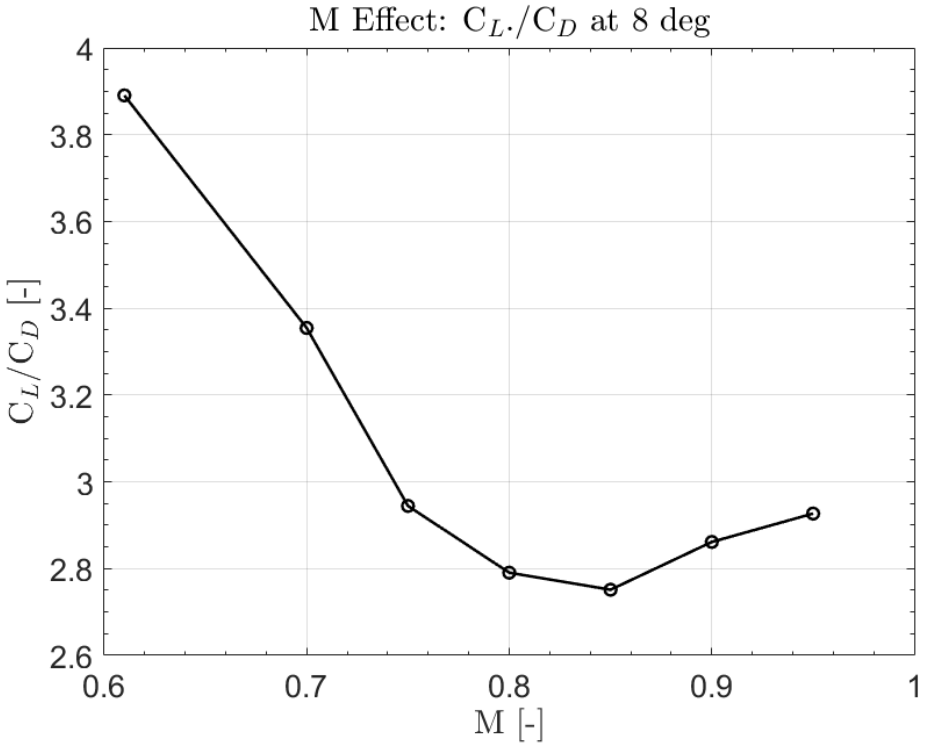

Figure 5.3: Mach number effect on the Lift-to-Drag ratio for a NACA 0012-34 Airfoil : Re = 11,000, α = 8 deg

5.1.1. Transonic Effects & SBLI

Figure 5.3 presents the onset of transonic flight and its subsequent impact on the lift-to-drag ratio; as can be seen, the increase in lift coefficient after the critical and drag divergence Mach numbers are surpassed is initially accompanied by a decrease in the descent of the lift-to-drag ratio, up until it reverses, albeit slightly, around M = 0.85. In order to understand why this occurs, let us consider the pressure distributions (Figure 5.4). A general estimate for the location of the shock-wave at some of the considered Mach numbers can be extracted from the pressure distributions of each condition; an exact location is difficult to ascertain due to the smearing of the shock. Prior to the drag divergence Mach number (M = 0.75), the suction peak, $C_{P,min}$, occurs at or near the leading edge. The suppressed magnitude of $C_{P,min}$ due to compressibility effects can be seen to continue, up until M passes the inflection point of the lift-to-drag curve (M = 0.85), then the following trends can be seen: the aft movement of $C_{P,min}$; a mild increase in the magnitude of $C_{P,min}$, and a less adverse pressure gradient.

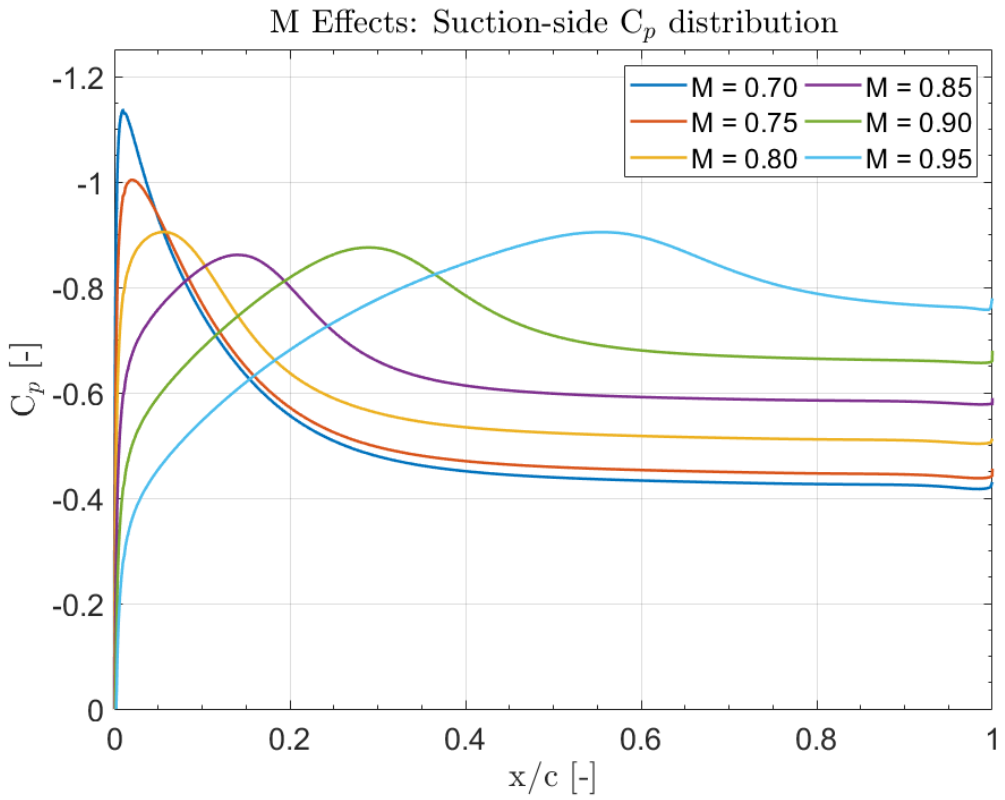

Figure 5.4: Mach number effect on NACA 0012-34 Pressure distributions at $Re = 1.1 \times 10^4$ & $\alpha = 8\,\mathrm{deg}$

Once the critical Mach number is surpassed, the suction peak begins to move aft as a result of an expansion fan forming at the regions of diverging curvature; this movement is illustrated in Figure 5.8. The magnitude of $C_{P,min}$ initially decreases, following the same trend seen in the literature, at which M has a detrimental impact on $C_{P,min}$ (Chapter 2.1.2). The reduction in the magnitude of $C_{P,min}$ was stated to be due to the interaction between viscous and com-

pressibility effects, which result in the in-applicability of Prandtl-Glauert corrections above M = 0.3 for low Reynolds numbers. As M increases, the resulting temperature rise can result in an increase in μ; this, in turn, can impact C_f, the boundary-layer thickness, displacement thickness, and momentum thickness. As discussed, these are important parameters in defining the external velocity as described in the Von Kármán relation.

The adverse pressure gradient for the high subsonic cases is steeper than the transonic cases and is a result of the already depressed suction peak due to subsonic Mach effects, and the diminished interaction between the shock-wave and the boundary-layer at lower Reynolds numbers, as discussed in Chapter 2.4.1. Why this is the case can be seen by considering the Mach numbers at which a shock occurs, and comparing it to their respective pressure distributions. While the drag divergence Mach number occurs around M = 0.75; the first formations of a shock are not seen until M = 0.80 (Figure 5.6). It is not until M = 0.85, at the aforementioned inflection point in the lift-to-drag curve, that the lambda structure begins to form in a similar fashion to what occurs for a shock-control bump (Chapter 2.4.1). As can be seen in Figure 5.7 for M = 0.85, this lambda structure is significant, and the second leg of the structure forms aft of the trailing edge. At M = 0.90, the lambda structure of the shock increases in size; additionally, the second shock leg moves in line with the normal shock at the point where the two shock legs meet.

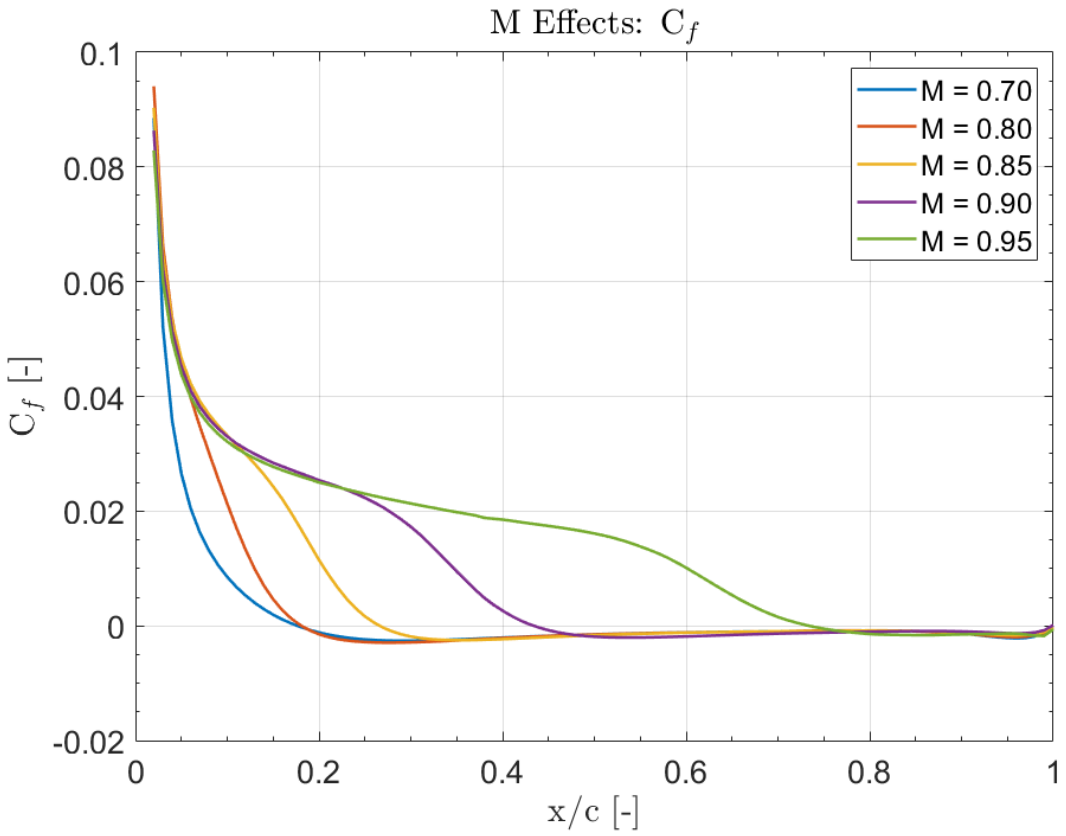

Figure 5.5: Mach number effect on Skin Friction Coefficient: Re = 11,000, & α= 8 deg

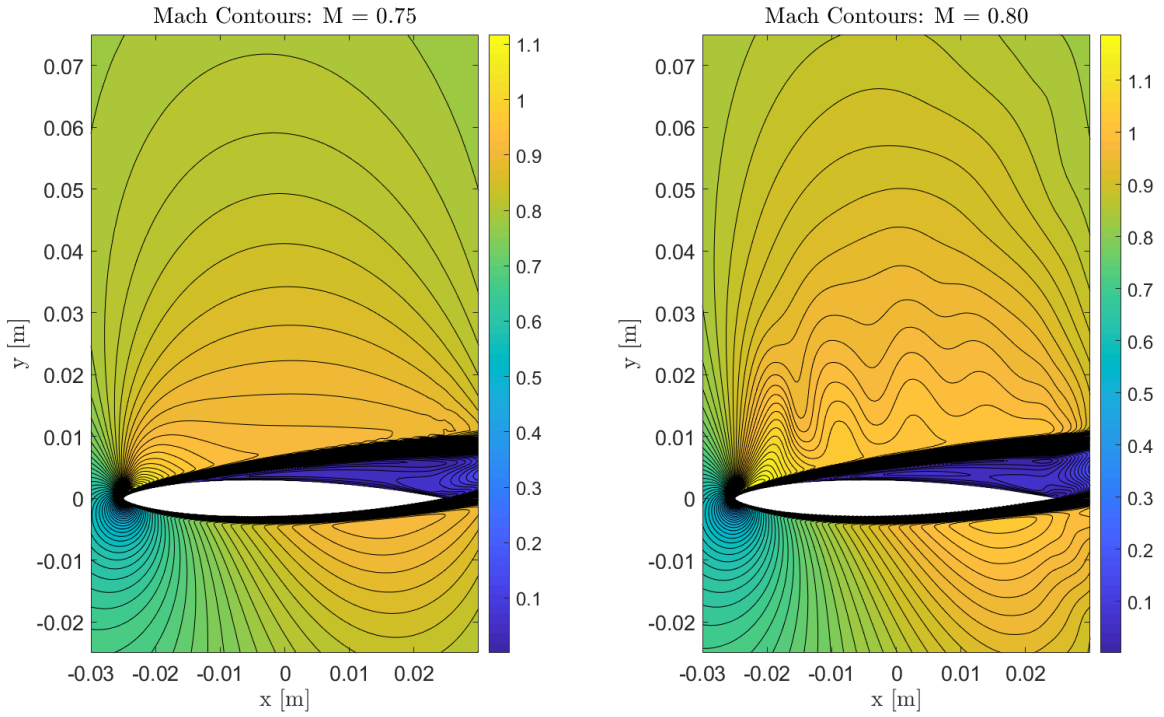

Figure 5.6: Time-averaged Mach contours at M = 0.75 & M = 0.80 at Re = 1.1×10^4 & α= 8 deg

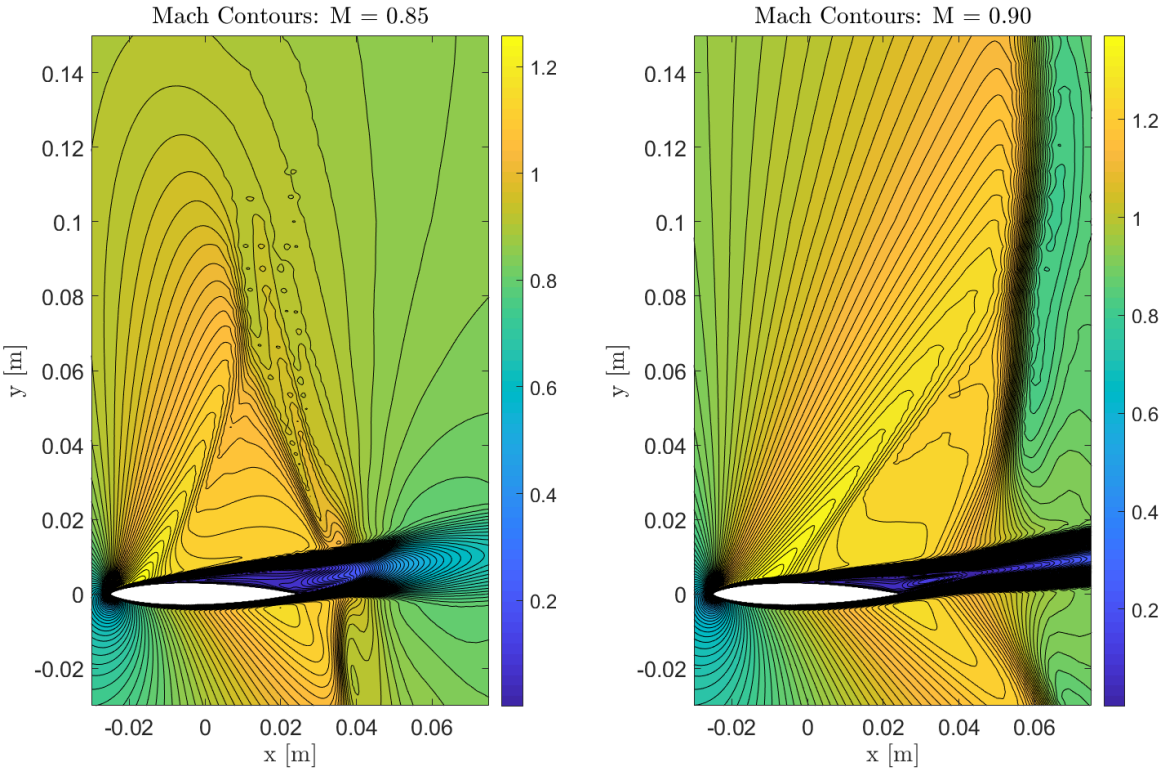

Figure 5.7: Time-averaged Mach contours at M = 0.85 & M = 0.90 at Re = 1.1×10^4 & α= 8 deg

5.1.2. Boundary-layer Separation

As the shock-wave moves aft due to an increase in Mach number, and there exists a favorable pressure gradient prior to the shock-wave; one can expect that the separation point moves aft until after the shock-wave. Figure 5.5 presents a targeted view of the skin friction coefficients, where at which it can be seen that the separation point is consistently aft of the adverse pressure gradients initial point, and moves further aft as M increases (Figure 5.8). This is due to the influence of the pressure gradient on the separation point, where the flow reversal occurs due to the flow within the boundary-layer no longer being able to counteract the increase in pressure. From what can be inferred is that the expansion fan extends the favorable pressure gradient, and the low Reynolds numbers' effect on the shock-wave boundary-layer interaction reduces how adverse the pressure gradient is after the first leg of the shock occurs. This is important in producing higher lift coefficients, as the key reason for the poor lift performance of a NACA 0012-34 airfoil at low Reynolds numbers is that the high stability of the boundary-layer at these conditions delays transition, and thus promotes laminar separation, and inhibits reattachment of the separated shear-layer.

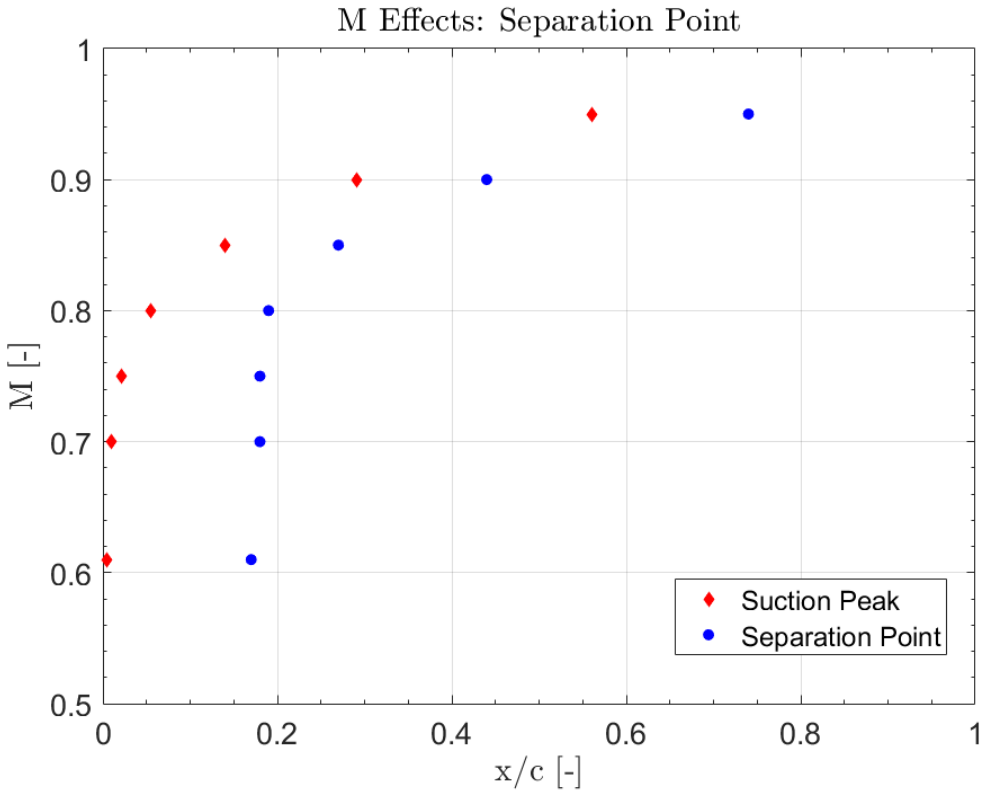

Figure 5.8: Mach number effect on the location of $C_{P,min}$ & separation point for a NACA 0012-34 at Re = 1.1×10^4 & α= 8 deg

Figure 5.9 shows the shape factor at various Mach numbers; the boundary-layer remains laminar up until separation, as the shape factor for each case remains relatively stable up until the pressure gradient becomes adverse. A shape factor of around H = 4 is expected

before the separation of a laminar boundary-layer occurs; Figure 5.10 shows that separation does indeed occur near or above this value. The shape factors found are slightly higher than predicted, with the laminar boundary-layers having shape factors around H = 3.2 rather than the expected H = 2.7; this is likely due to the upper integral limited selected for velocity. In any case, the only impact this has is on the scaling of the shape factors value.

5.1.3. Boundary- & Shear-layer Stability

The stability of the boundary-layer is also seen to be impacted, or rather more specifically, the relative location of the transition point. After the separation point, the shape factor still increases monotonically up until an inflection point occurs; for M = 0.61; this occurs within the bounds of the airfoil-chord around x/c = 0.88. The drop in shape factor here is indicative of the transition of the separated shear-layer, and occurs in a similar fashion to what is described in Figure 2.5. In fact, for the all the cases above M = 0.61 at $Re = 1.1 \times 10^4$, the boundary-layer does not appear to transition; this is reasonable, as Anyoji et al. [5] found for M = 0.61, Re = 1.1×10^4 that the transition point does not occur until x/c = 0.9, which fairly consistent with the decrease in the shape factor for the same case seen in Figure 5.9.

The transition point at these conditions is primarily dominated by the pressure gradient; as free-stream turbulence is small, there is no considered the surface roughness, and the airfoil surface is specified as an adiabatic wall. In this case, it can be said that the transition point is pushed aft due to the expansion fan moving the adverse pressure gradient aft and the subsequent shock decreasing the severity of said adverse pressure gradient. This was predicted in the formulation of the research in Chapter 3; where increased attached laminar flow is expected due to the aft movement of the adverse pressure gradient.

A question remained whether the advent of the shock-wave would provide significant enough of an adverse pressure gradient to have a destabilizing effect on the boundary-layer enough to encourage earlier transition; this does appear not to be the case. The interaction of the shock wave and the boundary-layer at low Reynolds numbers has been seen to be diminished and spread out, resulting in a lower adverse pressure gradient and an overall smaller change in the pressure coefficient compared to the sub-transonic cases (M = 0.70); this itself would be indicative of a delay in transition by itself, under the assumption that the adverse pressure gradient is the dominant factor for instability at these conditions. On top of the aforementioned effects, one must also consider the aft movement of the adverse pressure gradient due to the expansion fan. which would delay the transition point by itself, even if the pressure gradient were not to change. This is an addition to the increasing suppressed suction peak magnitude due to increasing sub-transonic Mach numbers at low Reynolds numbers discussed in Chapter 2.1.2.

The transition point is delayed due to increasing Mach numbers due to three key reasons: the decrease in the magnitude of the suction peak, $C_{P,min}$, due to compressibility effects at low Reynolds numbers, the decrease in the severity of the adverse pressure gradient due to a

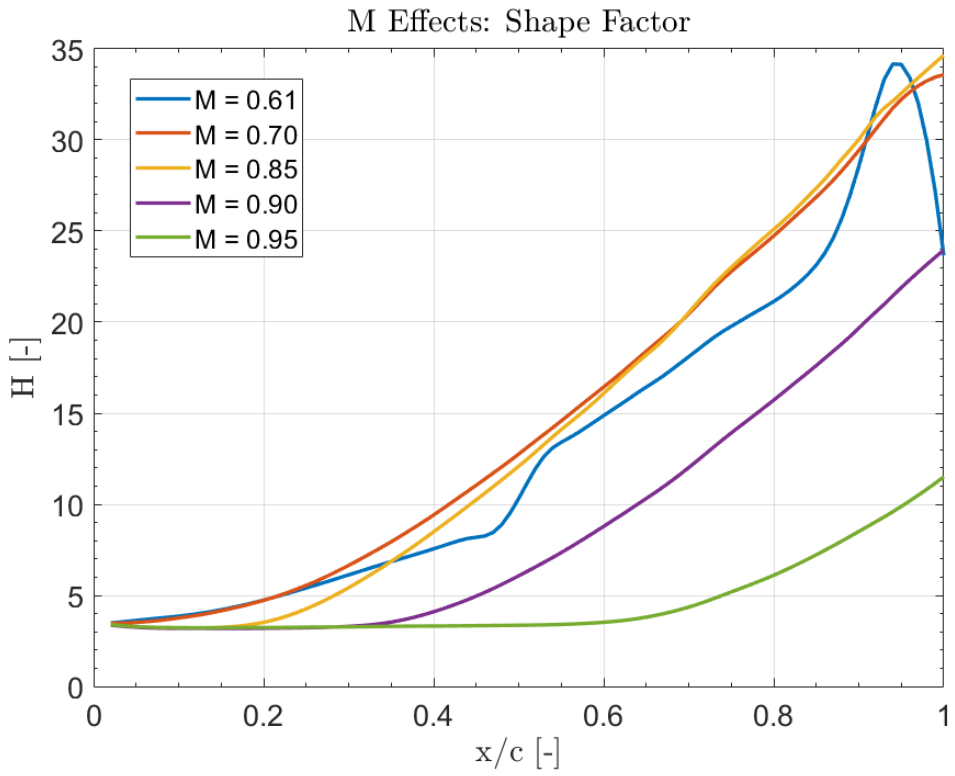

Figure 5.9: Mach number effect on the shape factor, H: Re = 11,000, & α= 8 deg

shock wave at low Reynolds numbers, and the aft movement of the shock-wave, and subsequent adverse pressure gradient, due to the expansion fan. This culminates into a scenario where the transition point being pushed further aft where no transition of the boundary-layer within the bounds of the airfoil chord length; this can be seen for M = 0.61 for a Reynolds number of Re = 1.1×10^4, as seen in Figure 5.9, where the transition point is near the trailing edge. For the considered Reynolds number of Re = 1.1×10^4, the transition point moves aft of the trailing edge solely due to the sub-transonic compressibility effects and can be seen in the in shape factor for M = 0.70 (Figure 5.10), where transition no longer occurs.

The effect this has on the vortex shedding can be seen in Figure 5.12; the aft movement of the transition point coincides with a reduction in the Strouhal number. This is similar to the compressibility effects on the Strouhal number discussed in Chapter 2.2. The amplitude of the vortex shedding and its effect on the lift coefficient shown in Figure 5.12indicates that there is a significant drop-off in influence the shed vortex has on the force coefficients after M = 0.61, which reasons that this is due to the transition point moving aft of the trailing edge as it is the later stages of transition that result in the development of coherent structures that can contribute to vortex shedding. The separated shear-layer is an additional factor to consider; the Kelvin-Helmholtz instability develops within the separated shear layer. The separation point moves aft and thus the size of the separated shear layer is impacted. Additionally, The Kelvin-Helmholtz instability within the separated shear-layer is impacted by the compressibility of the

second leg of the shock, as the Mach numbers on the boundary of the wake are above unity near the trailing edge. The Kelvin-Helmholtz instability has been seen to be impacted quite significantly due to increased compressibility, resulting in a stabilizing effect. As M increases, an aft movement of the second shock leg occurs, and thus the wake experiences more of this phenomena, and thus would in help suppress the development of these roll-up vortices. This indicates that the cases become more steady at higher Mach numbers; at M = 0.90 and above, no oscillation of the force measurements occurs. The lack of any force oscillations also indicates that the shock-wave does not move in time. This can be confirmed to be true by considering a time-instantaneous plot to see if any vortex shedding does occur, as can be seen in Figure 5.11. There is a significant caveat with regards to these conclusions; the mesh could be too coarse to capture the developing vortex significantly aft of the trailing edge, and the URANS approach used could prevent small-scale fluctuations from being captured. In any case, these would likely be small, but would require further research.

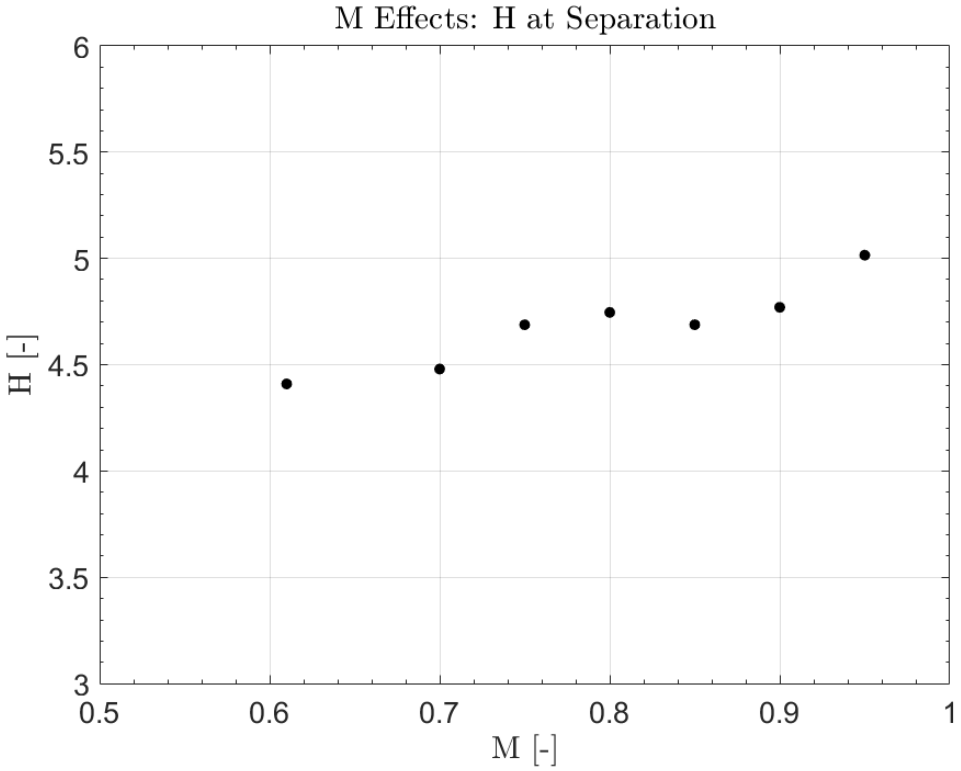

Figure 5.10: Mach number effect on the shape factor, H, at separation: Re = 11,000, & α= $8\,\mathrm{deg}$

The above reasons for why transition is delayed explain why the lift coefficient increases at post-critical Mach numbers relative to the subsonic cases; it can be concluded to be a result of the expansion fan moving $C_{P,min}$ aft, and the diminished and spread out the interaction between the shock-wave and the boundary-layer, which allows the boundary-layer to retain its momentum due to the lower adverse pressure gradient, and thus delays separation of the laminar boundary-layer. The shock wave boundary-layer interaction results in drag savings as well, in a similar fashion to a shock control bump.

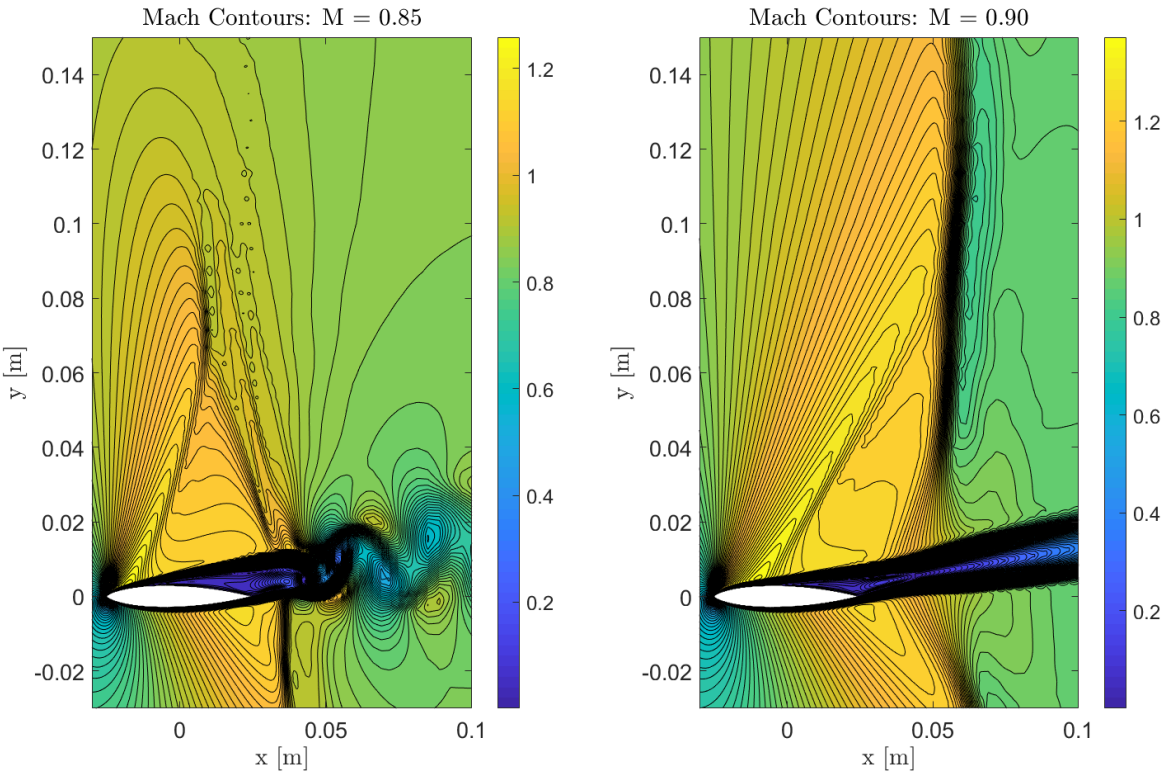

Figure 5.11: Time-instantaneous Mach contours at M = 0.85 & M = 0.90 at Re = 1.1×10^4 & α= 8 deg

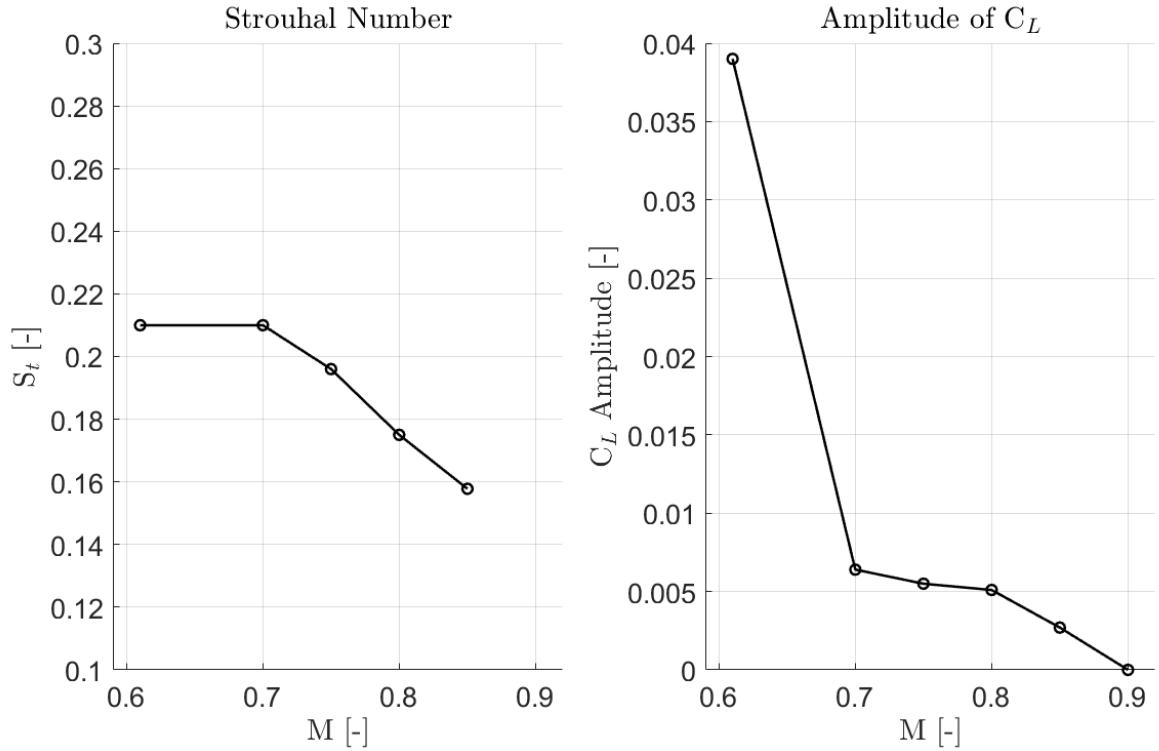

Figure 5.12: Mach number effect on the Strouhal number, S_t & vortex shedding Amplitude: Re = 11,000, & α= 8 deg

5.2. Reynolds Number Effects

Within the bounds of flight on Mars, the Reynolds number would have a few key effects on boundary-layer: the overall shape and profile of the boundary-layer, the stability of the boundary-layer, and the strength of the interaction between the shock wave and the boundary-layer. The pressure distribution is impacted due to the increase in displacement thickness, which in turn alters the effective curvature of the airfoil; this is of primary concern for the leading edge, as the magnitude of the pressure coefficient is suppressed; this impacts lift, but also helps minimize the strength of the adverse pressure gradient. It was also seen that the decrease in Re has had a stabilizing effect on the boundary-layer, specifically in that the transition point is pushed further aft, thus delaying or preventing reattachment. Separation of the laminar boundary-layer is in turn impacted by the strength of the shock-wave boundary-layer interaction and its subsequent effect on the pressure gradient.

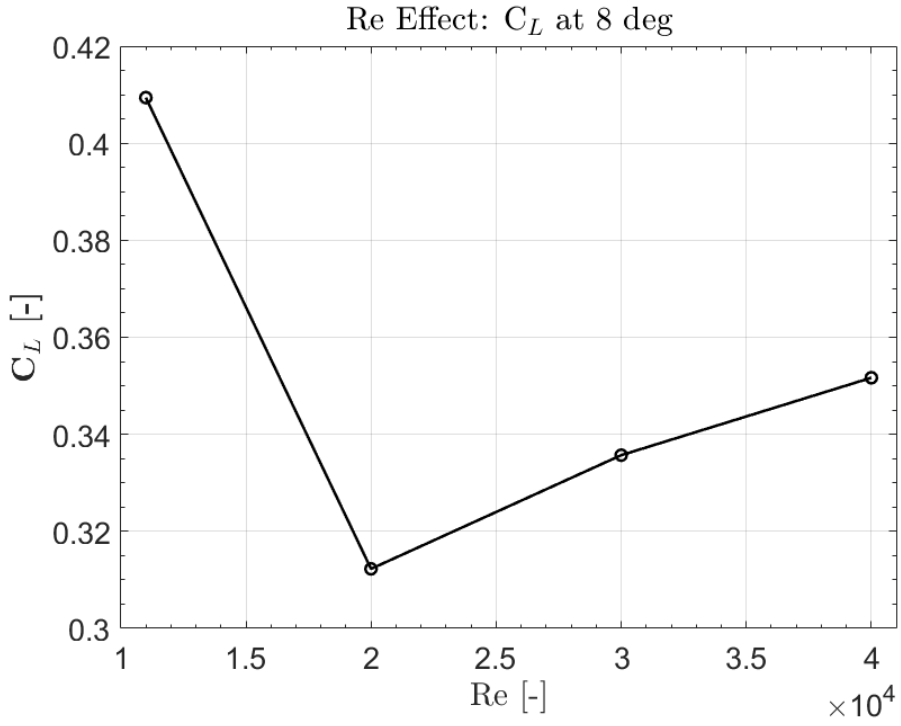

Figure 5.13: Reynolds number effect on the Lift Coefficient for a NACA 0012-34 Airfoil: M = 0.85, α = 8 deg

The key factor for why lift performance is depressed at low Reynolds numbers is due to the early separation of the laminar boundary-layer. At transonic Mach numbers this has been seen to reverse relative to the high subsonic condition at a constant Re. With these facts in mind, one would expect an increase in Re to the following effects: stronger adverse pressure gradient, earlier transition, an increase in the magnitude of $C_{P,min}$. How this impacts the lift and drag coefficients can be seen in Figures 5.13 and 5.14; the increase in Re results in an initial drop in the lift coefficient but then proceeds with a further increase. This coincides with a decrease in drag (Figure 5.14). Aerodynamic performance improves overall as a result (Figure 5.15).

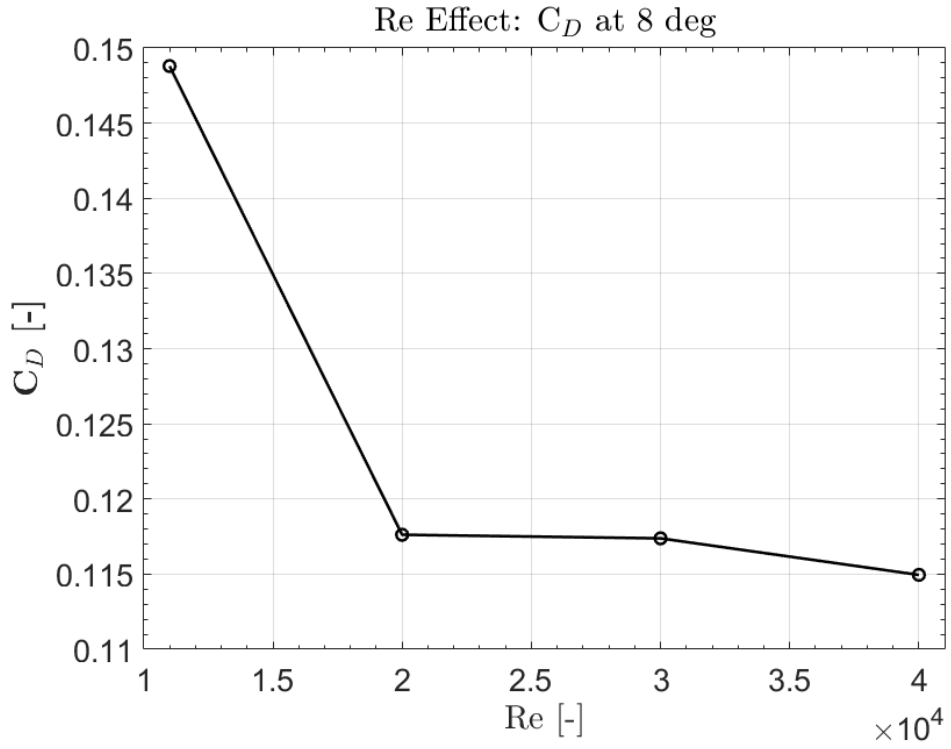

Figure 5.14: Reynolds number effect on the Drag Coefficient for a NACA 0012-34 Airfoil: M = 0.85, α = 8 deg

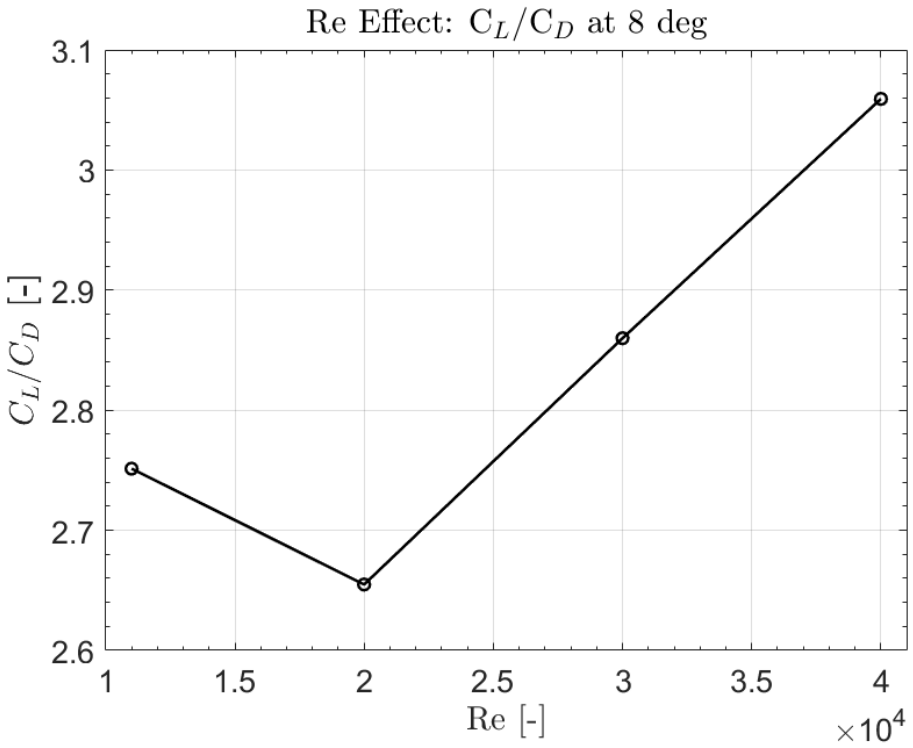

Figure 5.15: Reynolds number effect on the Lift-to-Drag ratio for a NACA 0012-34 Airfoil: M = 0.85, α = 8 deg

5.2.1. Transonic Effects & SBLI

The reasoning for this can be explained by considering the pressure distributions (Figure 5.16). As can be seen, $C_{P,min}$ moves forward along the chord, and reduces in magnitude; this trend appears to reverse once Re increases further. This is a combination of two phenomena: the strength of the shock wave boundary-layer interaction, and the effect of an increase in Re on the boundary-layer profile and thus the pressure distribution, more specifically $C_{P,min}$. The strength of the shock wave boundary-layer interaction strengthens as Re increases, as the boundary layer thickness decreases, and thus the sonic line moves closer to the airfoil; this effectively moves the coalescent point of the compression lines closer to the sonic line, and thus upstream due to the angle of the shock. This also coincides with the breakdown of the

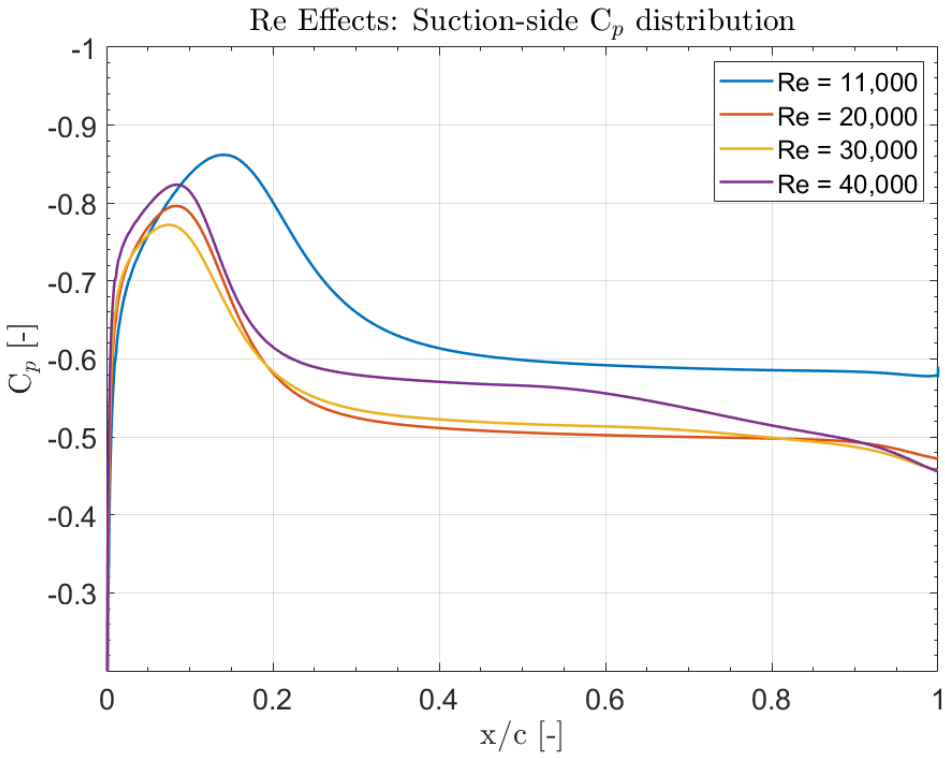

Figure 5.16: Reynolds number effect on NACA 0012-34 Pressure distributions at M = 0.85 & α= 8 deg

lambda structure (Figure 5.18); the shape of the shock at $Re = 2 \times 10^4$ appears to indicate the formation of the lambda structure. The lambda structure is highly dependent on the curvature of the geometry; in this case the sonic line. An increase in Re alters this curvature due to the decrease in displacement thickness, and thus it appears more as a main shock-wave with a secondary shock-wave forming. A similar scenario occurs in The last section on Mach effects that saw that the lambda structure develops after the first signs of a shock appear (M = 0.80); in order to check whether an increase in Re delays this development to higher Mach numbers, cases at M = 0.90 were considered as well in Figure 5.19. There does appear to be some indications of it being the case, but it appears that instead of oblique shock forming at the

front leg, compression waves form instead. In this case, the behavior is still exactly that of a shock control bump; expansion waves still emerge within the lambda shock region. Another point of interest is the gradient of the interaction zone between the second shock leg and the separated shear layer; the lower Reynolds number case illustrates a more gradual decrease in M within; this coincides with a less adverse pressure gradient acting on the wake.

5.2.2. Boundary-layer Separation

A further increase in Re results in a subtle increase in the magnitude of the suction side of the pressure distribution; as mentioned, this is due to the decrease in the displacement thickness and skin friction coefficient. There now exists two opposing trends, a detrimental increase in the strength of the shock wave boundary-layer interaction, and a beneficial impact on the magnitude of the suction-side pressure distribution. The result of this can be seen on the separation point (Figure 5.17). The separation point moves aft, initially quite substantially. A forward movement in the separation point can be seen from $Re = 2 \times 10^4$ and above, but it is rather small, and is due to the steeper adverse pressure gradient due to the stronger shock interaction. The drag coefficient is in turn impacted by all these factors as well. An increase in Re would result in the stronger shock-wave boundary-layer interaction, which could increase pressure drag, but it appears that the drop in viscous drag precludes an overall increase in drag and outpaces the drag increase due to the strengthened shock-wave boundary-layer interaction beyond $Re = 3 \times 10^4$ (Figure 5.20).

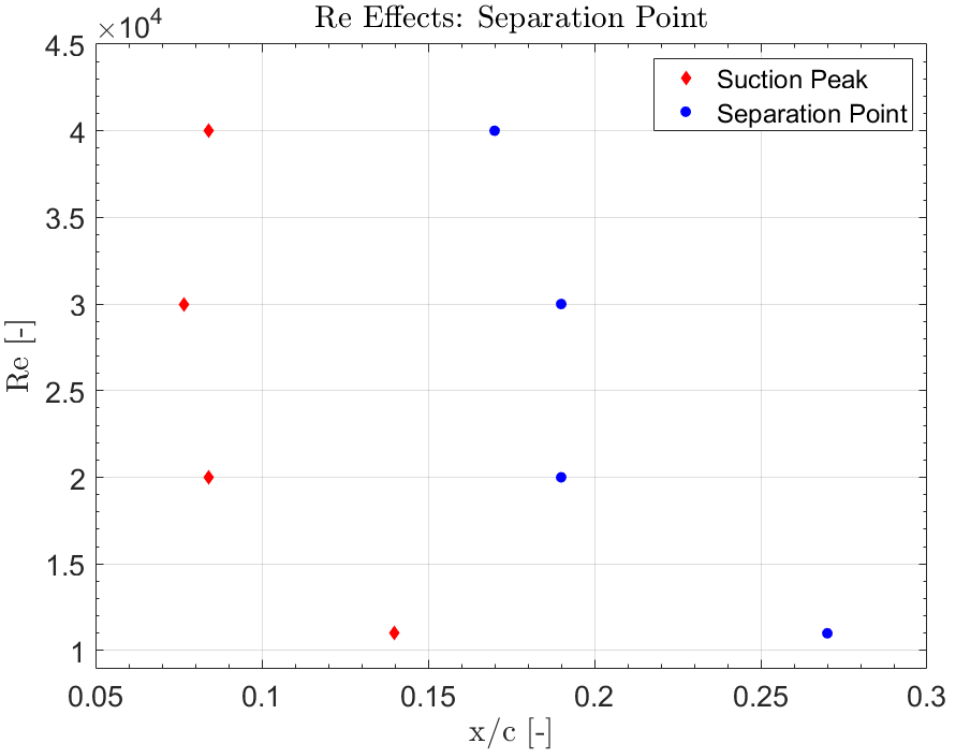

Figure 5.17: Reynolds number effect on $C_{P,min}$ and separation point, H, at separation: M = 0.85, & α= 8 deg

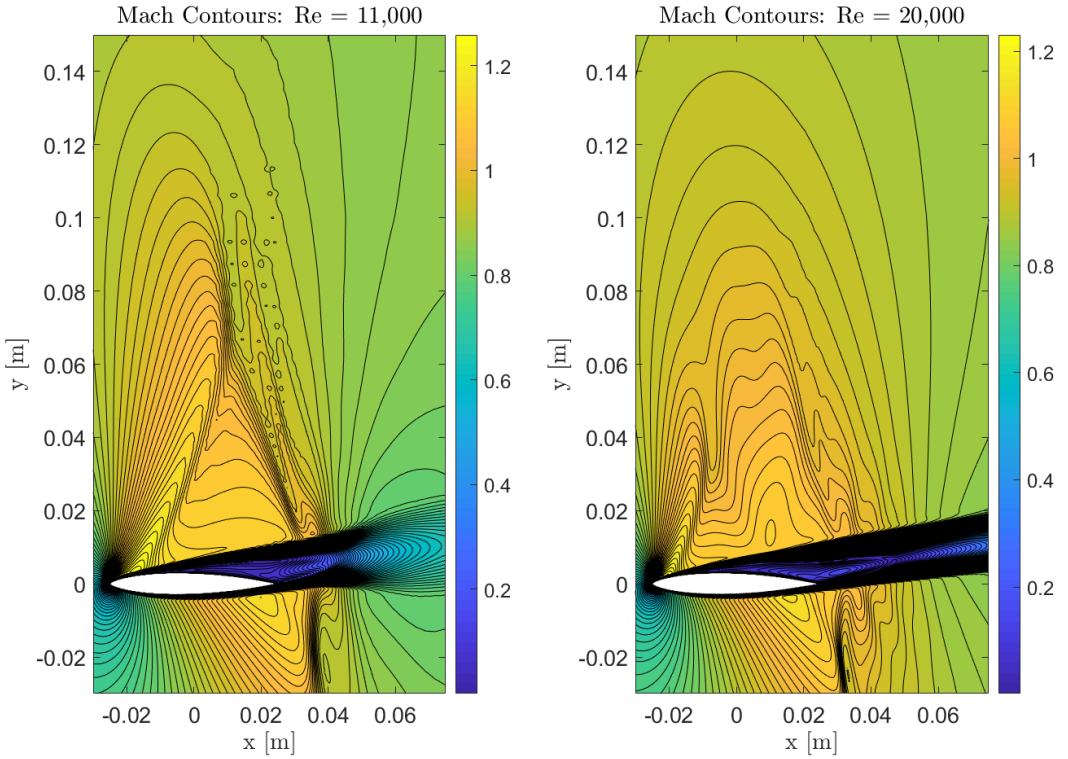

Figure 5.18: Time-averaged Mach contours at Re = 1.1×10^4 & Re = 2×10^4 at M = 0.85 & α= 8 deg

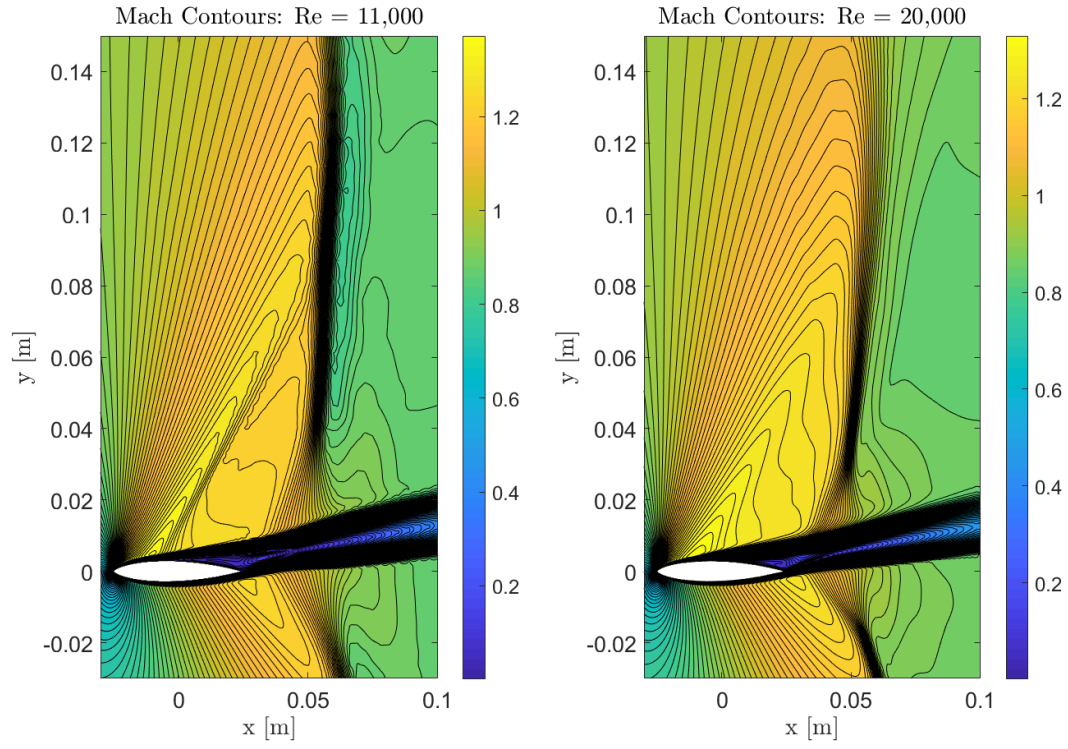

Figure 5.19: Time-averaged Mach contours at Re = 1.1×10^4 & Re = 2×10^4 at M = 0.90 & α= 8 deg

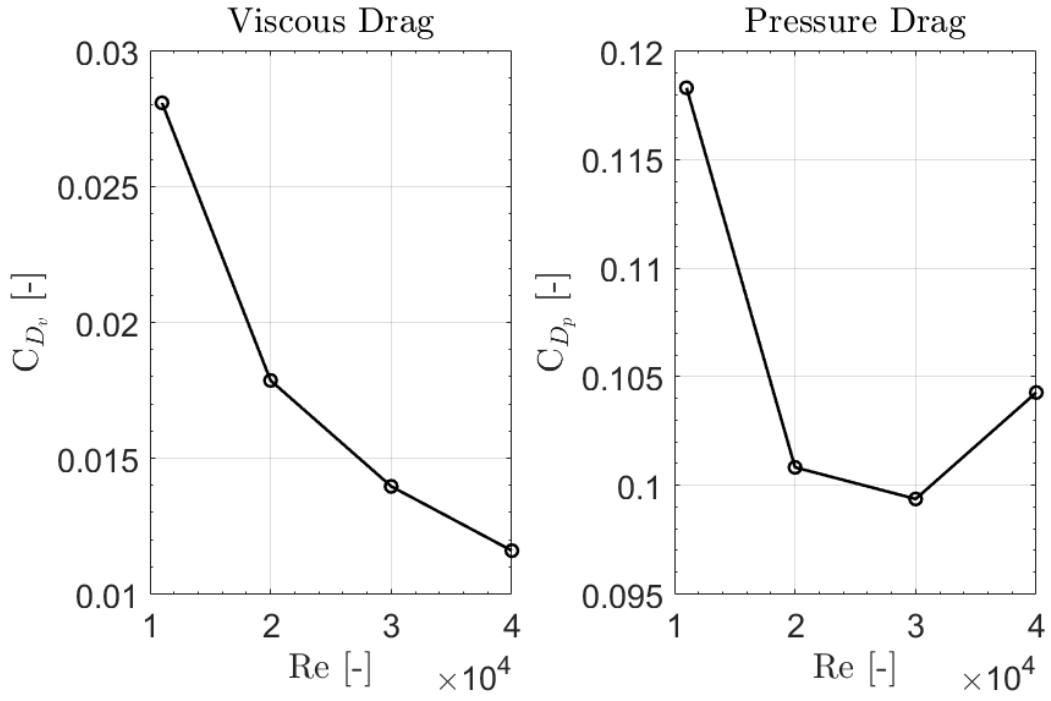

Figure 5.20: Reynolds number effect on the Viscous & Pressure Drag for a NACA 0012-34 Airfoil: M = 0.85, α = 8 deg

5.2.3. Boundary- & Shear-layer Stability

The separated laminar shear layer is expected to transition earlier as a result of an increasing Reynolds number, and this can be seen in Figure 5.21. The inflection point in the shape factor can be seen to move forward along the chord as Re increases. At Re = 20,000 the transition point appears to be around x/c = 0.90, and at Re = 30,000, this appears to remain the case. As Re increases to 40,000, the inflection point in the shape factor moves to around x/c = 0.65. This movement forward is consistent with the discussed Re effects in Chapter 2.1. Despite the forward movement of the transition point, the boundary layer prior to separation remains laminar, which can be seen in Figure 5.22, illustrating that the shape factor at separation remains around H = 4. In the discussion on the Mach number effects, it was stated that the transition point was important when it comes to the development of vortices in the separated shear layer; additionally, the shear layer separates sooner, which should amplify the Kelvin-Helmholtz instability. Despite this, no vortex shedding is captured from $Re = 2 \times 10^4$ and above. Compressibility has been discussed to have a stabilizing effect on the Kelvin-Helmholtz instability; as can be seen in Figure 5.18, for $Re = 2 \times 10^4$, the Mach numbers aft of the trailing edge outside the separated shear-layer are larger than its $Re = 1.1 \times 10^4$ counterpart, and thus would have an increased stabilizing effect. In any case, as discussed in the previous section, this would have to be researched further.

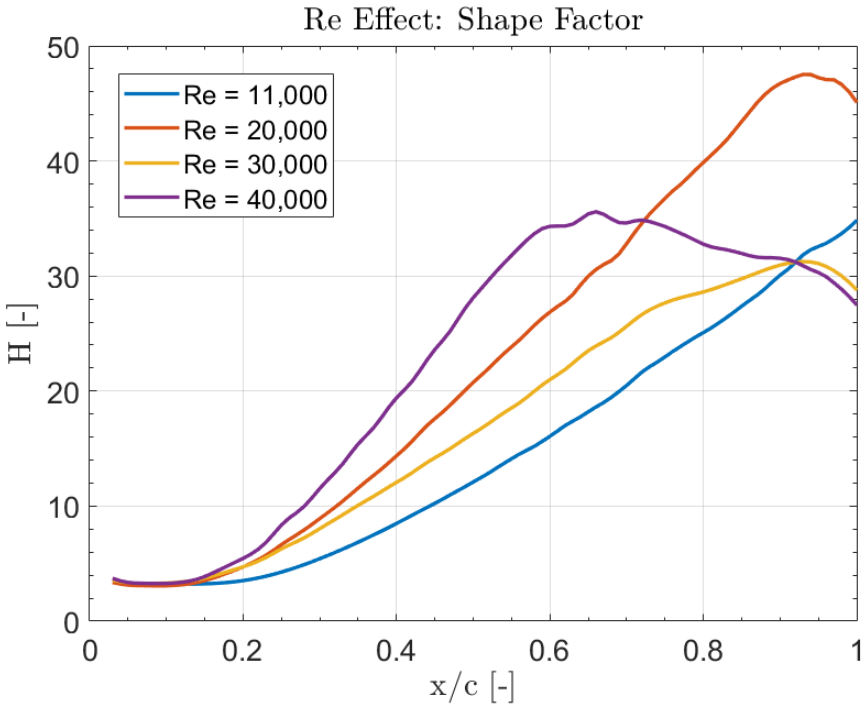

Figure 5.21: Reynolds number effect on the shape factor, H: M = 0.85, & α= 8 deg

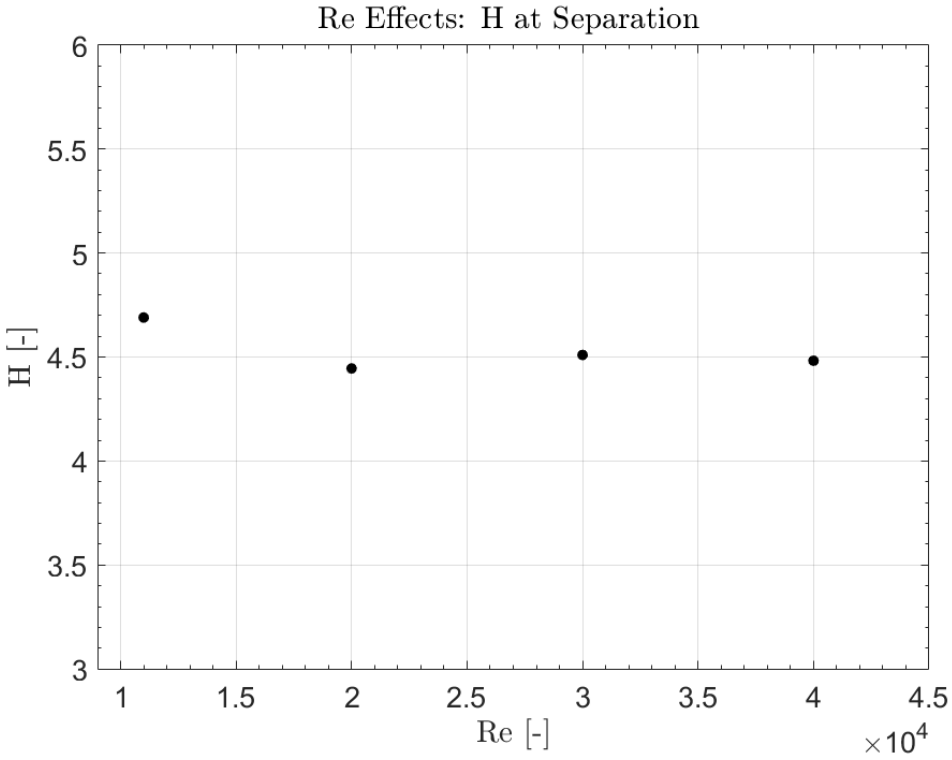

Figure 5.22: Reynolds number effect on the shape factor, H, at separation: M = 0.85, & α= 8 deg

5.3. Overview & Discussion

Taking a holistic approach; one can make some compelling arguments to what occurs in the low Reynolds transonic conditions typical for Mars. Primarily we have seen that a substantially smaller Reynolds number, relative to those typical on Earth, has a substantial impact on boundary- and shear-layer behavior, SBLI, and performance. The resulting smeared shock has diminished the impact of the shock substantially while allowing for increased attached flow due to the presence of the expansion fan allowing for a favorable pressure gradient. In general, relative to the low Reynolds high subsonic conditions one would expect on Mars, the transonic flight regime is either insignificant or mildly beneficial to performance. In general, the difference is minuscule, though is compelling in stating that the key factor in the reduction in performance for increasing Mach numbers at these conditions is not the shock, but due to a combination of increased boundary layer stability and a deviation from compressibility corrections.

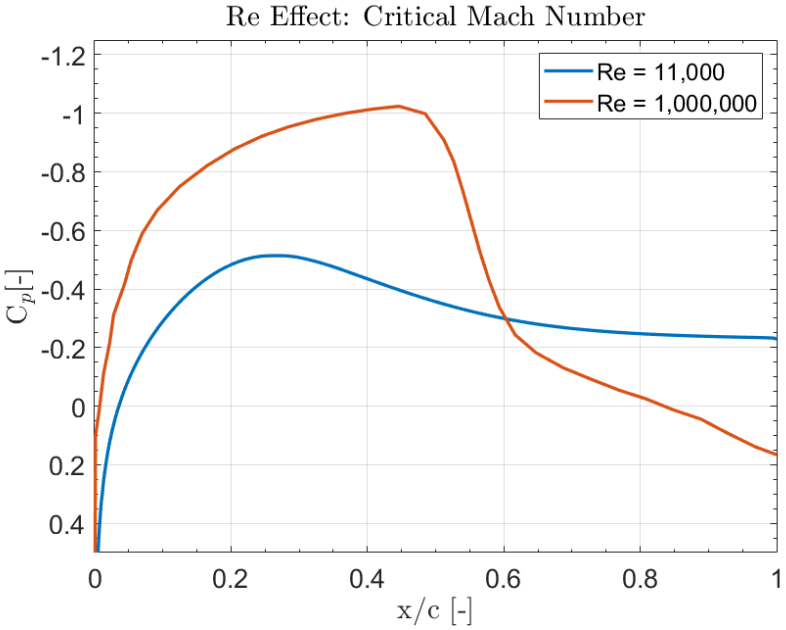

Figure 5.23: Comparison of Reynolds number impact on the suction side pressure distribution at M = 0.80 & α= 1 deg. (NACA 0012 pressure distribution taken from [33])

Viscous effects have been seen to garner prominence at compressible conditions on Mars; this is expected due to a decrease in Re, but as literature has stated, and as the results have shown, M has a substantial impact as well. This is due to the increased impact of viscous effects at low Reynolds numbers: the compressibility effects on viscosity dominate, as can be seen in the pressure distribution, primarily in the magnitude of the suction peak. This change has had a multitude of effects, but one that has not been detailed is the effect on the critical Mach number, M_{crit}. the magnitude of $C_{P,min}$ decreases with increasing M and thus a delay in M_{crit} is seen; this can be noticed by considering two pressure distributions at M = 0.80 and α = 1 deg (Figure 5.23). Both are considered at two different Reynolds numbers: Re =

1.1×10^4 and $Re = 1 \times 10^6$. The airfoils are a NACA 0012-34 and NACA 0012 respectively. The pressure distributions differ greatly and this is due to the viscous effects on $C_{P,min}$. The shock can be seen for $Re = 1 \times 10^6$, but is not present for $Re = 1 \times 10^4$. This indicates that the suppression of the suction peak, $C_{P,min}$, delays the formation of the shock.

The paper initially aimed to investigate whether a shock at low Reynolds numbers would be able to provide enough instabilities in the shear-layer in order to induce transition, and thus promote reattachment: increasing the amount of attached flow over the airfoil surface. This has been seen to not be the case, at least in the specific cases discussed. We have seen instead that the destabilizing effect of the shock is inconsequential, and in fact counteracted by the stabilizing effect of increased compressibility. However, the aft movement of the shock at increased Mach numbers has allowed for favorable pressure gradients to keep the flow attached longer, and combined with the diminished impact of a low Reynolds shock, and been seen to potentially be relatively productive to performance, though as mentioned, this gain is minute. What should be clear is that the main research question assumed the performance increase would be as a result of an increase in attached flow, whether this is through delayed separation, or encouraging the formation of a laminar separation bubble.

The smeared shock does not destabilize the boundary-layer enough in order to induce turbulence immediately thereafter, and thus the subsequent reattachment of the separated shear-layer fails to occur. In fact, due to the diminished interaction between the shock-wave and the boundary-layer, along with the aft movement of the shock wave (and resulting adverse pressure gradient); the boundary-layer stability increases. This is compounded due to the stabilizing effect of compressibility on the Kelvin-Helmholtz instability, which could explain the suppression of any vortex formation within the wake. The Reynolds number has been seen to be significant as well, given that a Reynolds number deviation of less than one order of magnitude has resulted in surprisingly substantial changes in performance above the critical Mach number. The smeared shock and resulting lambda structure is highly dependent on the Reynolds number, which in turn coupled with the Reynolds number's effect on boundary layer stability results in a complicated interchange and trade-off of the benefits and disadvantages of either.

The hypothesis set out in this report was partially correct in its assumptions about the flow physics at the conditions on Mars due in part to the diminished impact of shock-wave boundary-layer interactions at low Reynolds numbers; separation is delayed due to the expansion fan, but transition point is also delayed as well. Despite this, the conclusions with regards to lift-to-drag performance are inconclusive, or slightly affirmative. The lift-to-drag performance does slightly increase past the critical Mach number, but this is strictly relative to the high subsonic performance at the same Reynolds number. In any case, these conclusions apply to a relatively thick airfoil; a thinner airfoil suffers from less of an adverse pressure gradient, and thus laminar separation occurs layer. At higher angles of attack for a thin airfoil, the sharp curvature at the leading edge is detrimental due to the subsequent adverse pressure gradient, and thus these findings may be useful in such a case.

6 Conclusion & Recommendations

The conditions on Mars provide an environment where transonic Mach numbers can exist at Reynolds numbers between Re = 1×10^4 & Re = 1×10^5 with realistically achievable chord lengths. One of the aims of this paper was to expand upon the work conducted by Anyoji et al, who developed a Mars wind tunnel to analyze the flow behavior on Mars experimentally; despite this, their wind tunnel was not capable of reaching Mach numbers well within the transonic flow regime. In any case, the team discovered that the increased boundary layer stability due to reduced Reynolds number and increased compressibility be detrimental for performance, especially for thicker airfoils.

The hypothesis stated is correct in its prediction, but unsubstantial in impact. The diminished shock impact on the boundary-layer, combined with the expansion fan, produces a surplus of attached flow compared to the high subsonic case: the separation point is in fact delayed due to the aft movement of the shock, but the transition point is delayed further as well due to increased compressibility and a delay and weakening of the adverse pressure gradient, despite the presence of a shock. The aerodynamic performance provides a more optimistic view of the results. In terms of the question, while the aerodynamic performance does improve relative to the high subsonic cases, and is a result of a delay in separation, and drag savings due to the smeared shock. The gains in performance are unsubstantial, and performance still falls below that of a flat plate. In conclusion, the specifics of transonic flight on Mars provide an interesting look into low Reynolds numbers and could be applicable to other airfoil configurations.

6.1. Recommendations

The interaction with compressibility and the Kelvin-Helmholtz instability could be an interesting topic to expand into with regards to compressibility effects on Mars. The physical mechanism for why compressibility has a stabilizing effect on the Kelvin-Helmholtz instability is known, but how it impacts, and what occurs in the separated shear-layer for the discussed cases is not. In similar terms, the effect of increased compressibility at low Reynolds numbers has resulted in a dominance of viscous effects; this has been seen to have a substantial impact on the pressure distribution, and a detailed analysis of this could be interesting. In terms of methodology, conducting more resource-intensive numerical studies, or designing and developing a new or updated Mars wind tunnel for transonic flight conditions. The numerical method used to approach this subject, while accurate enough to provide a general outline and relative shifts in behavior, is lacking and fails to capture the smaller scales which would be interesting, specifically with regards to the Kelvin-Helmholtz instability.

Bibliography

[1] Rutvika Acharya. Investigation of differences in ansys solvers cfx and fluent. *Royal Institute of Technology, KTH*, 2016.

[2] Mars Helicopter/IngenuityNational Aeronautics and Space Administration. Mars helicopter/ingenuity. *Jet Propulsion Laborator*, 04 2020.

[3] Tousif Ahmed, Md. Tanjin Amin, S. Islam, and Shabbir Ahmed. Computational study of flow around a naca 0012 wing flapped at different flap angles with varying mach numbers. *Global Journal of Researches in Engineering*, 13, 01 2013.

[4] Ronald L. Allen and Duncan W. Mills. *Signal Analysis: Time, Frequency, Scale, and Structure*. John Wiley & Sons, Inc., 2004. ISBN 0-471-23441-9.

[5] Masayuki Anyoji, Daiju Numata, Hiroki Nagai, , and Keisuke Asai. Low reynolds number airfoil testing in a mars wind tunnel. *Department of Aerospace Engineering, Graduate School of Engineering Tohoku University*, 2010.

[6] Masayuki Anyoji, Daiju Numata, Hiroki Nagai, and Keisuke Asai. Effects of mach number and specific heat ratio on low-reynolds-number airfoil flows. *Journal of Aircraft*, 53, 2015. doi: 10.2514/1.J053468.

[7] Holger Babinsky and John K. Harvey. *Shock Wave-Boundary-Layer Interactions*. Cambridge, 2011.

[8] Marco Baragona. Unsteady characteristics of laminar separation bubbles. DUP Science, 2004.

[9] R.J. Bodonyi and F.T. Smith. Shock-wave laminar boundary-layer interaction in supercritical transonic flow. *Computers Fluids*, 14(2):97–108, 1986.

[10] R. D. Braun, H. S. Wright, M. A. Croom, J. S. Levine, and D. A. Spencer. Design of the ares mars airplane and mission architecture. *Journal of Spacecraft and Rockets*, 43(5): 1026–1034, 2006. URL www.scopus.com. Cited By :61.

[11] Claudia E. Brunner, Janik Kiefer, Martin O. L. Hansen, and Marcus Hultmark. Study of reynolds number effects on the aerodynamics of a moderately thick airfoil using a high-pressure wind tunnel. *Experiments in Fluids*, 62(178), 2021. doi: 10.1007/s00348-021-03267-8.

[12] Neil Cameron and D. Carter. Rotorblade trailing edge flap failure modes and effects analysis. *35th European Rotorcraft Forum 2009, ERF 2009*, 1:134–148, 01 2009.

[13] Brian Cantwell, May 2013. URL https://web.stanford.edu/~cantwell/AA200_Course_Material/TheNACAairfoilseries.pdf.

[14] Daniel Canuto and Kunihiko Taira. Two-dimensional compressible viscous flow around a circular cylinder. *Journal of Fluid Mechanics*, 785:349–371, 2015. doi: 10.1017/jfm.2015.635.

[15] BH Carmichael. Low reynolds number airfoil survey. *NASA CR 165803*, 1, 1981.

[16] M. Carnevale, S. Salvadori, M. Manna, and F. Martelli. A comparative study of rans, urans and nles approaches for flow prediction in pin fin array. *10th European Conference on Turbomachinery Fluid dynamics Thermodynamics*, 2013.

[17] Anubhav Datta, Beatrice Roget, Daniel Griffiths, Gregory Pugliese, Jayanarayanan Sitaraman, Jinsong Bao, Lin Liu, and Olivier Gamard. Design of a martian autonomous rotary-wing vehicle. *Journal of Aircraft*, 40(3):461–472, 2003. doi: 10.2514/2.3141. URL https://doi.org/10.2514/2.3141.

[18] J. Delery. *Physical Introduction*, chapter 2, pages 5–86. 2011.

[19] Jonas Dino and Brian Dunbar. Ames technology capabilities and facilities. https://www.nasa.gov/centers/ames/research/technology-onepagers/mars-airplane.html, 2008.

[20] Mark Drela and Michael B. Giles. Viscous-inviscid analysis of transonic and low reynolds number airfoils. *AIAA Journal*, 25(10):1347–1355, 1987. doi: 10.2514/3.9789. URL https://doi.org/10.2514/3.9789.

[21] R.J. Goldstein, V.L. Eriksen, R.M. Olson, and E.R.G. Eckert. Laminar separation, reattachment, and transition of the flow over a downstream-facing step. *Journal of Basic Engineering*, pages 732–739, 1970.

[22] Ed Grayzeck. Mars fact sheet. https://nssdc.gsfc.nasa.gov/planetary/factsheet/marsfact.html, 2020.

[23] Owen M. Griffin. A universal strouhal number for the 'locking-on' of vortex shedding to the vibrations of bluff cylinders. *Journal of Fluid Mechanics*, 85(3):591–606, 1978. doi: 10.1017/S0022112078000804.

[24] R. J. Hakkinen, I. Greber, L. Trilling, and S.S. Abarbanel. The interaction of an oblique shock wave with a laminar boundary layer. *NASA Memorandum 2-18-59W*, 1959.

[25] J. Hart. Comparison of turbulence modeling approaches to the simulation of a dimpled sphere. *11th conference of the International Sports Engineering Association, ISEA 2016*, 2016. doi: 10.1016/j.proeng.2016.06.191.

[26] H. P. Horton. A semi-empirical theory for the growth and bursting of laminar separation bubbles. *Aeronautical Research Council CP 1073*, 1969.

[27] B. M. Jones. Stalling. J. Roy. Aero. Soc. 38, 1934.

[28] John D. Anderson Jr. *Fundamentals of Aerodynamics*. Second Edition. McGraw-Hill, Inc., 1991. ISBN 0-07-001679-8.

[29] Mona Karimi. Compressibility effects on the kelvin-helmholtz instability and mixing layer flows. *Doctoral disertation*, 2015.

[30] J.T. Kegelman and T.J. Mueller. Experimental studies of spontaneous and forced transition on an axisymmetric body. *AIAA J.*, 24:397–403, 1986.

[31] Slawomir Kubacki, Daniele Simoni, Davide Lengani, and Erik Dick. An extended version of an algebraic intermittency model for prediction of separation-induced transition at elevated free-stream turbulence level. *International Journal of Turbomachinery, Propulsion and Power*, 5(4), 2020. ISSN 2504-186X. doi: 10.3390/ijtpp5040028. URL https://www.mdpi.com/2504-186X/5/4/28.

[32] Vladimir D. Liseikin. *Grid Generation Methods*. Second Edition. Springer, 2010. doi: 10.1007/978-90-481-2912-6.

[33] W.J. McCroskey, J.D. Baeder, and J.O. BridgerMan. Calculation of helicopter airfoil characteristics for high tip-speed applications. *AMERICAN HELICOPTER SOCIETY*, 41, 1985.

[34] J. H. McMasters and M. L. Henderson. Low speed single-element airfoil synthesis. *Technical Soaring*, 6(2):1–21, 1980.

[35] F. Menter. *Zonal Two Equation k-w Turbulence Models For Aerodynamic Flows*. doi: 10.2514/6.1993-2906. URL https://arc.aiaa.org/doi/abs/10.2514/6.1993-2906.

[36] R. F. Menter. Two-equation eddy-viscosity turbulence models for engineering applications. *AIAA*, 32(8):1598–1605, 1994. doi: 10.2514/3.12149.

[37] M.Kato and Brian Launder. The modelling of turbulent flow around stationary and vibrating square cylinders. 01 1993.

[38] Thomas J. Mueller and James D. DeLaurier. Aerodynamics of small vehicles. *Annual Review of Fluid Mechanics*, 35, 2003. doi: 10.1146/annurev.fluid.35.101101.161102.

[39] Phillip M. Munday, Kunihiko Taira, Tetsuya Suwa, Daiju Numata, and Keisuke Asai. Nonlinear lift on a triangular airfoil in low-reynolds-number compressible flow. *Journal of Aircraft*, 2015. doi: 10.2514/1.C032983.

[40] H. Nagai and A. Oyama. Development of japanese mars airplane. In *Proceedings of the International Astronautical Congress, IAC*, 2016. URL www.scopus.com. Cited By :10.

[41] T. Nagata, T. Nonomura, S. Takahashi, Y. Mizuno, and K. Fukuda. Investigation on subsonic to supersonic flow around a sphere at low reynolds number of between 50 and 300 by direct numerical simulation. *Physics of Fluids*, 28(5):056101, 2016. doi: 10.1063/1.4947244. URL https://doi.org/10.1063/1.4947244.

[42] T. Ohtake, Y. Nakae, and T. Motohashi. Nonlinearity of the aerodynamic characteristics of naca 0012 aerofoil at low reynolds numbers. *Japanese Society for Aeronautical and Space Science Papers*, 55(644):439–445, 2007. doi: 10.2322/jjsass.55.439.

[43] Laura L. Pauley, Parviz Moin, and William C. Reynolds. *THE INSTABILITY OF TWO-DIMENSIONAL LAMINAR SEPARATION*, pages 82–92. Lecture Notes in Engineering. Springer-Verlag, 1989.

[44] B. Petropoulos and C. Macris. Physical parameters of the martian atmosphere. *Earth Moon Planet*, 46:1–30, 1989. doi: 10.1007/BF00056296.

[45] Christopher J. Roy. Review of code and solution verification procedures for computational simulation. *Journal of Computation Physics*, 205(3):131–156, 2005. doi: 10.1016/j.jcp.2004.10.036.

[46] Christopher Rumsey. Menter shear stress transport model, Mar 2021. URL https://turbmodels.larc.nasa.gov/sst.html.

[47] M. Sajben and Y. Liao. *A criterion for the detachment of laminar and turbulent boundary layers*. 1995. doi: 10.2514/6.1995-2152. URL https://arc.aiaa.org/doi/abs/10.2514/6.1995-2152.

[48] A.D. Savel'ev. Supersonic flow past a wedge on a flat plate. laminar boundary layer separation and reattachment. *Fluid Dynamics*, 42(3):907–913, 2007. doi: 10.1134/S0015462807060051.

[49] Roy T. Schemensky. *Development of an Empirically Based Computer Program to Predict the Aerodynamic Characteristics of Aircraft. Volume I. Empirical Methods*, volume 2. GENERAL DYNAMICS FORT WORTH TX CONVAIRAEROSPACE DIV, 1973.

[50] Hermann Schlichting and Klaus Gersten. *Boundary-Layer Theory*. Springer, 2017. doi: 10.1007/978-3-662-52919-5.

[51] Robin Shrestha, Moble Benedict, Vikram Hrishikeshavan, and Inderjit Chopra. Hover performance of a small-scale helicopter rotor for flying on mars.

[52] Tosaporn Soontornpasatch. Computational study of low and high subsonic speed aerodynamic characteristics of the modified airfoil profile. *IOP Conference Series: Materials Science and Engineering*, 405:012002, 09 2018. doi: 10.1088/1757-899X/405/1/012002.

[53] Philippe Spalart and Christopher Rumsey. Effective inflow conditions for turbulence models in aerodynamic calculations. *Aiaa Journal - AIAA J*, 45:2544–2553, 10 2007. doi: 10.2514/1.29373.

[54] A Spentzos, George Barakos, KJ Badcock, BE Richards, Philippe Wernert, S. Schreck, and M. Raffel. Cfd investigation of 2d and 3d dynamic stall. 01 2004.

[55] O. Sugar-Gabor and A. Koreanschi. "design of supercritical low-reynolds-number airfoils for fixed-wing flight on mars". *Journal of Aerospace Engineering*, 33, 2020. doi: 10.1061/(ASCE)AS.1943-5525.0001166.

[56] T. Suwa, K. Nose, D. Numata, D. Nagai, and K. Asai. "compressibility effects on airfoil aerodynamics at low reynolds number. *30th AIAA Applied Aerodynamics Conference: AIAA Paper 2012-3029*, 2012.

[57] I. Tani. Boundary-layer transition. *Annual Review of Fluid Mechanics*, 1(1):169–196, 1969. doi: 10.1146/annurev.fl.01.010169.001125. URL https://doi.org/10.1146/annurev.fl.01.010169.001125.

[58] Engineering ToolBox. U.s. standard atmosphere. https://www.engineeringtoolbox.com/standard-atmosphere-d_604.html, 2003.

[59] Peggy L. Toot. Summary of experimental testing of a transonic low reynolds number airfoil. In Thomas J. Mueller, editor, *Low Reynolds Number Aerodynamics*, pages 369–380, Berlin, Heidelberg, 1989. Springer Berlin Heidelberg. ISBN 978-3-642-84010-4.

[60] L.L.M. Veldhuis. Aircraft aerodynamics primer, part 2. Delft University of Technology, 2019.

[61] A. Villegas and F.J. Diez. Effect of vortex shedding in unsteady aerodynamic forces for a low reynolds number stationary wing at low angle of attack. *Journal of Fluids and Structures*, 64:138–148, 2016. ISSN 0889-9746. doi: https://doi.org/10.1016/j.jfluidstructs.2016.03.012. URL https://www.sciencedirect.com/science/article/pii/S0889974616301980.

[62] Roelof Vos and Saeed Farokhi. *Introduction to Transonic Aerodynamics*. Fluid Mechanics and Its Applications. Springer, 2015. ISBN 978-94-017-9746-7.

[63] Shengyi Wang, Derek B. Ingham, Lin Ma, Mohamed Pourkashanian, and Zhi Tao. Numerical investigations on dynamic stall of low reynolds number flow around oscillating airfoils. *Computers Fluids*, 39(9):1529–1541, 2010. ISSN 0045-7930. doi: https://doi.org/10.1016/j.compfluid.2010.05.004. URL https://www.sciencedirect.com/science/article/pii/S0045793010001106.

[64] JONATHAN H. WATMUFF. Evolution of a wave packet into vortex loops in a laminar separation bubble. *Journal of Fluid Mechanics*, 397:119–169, 1999. doi: 10.1017/S0022112099006138.

[65] David Weyburne. The unbounded and bounded boundary layer models for flow along a wall. 01 2020.

[66] Justin Winslow, Hikaru Otsuka, Bharath Govindarajan, and Inderjit Chopra. Basic understanding of airfoil characteristics at low reynolds numbers. *JOURNAL OF AIRCRAFT*, 55, 2018. doi: 10.2514/1.C034415.

[67] Jian-Hua Xu, Wen-Ping Song, Zhong-Hua Han, and Zi-Hao Zhao. Effect of mach number on high-subsonic and low-reynolds-number flows around airfoils. *International Journal of Modern Physics B*, 34, 2020. doi: 10.1142/S0217979220401128. URL https://doi.org/10.1142/S0217979220401128.

[68] Han Yang and Ramesh K. Agarwal. Cfd simulations of a triangular airfoil for martian atmosphere in low-reynolds number compressible flow. *American Institute of Aeronautics and Astronautics, Inc.*, 2019.

[69] Serhiy Yarusevych, Pierre Sullivan, and John Kawall. On vortex shedding from an airfoil in low-reynolds-number flows. *Journal of Fluid Mechanics*, 632:245, 01 2010. doi: 10.1017/S0022112009007058.

A Ramp Simulations

The effect of the Reynolds number on shock-wave boundary-layer interactions has been discussed in Section 2.4.1; the Reynolds number has been seen to have a substantial effect on the interactions and primarily has an effect of lessening and spreading out the change in key flow parameters, such as pressure.

Whether or not the developed methodology can capture this behavior is unknown, as the shock wave boundary-layer interactions discussed are heavily dependent on what occurs within the boundary-layer, and thus the wall models utilized for a URANS approach may have an impact. Ramp simulations were conducted in order to ensure the validity of the model, and gain further insight into the SBLI in an isolated case study; The simulation considers supersonic flow over a non-slip flat plate with a wedge, or ramp, placed after said plate. The purpose of the flat plate is to develop the boundary-layer [48].

A.1. Methodology

The mesh and boundary conditions considered were similar to the validation mesh, with the only difference being supersonic pressure inlet & outlets, a slip wall in place of a far-field, and a flat plate + wedge in place of an airfoil. The lower boundary was replaced with a $0.05\,\mathrm{m}$ flat-plate, and a wedge with a $5\,\mathrm{deg}$ angle.

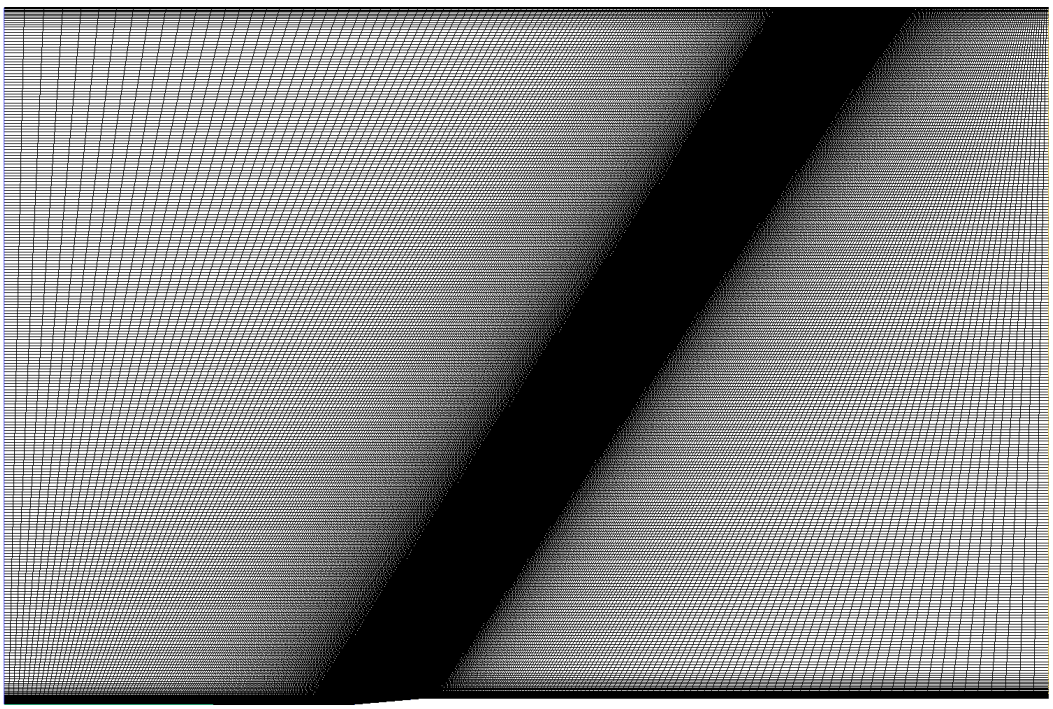

Figure A.1: Mesh of the Wedge Simulation [162,955 cells]

The initial conditions are similar to those discussed in the previous Chapter, however, the Mach and Reynolds numbers are different. Three Reynolds numbers were considered: 1×10^4, 1×10^5 & 1×10^6. The Mach number of 1.4 was selected based on the peak Mach number seen in the airfoil simulations, however, the exact value is not important. The deflection angle of the wedge was selected in order to produce a weak shock (Figure A.2), and thus, a $5\,\mathrm{deg}$ deflection angle was selected.

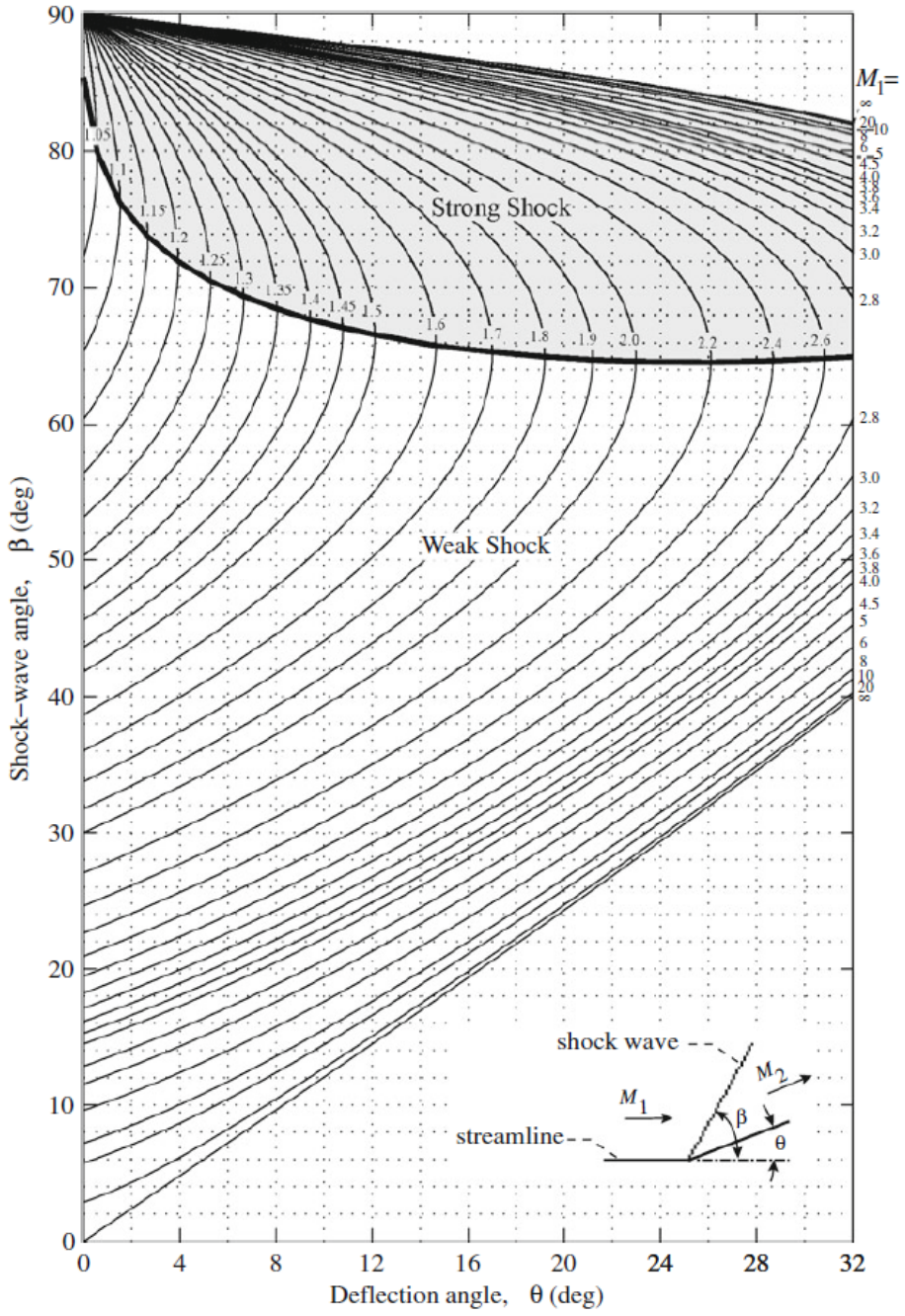

Figure A.2: Oblique shock charts [62]

A.2. Results

Figure A.3 illustrates the relative change in wall pressure across a weak shock at various Reynolds numbers; The pressure change is relative to the pressure prior to the shock formation, P_0, and is defined by Equation A.1. The pressure change used here is done in order to match that of the literature provided in Chapter 2.4.1, the pressure coefficient could also be utilized. The shock occurs at x_s = 0, where x_s is the non-dimensional distance to the beginning of the ramp, scaled by the length of the non-slip plate, c.

$$P_{rel} = \frac{\Delta P}{P_0} = \frac{P - P_0}{P_0} \tag{A.1}$$

The results follow the same trend as the theoretical method discussed in Section 2.4.1, indicating that a reduction in Reynolds number does lessen, and spread out, the impact of the shock on the boundary layer. This does indicate that the methodology utilized can capture the interaction between the shock wave boundary-layer discussed in Section 2.4.1.

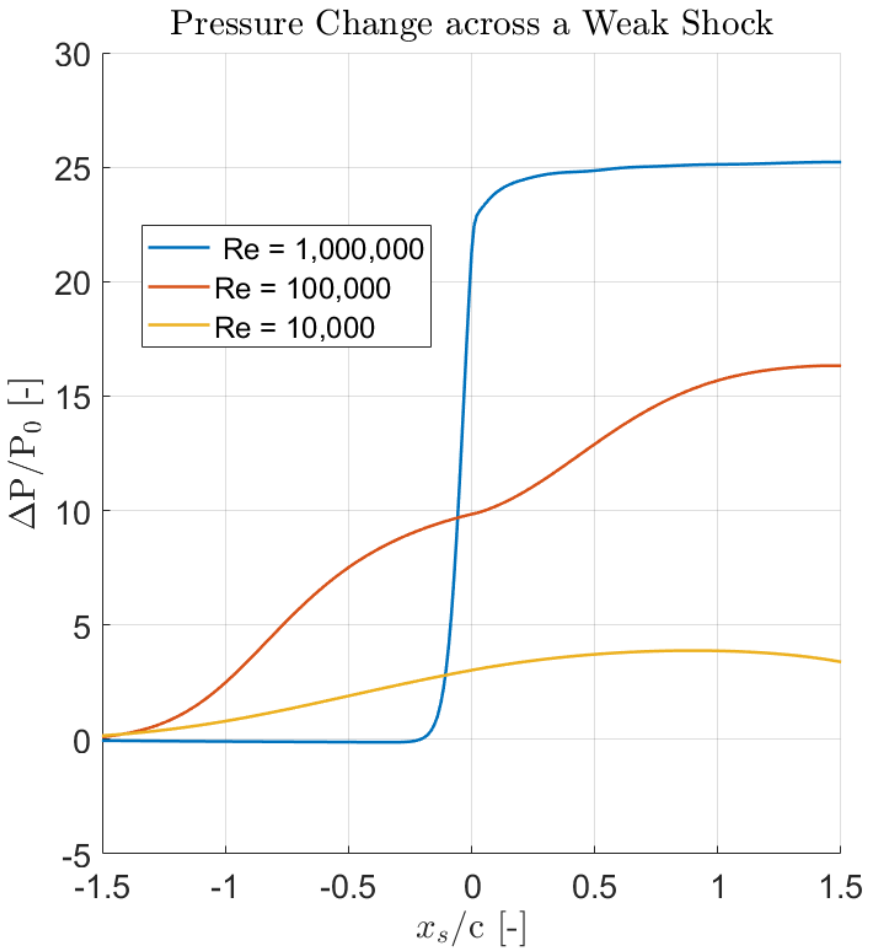

Figure A.3: Change in pressure across a shock (x_s/c = 0) at three Reynolds numbers: 1×10^6, 1×10^5, & 1×10^4

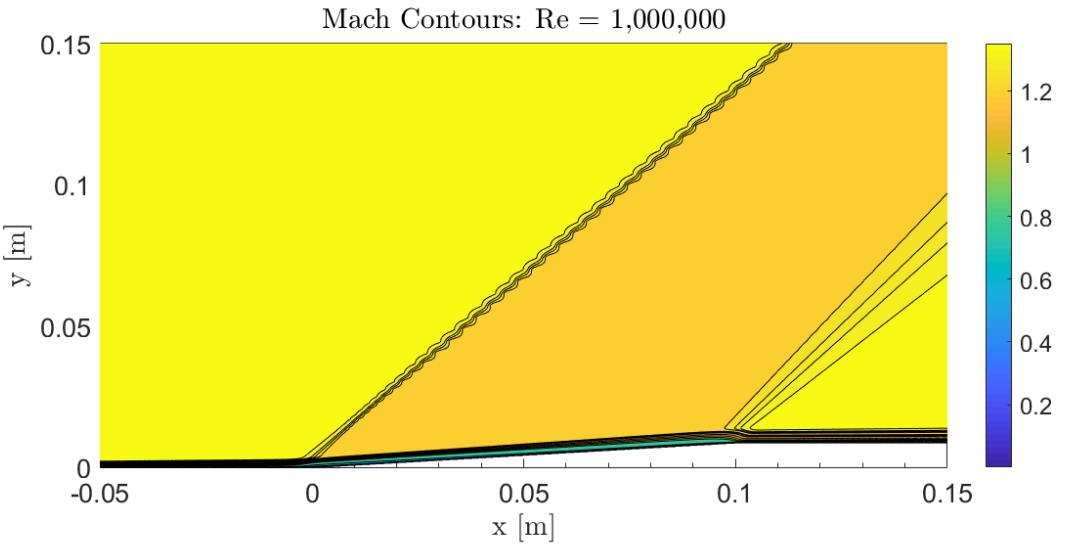

Figure A.4: Mach Contours Ramp M = 1.4, $Re = 1 \times 10^6$

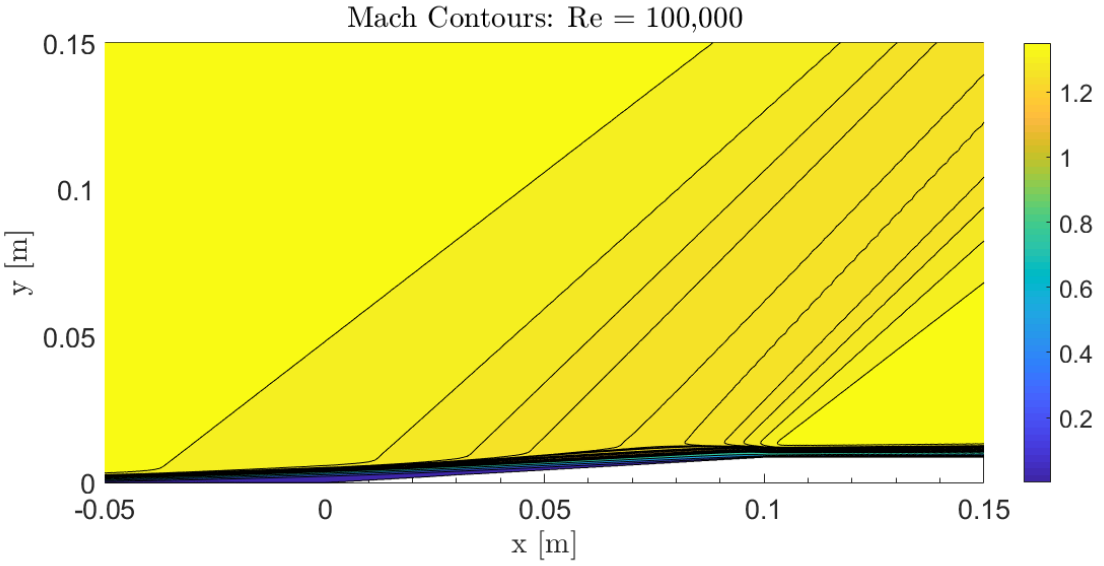

Figure A.5: Mach Contours Ramp M = 1.4, $Re = 1 \times 10^5$

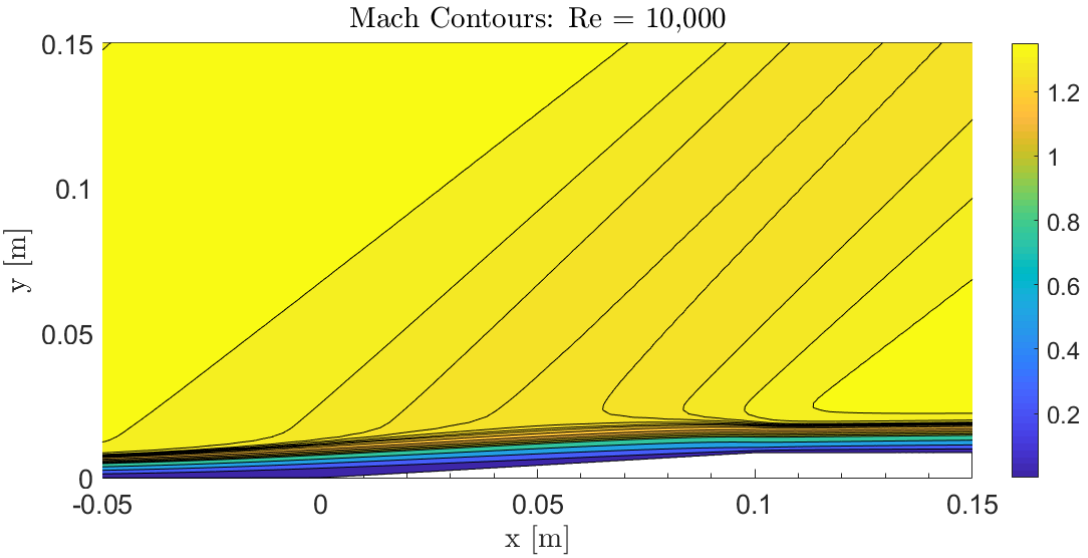

Figure A.6: Mach Contours Ramp M = 1.4, Re = 1×10^4

exac

B Pressure Distributions

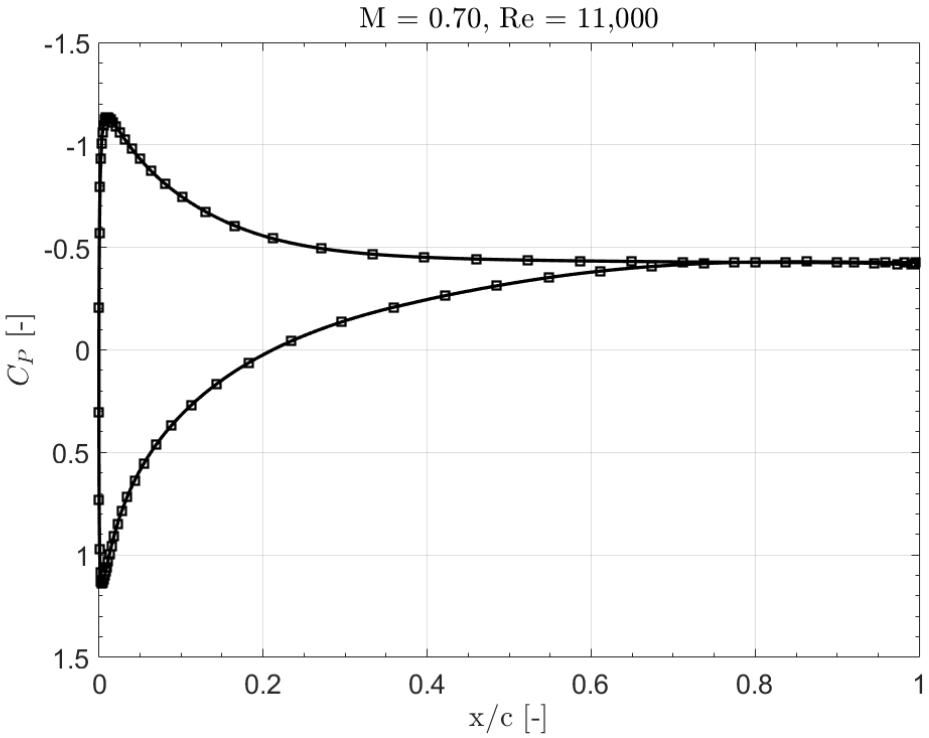

Figure B.1: Pressure Distribution: NACA 0012-34, M = 0.70, Re = 1.1×10^4 & α= 8 deg

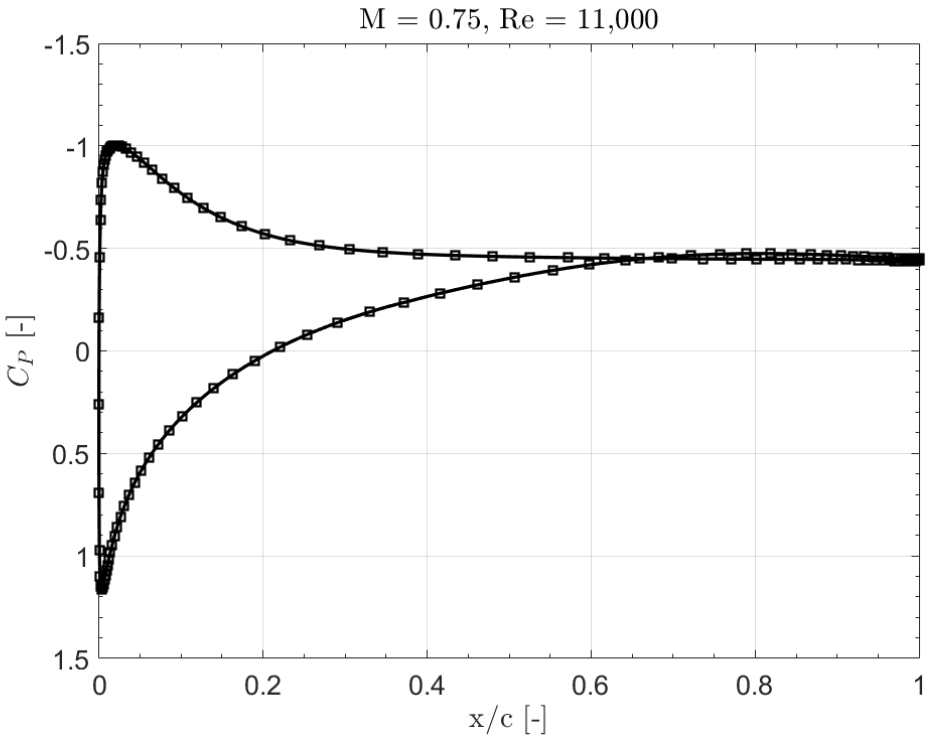

Figure B.2: Pressure Distribution: NACA 0012-34, M = 0.75, Re = 1.1×10^4 & α= 8 deg

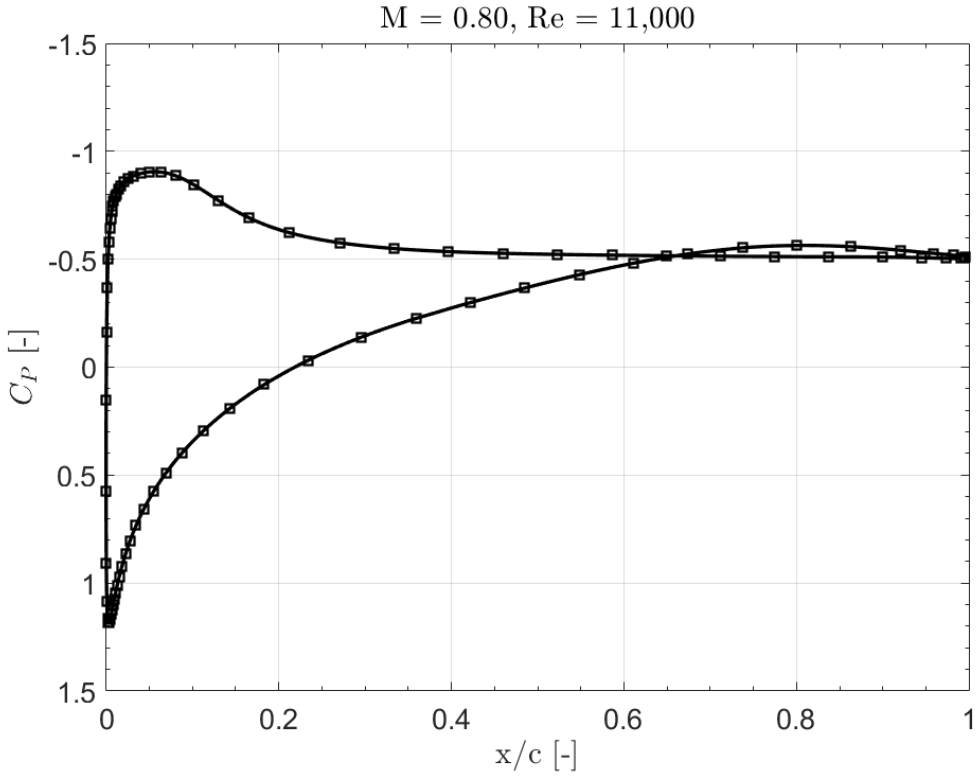

Figure B.3: Pressure Distribution: NACA 0012-34, M = 0.80, Re = 1.1×10^4 & α= 8 deg

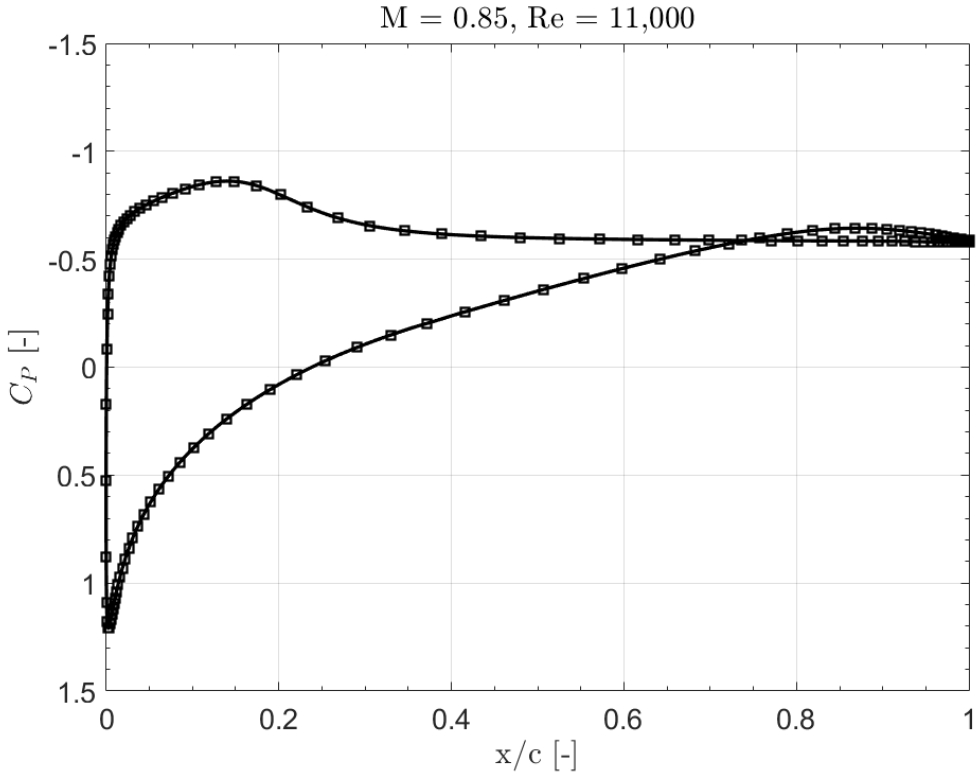

Figure B.4: Pressure Distribution: NACA 0012-34, M = 0.85, Re = 1.1×10^4 & α= 8 deg

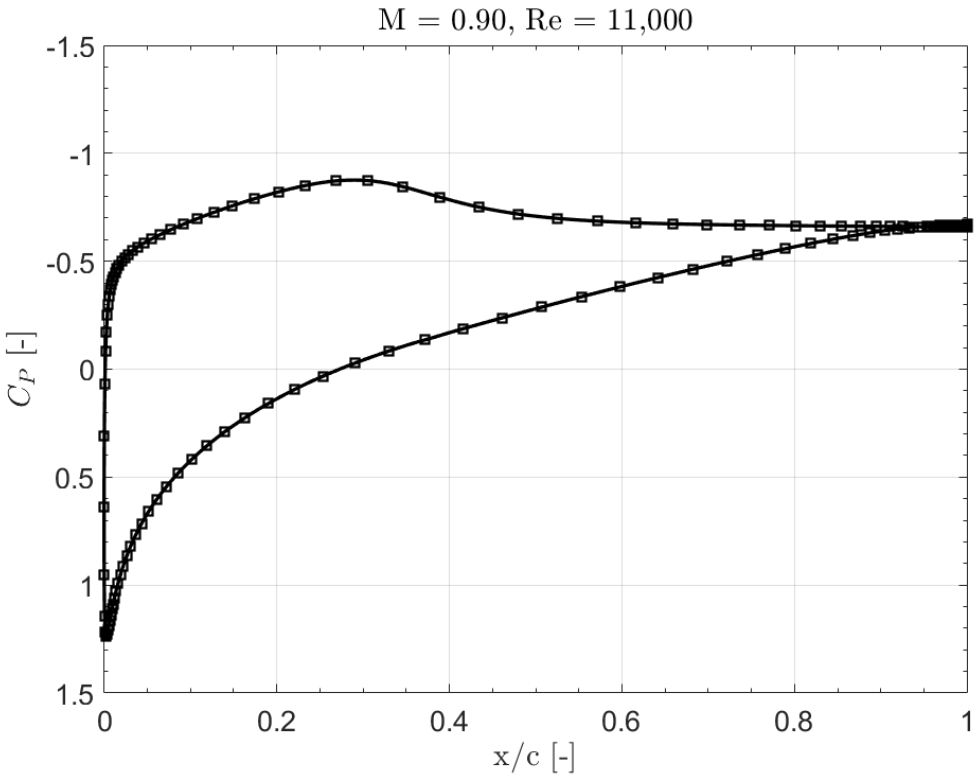

Figure B.5: Pressure Distribution: NACA 0012-34, M = 0.90, Re = 1.1×10^4 & α= 8 deg

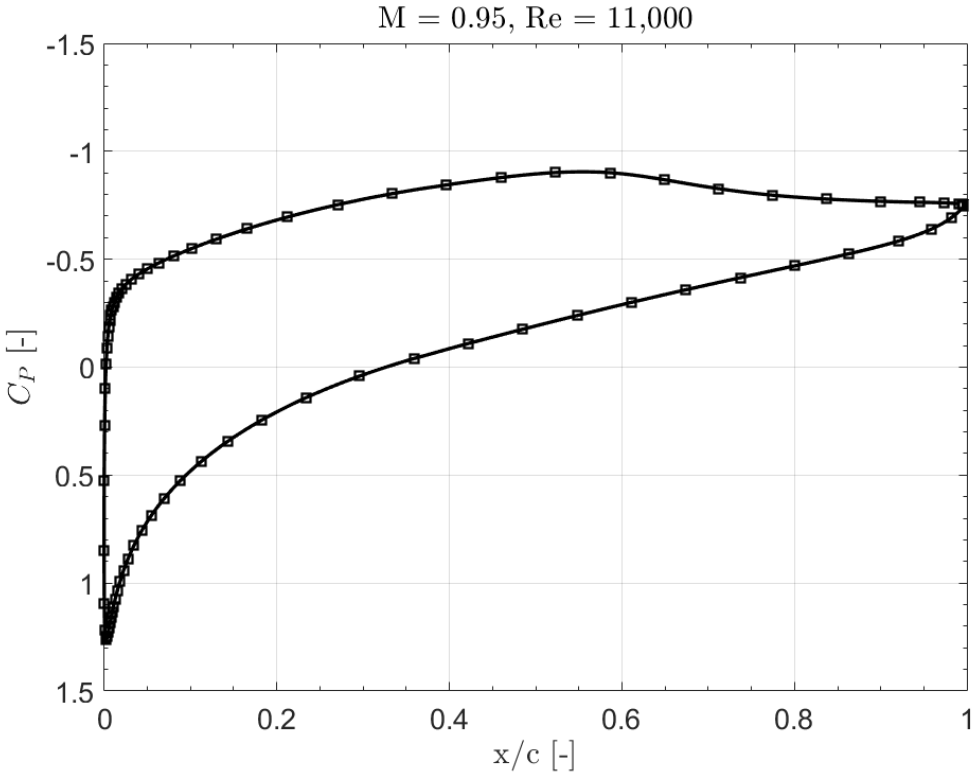

Figure B.6: Pressure Distribution: NACA 0012-34, M = 0.95, Re = 1.1×10^4 & α= 8 deg

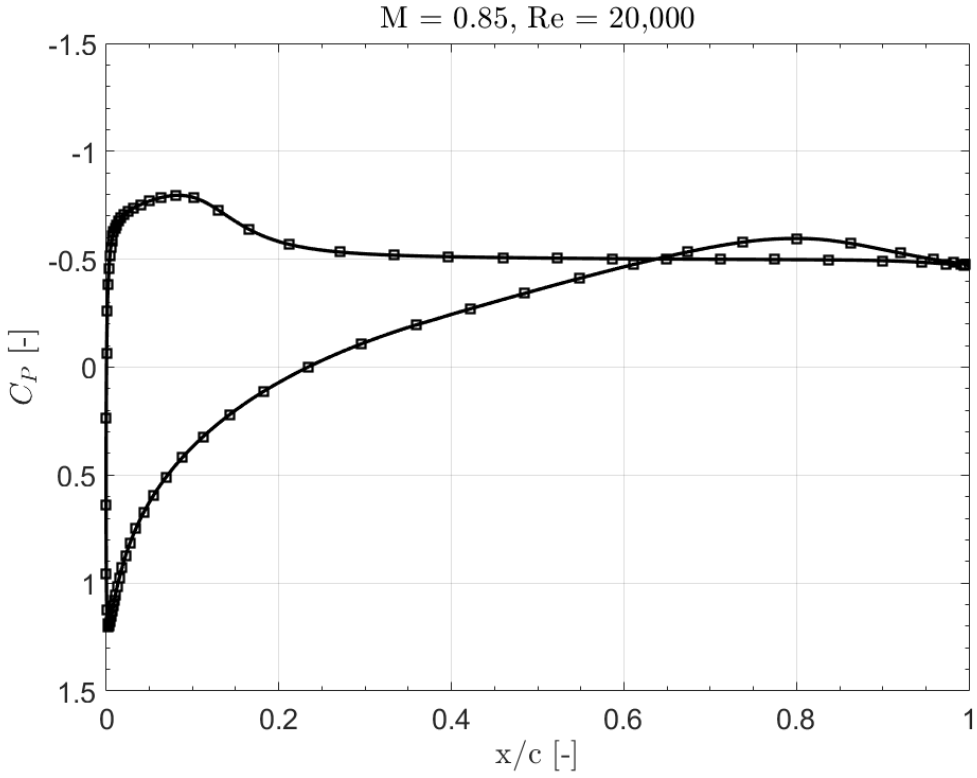

Figure B.7: Pressure Distribution: NACA 0012-34, M = 0.85, Re = 2×10^4 & α= 8 deg

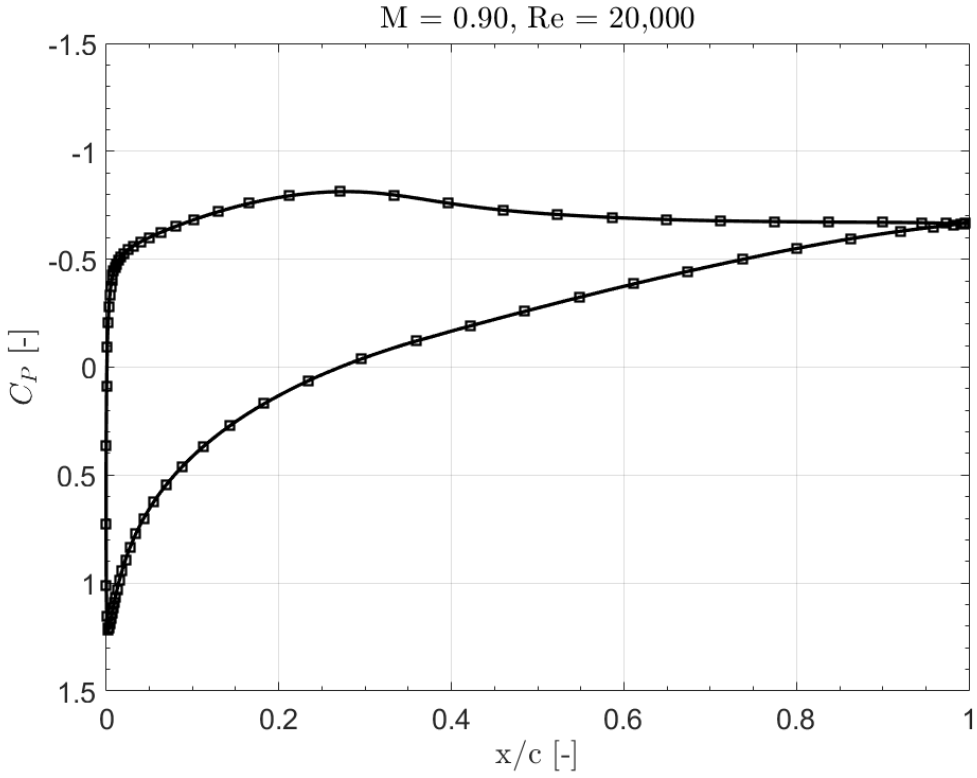

Figure B.8: Pressure Distribution: NACA 0012-34, M = 0.90, Re = 2×10^4 & α= 8 deg

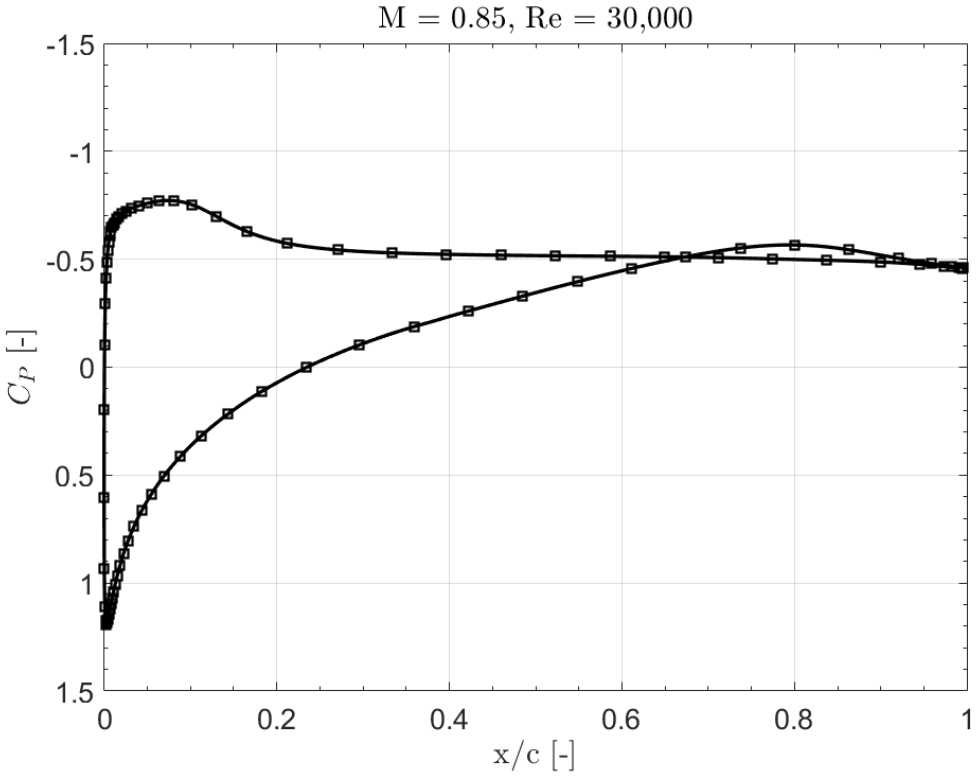

Figure B.9: Pressure Distribution: NACA 0012-34, M = 0.85, Re = 3×10^4 & α= 8 deg

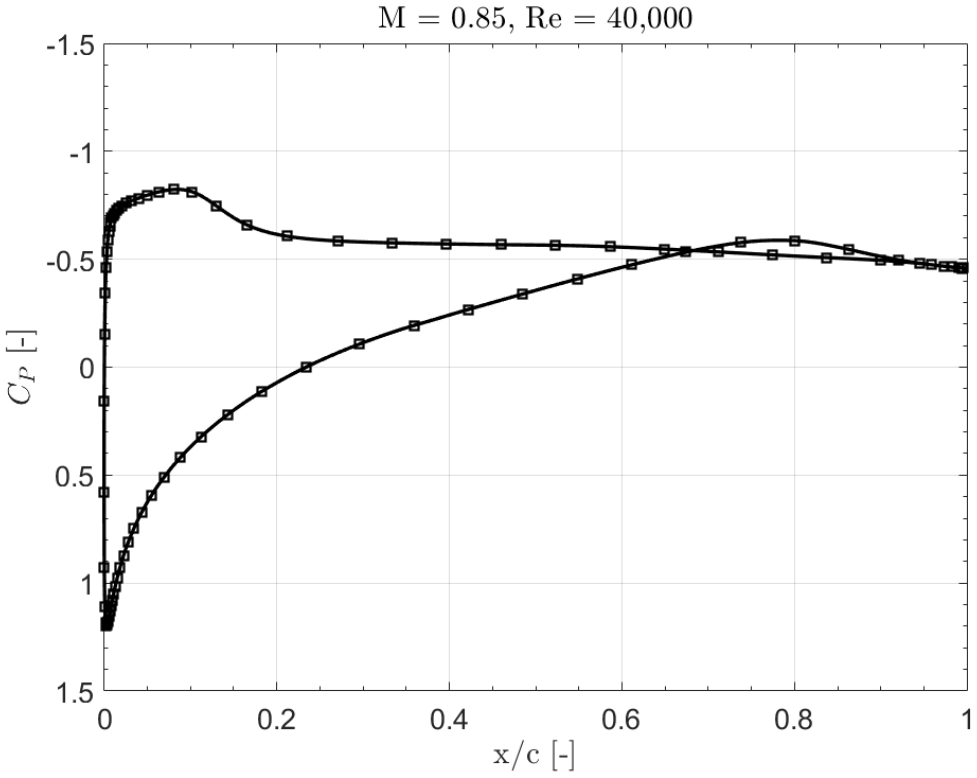

Figure B.10: Pressure Distribution: NACA 0012-34, M = 0.85, Re = 4×10^4 & α= 8 deg